

PROCEEDINGS

OF THE PAKISTAN ACADEMY OF SCIENCES:
A. Physical and Computational Sciences

ISSN Print: 2518-4245

ISSN Online: 2518-4253

Vol. 54(3), September 2017



PAKISTAN ACADEMY OF SCIENCES
ISLAMABAD, PAKISTAN

PAKISTAN ACADEMY OF SCIENCES

Founded 1953

President: Anwar Nasim
Secretary General: Zabta K. Shinwari
Treasurer: M.D. Shami

Proceedings of the Pakistan Academy of Sciences, published since 1964, is quarterly journal of the Academy. It publishes original research papers and reviews in basic and applied sciences. All papers are peer reviewed. Authors are not required to be Fellows or Members of the Academy, or citizens of Pakistan.

Editor-in-Chief:

Abdul Rashid, Pakistan Academy of Sciences, Islamabad, Pakistan; editor@paspk.org

Discipline Editors:

Chemical Sciences: Peter Langer, University of Rostock, Rostock, Germany; peter.langer@uni-rostock.de

Chemical Sciences: Syed M. Qaim, Universität zu Köln D-52425, JÜLICH, Germany; s.m.qaim@fz-juelich.de

Computer Sciences: Sharifullah Khan, NUST, Islamabad, Pakistan; sharifullah.khan@seecs.edu.pk

Engineering Sciences: Fazal A. Khalid, University of Engineering & Technology, Lahore, Pakistan; vc@uet.edu.pk

Mathematical Sciences: Muhammad Sharif, University of the Punjab, Lahore, Pakistan; msharif.math@pu.edu.pk

Mathematical Sciences: Jinde Cao, Southeast University, Nanjing, Jiangsu, China; jdcao@seu.edu.cn

Physical Sciences: M. Aslam Baig, National Center for Physics, Islamabad, Pakistan; baig77@gmail.com

Physical Sciences: Stanislav N. Kharin, 59 Tolebi, Almaty, Kazakhstan; staskharin@yahoo.com

Editorial Advisory Board:

David F. Anderson, The University of Tennessee, Knoxville, TN, USA; anderson@math.utk.edu

Ismat Beg, Lahore School of Economics, Pakistan; ibeg@lahoreschool.edu.pk

Rashid Farooq, National University of Sciences & Technology, Islamabad, Pakistan; farooq@sns.nust.edu.pk

R. M. Gul, University of Engineering & Technology, Peshawar, Pakistan; rmgul@uetpeshawar.edu.pk

M. Asghar Hashmi, The Islamia University of Bahawalpur, Pakistan; mhashmi@iub.edu.pk

Aynur Keskin Kaymakci, Selcuk University, Konya, Turkey; akeskin@selcuk.edu.tr

Tahir I. Khan, Professor of Materials Engineering, University of Bradford, Bradford, UK; T.Khan20@bradford.ac.uk

Zhou Lang, Nanchang University, Nanchang, Jiangxi, 330031, China; lzhou@ncu.edu.cn

Shaukat Mahmood, Mirpur University of Science & Technology, Mirpur, Pakistan; shau_meph@yahoo.com

Waqar Mahmood, University of Engineering & Technology, Lahore, Pakistan; waqar@uet.edu.pk

Onaiza Maqbool, Quaid-i-Azam University, Islamabad, Pakistan; onaiza@qau.edu.pk

Nadeem Mufti, University of Engineering & Technology, Lahore, Pakistan; namufti@uet.edu.pk

Adele Maria Muscolo, University Mediterranea di Reggio Calabria, Italy; amuscolo@unirc.it

Naveed K. Piracha, John Carroll University, University Heights, OH, USA; npiracha@jcu.edu

Martin C. Richardson, University of Central Florida, FL, USA; mcr@creol.ucf.edu

Mudasser Faraz Wyne, National University, San Diego, CA, USA; mwyne@nu.edu

Muhammad Younas, Oxford Brookes University, Oxford, OX33 1HX, UK; m.younas@brookes.ac.uk

Annual Subscription: Pakistan: Institutions, Rupees 2000/- ; Individuals, Rupees 1000/-

Other Countries: US\$ 100.00 (includes air-lifted overseas delivery)

© Pakistan Academy of Sciences. Reproduction of paper abstracts is permitted provided the source is acknowledged. Permission to reproduce any other material may be obtained in writing from the Editor-in-Chief.

The data and opinions published in the *Proceedings* are of the author(s) only. The Pakistan Academy of Sciences and the Editors accept no responsibility whatsoever in this regard.

HEC Recognized, Category X; PM&DC Recognized

Published by Pakistan Academy of Sciences, 3 Constitution Avenue, G-5/2, Islamabad, Pakistan

Tel: 92-5 1-920 7140 & 921 5478; Fax: 92-51-920 6770; Website: www.paspk.org

Printed at PanGraphics (Pvt) Ltd., No. 1, I & T Centre, G-7/I, Islamabad, Pakistan

Tel: 92-51-220 2272, 220 2449 Fax: 92-51-220 2450 E-mail: pangraph@gmail.com



PROCEEDINGS

OF THE PAKISTAN ACADEMY OF SCIENCES:

A. Physical and Computational Sciences

CONTENTS

Volume 54, No. 3, September 2017

Page

Review Article

- Solar Tracking Techniques and Implementation in Photovoltaic Power Plants: a Review 231
— *Fazli A. Khalil, Muhammad Asif, Shahzad Anwar, Sana ul Haq, and Farman Illahi*

Research Articles

- Design of Broadband Matching Network for Complex Reactive Load using L-Matching 243
— *Jawad Yousaf, Zubair Mehmood, Waseem Abbas, and Khuram Shehzad*
- On Classes of Analytic Functions Associated by a Parametric Linear Operator in a Complex Domain 257
— *Rabha W. Ibrahim, Adem Kilicman, and Zainab E. Abdulnaby*
- Automatic Signature Extraction from Document Images using Hyperspectral Unmixing 269
— *Kashif Iqbal, and Khurram Khurshid*
- Numerical Simulation of Fractional Order Dengue Disease with Incubation Period of Virus 277
— *Zain Ul Abadin Zafar, M. Mushtaq, Kashif Rehan, and M. Rafiq*
- Fractional Numerical Treatment for Biochemical Reaction Networks 297
— *Zain Ul Abadin Zafar, Kashif Rehan, M. Mushtaq, and M. Rafiq*
- Radiolysis-induced Dosimetric Characterization of Aqueous Solutions of a Synthetic Dye for Gamma Dosimetry 305
— *Muhammad Khawar Hayat, Ramiza, Taqmeem Hussain, Nasim Akhtar, Rabia Khaliq, and Abdul Hanan Saeed*
- Magnetotelluric Data Analysis using Swift Skew, Bahr Skew, Polar Diagram, and Phase Tensor: a Case Study in Yellowstone, US 311
— *Erick Pranata, Selvi Misnia Irawati and Sintia Windhi Niasari*
- Characterization of CO₂ Laser Photoacoustic Spectrometer Intracavity Configuration and Its Application in Measuring Acetone Gas in Human Breath 319
— *Mitrayana, Nurul Muyasaroh, Mohammad Ali Joko Wasono, and Mohammad Robikhul Ikhsan*
- Efficiency Enhancement of Banana Peel for Waste Water Treatment through Chemical Adsorption 329
— *Atif Khan, Hassan Jived Naqvi, Shabana Afzal, Shaista Jabeen, Misbah Iqbal, and Iram Riaz*
- Instructions for Authors 337

Submission of Manuscripts: Manuscripts may be submitted as E-mail attachment at editor@paspk.org. Authors must consult the **Instructions for Authors** at the end of this issue or at the Website: www.paspk.org



Solar Tracking Techniques and Implementation in Photovoltaic Power Plants: a Review

Fazli A. Khalil^{1*}, Muhammad Asif¹, Shahzad Anwar²,
Sana ul Haq¹, and Farman Illahi¹

¹Department of Electronics, University of Peshawar, Peshawar, Pakistan

²Institute of Mechatronics Engineering, University of Engineering and Technology,
Peshawar, Pakistan

Abstract: Electricity is one of the basic needs of life. Emission of harmful gases during the process of electricity generation leads to greenhouse affects. However, by employing photovoltaic (PV) panels, electricity can be generated without creating air, noise and water pollution caused by the emission of harmful gases. Geographically, Pakistan is located in a region of the world where solar irradiance is approximately 2000 KWh/m². In recent decades, grid-connected PV power plants have been implemented worldwide to fulfill the power requirements. Usually, these power plants are mounted fixed. However, with advancement in technology solar trackers have increased the yield. In this study, after reviewing and analyzing various PV tracking techniques, an open-loop single axis technique is suggested for use in the huge PV power plants.

Keywords: Renewable energy, PV system, single axis-tracking, dual-axis tracking

1. INTRODUCTION

Solar energy is an everlasting resource [1] for tomorrow because it is free, practically inexhaustible, and involves no polluting residues or greenhouse gases emission [2]. Photovoltaic (PV) solar cell directly converts sunlight to electricity. A solar system with 10% efficiency covering 0.16% of earth would provide 20TW (Terawatt) energy, about twice the world consumption rate of fossil energy [3, 4].

Recently, all over the world the energy demand has greatly increases. Meanwhile the resources of fossil fuels are depleting with the passage of time. The world's demand for energy will be almost triple in the forthcoming three decades [5]. This situation appeals the research community to pay attention toward renewable energy system. To find sufficient pollution free energy resources for future is one of the great challenges for society. Research in the field of renewable energy can solve this problem. Energy generated from natural renewable resources

such as wind, waves, tides, solar radiation etc. are termed as renewable energy.

In South Asia, especially Pakistan is facing an acute shortage of electricity since 2000. In 2014, the short fall reaches 4500-5500 MW [6]. To meet Pakistan's soaring demand in energy, there is a need to devise efficient energy system which is capable to fulfill energy needs at present and is sufficient in future too. The world's scientific advanced countries are using renewable energy systems to meet their needs [7]. These energy resources are environmental friendly and everlasting.

Many regions in Pakistan receive solar energy abundantly and sun light is present almost throughout the year. The yearly sum of global irradiance is approximately 2000 KWh/m² as shown in Fig. 1. Moreover, in most cities in Pakistan sun rise hours range 2200 – 2500 per year [5].

Photovoltaic energy is one of the mature technologies amongst all renewable sources. To

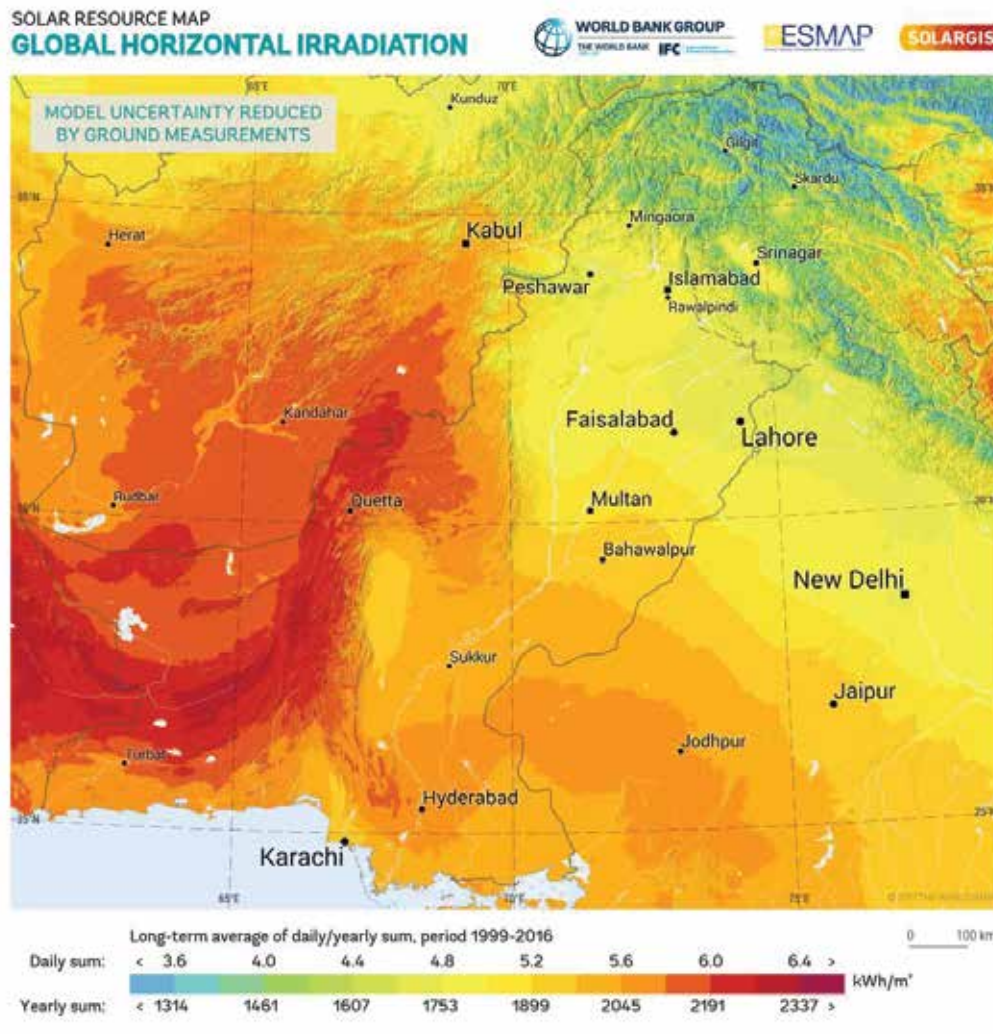


Fig. 1. Annual mean of global horizontal irradiance in $\text{kWh/m}^2/\text{day}$ [27].

harvest solar energy, solar tracker is used which keeps panel normal to the sun radiations in sunrise hours therefore, more energy could be collected.

One of the main objectives of this study is the investigation of solar tracking system and its various types, i.e., single and dual axis and their techniques along with open and closed loop system used in solar trackers. This study also discusses the implementation of tracking system in PV power plants and its effectiveness on the yield gain.

The reminder of this paper is organized as following: Solar tracker and its types are discussed in section II while Section III comprises of critical analysis of different techniques adapted by researchers to upgrade the efficiency of PV panels. To know the effective tracking method for PV power plant, conclusion is drawn in section IV.

2. SOLAR TRACKER

An automated system (in which solar panels are mounted), tracks sun's position accurately in order to maximize the power yield. Everyday sun rises in the east and move across the horizon toward west (solar azimuth angle) as illustrated in Fig. 2. A field of sunflowers rotate according to the sun motion (east to west) throughout a sunny day such that each leaf seek maximum light heliotropism, a clever bit of natural engineering [1, 2].

Sun changes its position throughout the days, years and seasons. To increase the energy production from PV panels, it is necessary to rotate the PV panels accordingly. It can be realized that more power will be generated if PV panel is exposed (for more time) towards the sun, so they can harness more sunlight. This idea describes solar tracking

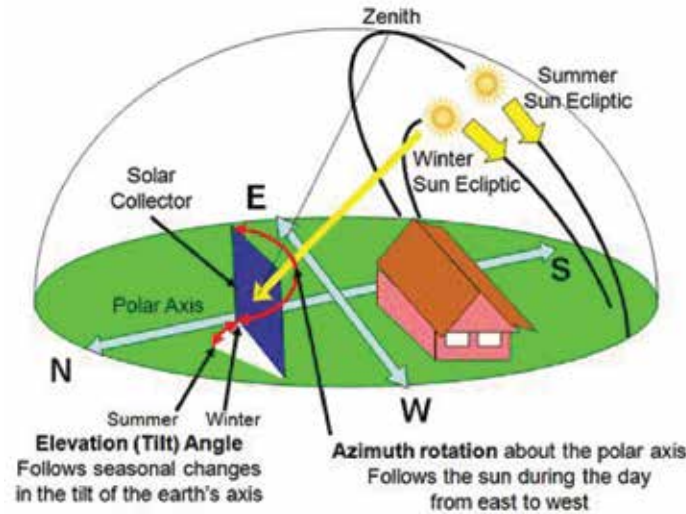


Fig. 2. Daily and seasonal movement of sun [9].

principle [8]. It increases the system's efficiency while reduces its size and overall cost. For solar trackers, it is challenging to always align the panel with sun. In crystalline or thin film PV power plants it is observed that if the tracker missed the target (sun) by few (up to 10) degree the yield still remain 98.5% of the full-tracking maximum, due to diffuse light [2, 9]. However, the concentrated solar power (CSP) system must be normal to solar radiations all the time. Tracker keeps the array of solar panels in focus with the sun for whole day, year and season – maximize the power yield [9]. In 1962, Finster [10] introduced first ever tracker which was completely mechanical, in the following

year, Saavedra [11] presented a tracker with an automatic electronic control mechanism, which was used to operate pyr heliometer. Mousazadeh et al. [3] further explore this idea in 2009 via examining their basic principles and subsequently analyzed various tracking techniques.

In light of the above discussion it is obvious that solar tracker is necessary for PV operation however avoiding tracking would affect performance [1]. The use of solar tracker not only increases energy harvesting but, also affects its cost, reliability, maintenance, performance and energy consumption [1, 12]. The energy gain from different tracking

Table 1. PV system gain tracking efficiency: a comparison.

Reference No.	Control unite	Drive method	Control mechanism	Orientation	% Gain
5	Microcontroller	Active	Close loop	Dual axis	40.0%
8	Microcontroller	Active	Open loop	--	26.0%
8	Microcontroller	Active	Close loop	--	33.0%
18	Microcontroller	Active	Open loop	Single axis	18-64%
20	Microcontroller	Active	Close loop	Single axis	20.0%
21	Microcontroller	Active	Open loop	Dual axis	64.0%
22	PLC	Active	Open loop	Dual axis	38.0%
23	Microcontroller	Active	Close loop	Dual axis	50-60%
24	Microcontroller	Active	Close loop	Dual axis	57.0%
25	Microcontroller	Active	Close loop	Dual axis	28.9%
12	Hybrid	Active	Close loop	Dual axis	25.0%
26	Volatile liquids	Passive	Open loop	--	23.0%
29	Volatile liquids	Passive	Open loop	Single axis	23.0%



Fig. 3. Zomework UTRF-168-2 passive solar tracking model [28].

techniques (reviewed in this paper) are categorized in Table 1. An ideal tracker keeps the PV module accurately towards the sun, compensates for both changes in elevation sun angle to track the sun throughout the day.

Solar trackers are categorized as active and passive on the bases of drive methods and discussed in the following sections.

2.1. Methods of Drive

2.1.1. Passive Trackers

In these trackers, a volatile fluid is compressed in containers, which is attached to both end of rack, and is shown in the Fig. 3. The solar radiation creates pressure inside the container which make the system imbalance—tends the system to move accordingly. This non-precise orientation makes it unsuitable for concentrating PV collector or tower solar concentrating system, however works better in mono or poly crystalline PV panel system [2]. The system does not use any gear and motor for rotation hence, power is not required. Zomework Corporation [2] a leader in passive solar energy products since 1969, while from 1980, more than 19,000 tracking system have been installed in different climates on nearly every continent on earth [2, 13]. Fig. 3 illustrates Zomework UTRF-

168-2 passive solar tracking model mounted on top of the pole.

2.1.2. Active Trackers

In these tracker gears and motor are used to drive the panel rack. The control circuit (microcontroller, Programmable Logic Controller (PLC), Personal Computer (PC), etc.) sends a command the motor to rotate – in order to track the sun. Since the motors consume energy so, they could be used only once required [2, 9].

2.1.3. Chronological Trackers

These tracker moves with the apparent speed of the earth but in opposite direction, i.e., 15°/h or one revolution per day, thus keep themselves align with sun. The speed of sun varies with season so, equation of time is used for high tracking accuracy – sundial time [2].

To provide feedback signal to the controlling circuit, solar trackers are classified into two categories i.e. open and closed loop trackers. Open loop trackers are simpler however, have low efficiency while closed loop trackers are more efficient with complexity. The complexity and efficiency have a tradeoff consideration. Close loop tracker's control mechanism is either based on

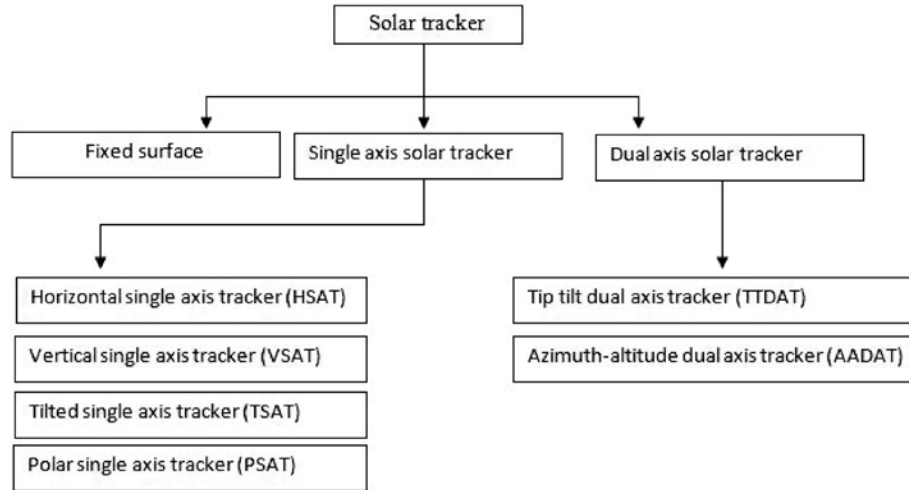


Fig. 4. Some common types of solar tracker; based on orientation capabilities.

microcontroller and optical sensor (Light dependent (LDR), Photodiode, etc.) or PC controlled based, auxiliary bifacial solar cell or a combination of both. Closed loop tracker is relatively complex however provides high accuracy [8].

Solar trackers are further classified into three categories by orientation capabilities: (i) the fixed mount; (ii) single axis; and (iii) dual axis trackers ;as illustrated in Fig. 4.

2.2. Types of Solar Tracker based on Orientation Capabilities

2.2.1. Fixed Mount Solar System

PV panels are mounted at fixed tilt angle (local latitude) facing south. Domestic, small scale commercial PV systems and solar geyser usually

use fixed surface solar system. The 100 MW Quaid-i-Azam Solar Park (QASP), Bahawalpur, (the first ever PV power plant) in Pakistan use fixed surface technique [14]. Fig. 5 exhibits a view of the Quaid-i-Azam Solar Park, Bahawalpur.

2.2.2. Single Axis Tracking System

This system traces the sun in single direction. Single axis tracking system offers one degree of freedom, which acts as an axis of rotation that is typically aligned along true north meridian. It is possible to align single axis tracker in any cardinal direction with advance algorithms [15, 19]. Such a system can be implemented in various configurations, such as horizontal single axis tracker (HSAT), vertical single axis tracker (VSAT), tilted single axis



Fig. 5. The 100 MW Quaid-e-Azam Solar Park, Bahawalpur, Pakistan [14].

tracker (TSAT) and polar aligned single axis tracker (PSAT) and is most effective at equatorial latitudes [1, 3]. As this system move in uni-direction; hence less operation is required and as a result less energy is consumed. Moreover, the simple nature makes it robust, thus less maintenance is need. On other hand, due to no proper alignment with sun rays, it harvest less energy hence its efficiency is low. The robust nature makes it suitable for PV power plant. In Greece [16], 8 MW PV power plant was installed using horizontal single axis tracker as shown in Fig. 6.

2.2.3. Dual Axis Solar Tracking System

Dual axis tracker tracks the sun in two directions; it has two degree of freedom that acts as axis of rotation. These axes are perpendicular to each other. Such a system incorporates the daily and seasonal changes which occurs in sun's path – exposes the

PV panels to the solar radiations to harvest optimum energy. This system can be implemented in two ways: (i) tip-tilt dual axis trackers (TTDAT); and (ii) azimuth-altitude dual axis trackers (AADAT) [1]. The above mentioned two types are the most popular of dual axis solar trackers and are used in various applications as illustrated in Fig. 7a and Fig. 7b.

3. TECHNIQUES USED TO ENHANCE EFFICIENCY OF PV PANEL

Single and dual axis tracking techniques were widely used throughout the world in PV power plants to maximize energy harvesting. These both techniques have some pros and cons. Dual axis tracking system offers high cost and high accuracy however low reliability (more down time more wear and tear). On contrary, single axis tracking system offers with low cost and less accuracy but high reliability (contains fewer things that can



Fig. 6. The 8 MW PV plant using horizontal single axis solar tracker in Greece [16].



Fig. 7(a). The TTDAT PV power plant [16].



Fig. 7(b). AADAT based PV plant in Toledo, Spain [16].

go wrong over the life time), hence requires less maintenance. In 1986, Akhmedyarov et al. [17] proposed an automatic sun tracking system in solar photoelectric station in Kazakhstan to increase the output power from 357 W to 500 W [15].

3.1 Single-axis Tracking Mechanism

Moniruzzaman et al. [18] performed a detail analysis of three level solar panel tracking system. The proposed system was compared with fixed PV system of the same number of panels. Three panels were mounted one above another with the height of half panel's width. The control circuit was microcontroller based open loop with fixed tilt angle equal to latitude along north – south. Unlike continuous rotation the proposed system was operated step-wise to reduce self-energy consumption. Gain in yield of 18-64% was recorded and compared to static PV system; however, occupied 33% less space. Therefore, the system is suitable for use in urban areas where less free room is available.

Anuraj et al. [20] have designed a solar tracker prototype with single degree of freedom; tracking the sun using Light Dependent Resistors (LDR). Their proposed system was microcontroller (ATMEGA 16) based automatic solar tracker. LDR detects sun light, which activate stepper motor to position PV panel, such that it receives maximum irradiance. The proposed tracker provides three mode of operation.

3.1.1 Normal Day Light Conditions

In daily sun's east-west motion, LDR1 needs to provide higher voltage than LDR2 to sense the rotation of sun. The tracker rotates 3.75° after every 15 minute.

3.1.2 Extreme Weather Conditions

In cloudy weather, a part of sunlight strikes both LDRs, as a result not enough voltage drops is measured across each LDR to judge the position of sun. To overcome this, a short delay of 1.5 minute is provided which checks the voltage of both LDRs. If voltage remains less than the defined threshold voltage, microcontroller check consecutively 10 times to make a wait state equal to 15 minutes to

get one-step, i.e., 3.75° .

3.1.3 Bi-directional Rotation

The tracker rotates from east to west throughout the day to follow the sun. At dusk the tracker faces west. Tracker is required to come back to initial position for next day. A variable I counts tracker steps it takes throughout the whole day; approximately 40, equals to 150° rotation. Once the variable I counts greater than 40 steps, tracker moves back to its initial position for the next day and power supply turned off until LDRs receive sunlight at Dawn. A brush along roller was added to clean the dust accumulated on the surface of panel, twice a day. Analysis and calculation shows that the proposed system can harvest 20% more energy, compared to fixed mount system. Huynh et al. [8] compared and analyzed open and closed loop trackers theoretically and experimentally. Data comprises of current and voltage output of each tracker was recorded on May 15th, 2013 from 7:00 am to 5:00 pm. Mathematical calculation in [8] shows that power gain for open and closed loop trackers were 25.96% and 33.00% compared to static panel of same size.

3.2 Dual-axis Tracking Mechanism

Furkan et al. [21] designed and analyzed an open loop, dual axis solar tracker. The performance of fixed tilted (37°) and dual axis movable solar tracker was analyzed theoretically and experimentally for climatic condition of Denizli, Turkey. DC motors were used to control the movement of solar tracker. Microcontroller along with external real time clock (RTC), two position sensors (potentiometers) and motor driver circuit were used to calculate the position of sun. In addition to experimental data, visual C#2005 computer programming was used for equations of solar radiations values of fixed and moving PV systems. The performance of two-axis tracker over fixed one was compared for the month of May and June, and was found the energy increase up-to 64% for tracking system.

Mahmood et al. [22] designed and implemented an open loop dual axis solar tracker using programmable logic controller (PLC). For PV panel rotations, direct current (DC) motors were used. The built-in yearly, weekly and hourly

timers of PLC were used to accurately track the sun throughout the year. The angles that were used in tracking have been calculated during rise hours of the day, for all days of years. MATLAB was used for computation and plotting. The equations of zenith angle and sun rise hours were converted to executable *m.file*. The programming performs calculation on the basis of these equations in [22] and extracts angles for vertical and horizontal angles for each and every day of the years. A simple solar positioning algorithm was presented in their study. Power outputs of the proposed system and fixed one were compared. A power gain of 38% was obtained with their proposed system.

Farhana et al. [23] discussed the structure and application of azimuth-altitude dual axis solar tracker. Mathematically, in [23] it was proved that solar energy increases 50-60% when dual axis solar tracker was used. The controlling circuit consists of microcontroller (PIC 18F452), two stepper motors (one for azimuth angle and the other one for latitude), six LDRs (three for azimuth tracking and the remaining three for elevation tracking). Energy output of fixed PV system and dual axis solar tracker was calculated which is 7.6KWh/m²/day and 12 KWh/m²/day respectively. It was shown that dual axis solar tracker maximize the energy output twice. Daily electricity expenditure was calculated for an ideal house of four family members i.e. 15.58KWh/day and the proposed solar tracker generates 12 KWh/day. From the national grid about 3.58 KWh/day energy was required.

Titirsha et al. [24] performed valuable advancement in dual axis tracking system. Mirrors were used on both sides of PV panels; to re-capture the reflected light from PV panel. The more photon strikes on PV panel the greater energy will be produced. Mathematical calculations in [24] were carried out and energy production for all day was calculated. It was realized that using the proposed system an increase of 57% would be achieved in output energy.

Bajpai et al. [25] designed automatic, two-axis solar tracker. The control circuit consists of microcontroller (ATMEGA 32L). Three LDRs (for sensing sunlight) mounted on rectangular plate at 120° separation to each other at top in center of PV

module and two DC motors. Their experimentation consists of Wheatstone bridge circuit mechanism. Code Vision AVR (software) was employed to generate the code for microcontroller and PROTEUS (software) was employed for logic simulation. In experimental studies 37W PV panel was used for static as well as for tracking system. Comparative performance analysis was carried out for static (37° tilt angle) and for proposed two axis tracking system. The data was recorded on hourly basis from 6AM to 5PM. The ambient temperature at the time of experiment was 27°C. The performance of both systems was comparatively analyzed for the following parameters:

- a) Solar irradiation received on collector.
- b) Maximum hourly electrical power (P_{max}) and efficiency gain (η gain).
- c) Short circuit current (I_{sc}) and Open circuit voltage (V_{oc}).
- d) Fill Factor (FF).

The irradiation gain for proposed tracking system was insignificant from 11 AM to 1 PM due to small azimuth angle. For the rest of sunshine hours the gain was significant due to non-alignment of sun rays with plane perpendicular to fixed PV module. Maximum irradiation gain of 22.19 W/m² was recorded at 8 AM while minimum gain of 2.33 W/m² has been recorded at 1 PM (output degrades with high ambient temperature).

The electrical output for both systems along with gain in yield was recorded hourly and compared. Furthermore, due to low cell temperature, high power gain was recorded at morning and evening session. Each degree rise in ambient temperature decrease the output by 0.5% of crystalline silicon solar cell. The maximum (efficiency gain) η_{gain} of 59.6% and 76.96% at 7 AM and 4 PM, respectively, had been recorded. While the minimum η_{gain} of 1.02% and 0.04% at 11 AM and 12 PM respectively was recorded because of high temperature.

Hourly variation of V_{oc} (open circuit voltage) and I_{sc} (short circuit current) was recorded. Comparison shows that from 11 AM to 1 PM, V_{oc} obtained with their proposed tracking system remain the same however, I_{sc} remains higher for tracking system compared to fixed system. V_{oc} also

depends upon insolation (amount of solar energy per square centimeter per minute) received so at evening and morning V_{oc} was minimum with static system due to less solar radiation.

Fill-Factor (FF) was correlated with series and shunt resistances. From 6 AM to 3 PM the solar cell temperature was high for tracking system; increases series while decrease the shunt resistance – cause losses. Fill Factor was low for the proposed system indicates its effectiveness at low temperature.

The average η_{gain} and max power obtained by this proposed dual axis solar tracker was 28.87% and 5.0423 W/hr, respectively, compared to the static PV system.

Pakistan receives abundant sunlight almost though out the year. Waleed et al. [5] discussed the geographical location of Pakistan. In Pakistan annual irradiance is approximately 2200-2500 hours per year. They designed closed loop, dual axis solar tracker which follows the sun. The control circuit consist of microcontroller (PIC 16877), LDR GM9516 and two stepper motors of rating 6 V & 0.6 A. Four LDRs were used for sun tracking, each pair for horizontal and vertical. On four sides of PV panel LDR was mounted. The light intensity on each LDR should be the same. On horizontal plane if left LDR receive less light than right LDR, the controller will move the PV panel in such direction that the both LDRs receives same light intensity. The same procedure was applies for vertical movement. Monocrystalline PV panel of 16x16 dimensions was used for experiment. The data was recorded on hourly basis from 8:00 AM to 6:00 PM. First, $V-I$ parameters were recorded for fixed, single axis and dual axis trackers and subsequently power output for each system was calculated. Power output for all the three systems were compared, it was observed that using dual axis solar tracker one can achieve power gain up-to 40% compared to static PV system.

Ferdaus et al. [12] performed designing, implementation and testing of a hybrid dual axis solar tracking system. The tracker operates on two motors to rotate the solar panel. One for east-west motion whiles the other for north-south motion. The proposed system was operated and tested in three modes, i.e., static, continuous and hybrid. It

was realized that the hybrid mode harvest 25.62% more energy than static mode while 4.2% less than continuous mode but further comparison of results showed that the hybrid movement consume 44.44% less energy compared to continuous mode.

3.3 Passive Tracking Mechanism

Narendrasinh et al. [2] designed open loop single axis passive solar tracking system works on Zomework principles. High volatile liquid filled in two metal (stainless) canisters with high pressure, fixed on both sides of the rack. Both canisters were connected to each other by a metal pipe. The complete system mounted on a fixed pole, that PV panels could easily be rotated. Aluminum plates were fixed on both cylinders in such orientation that outer half portion was shaded. The model start the day, facing west but when sun raises in the east, the radiations strikes the west side of cylinder filled with volatile liquid of low boiling point. The liquid gets heat in narrow tubes and moves toward east which cause the imbalance, rotates the tracker eastward. In their experimentation, aluminum plates were used to control the heating process of cylinder. If one cylinder exposes more to sun radiations than other, its vapor pressure increases and enforces the liquid to move toward the cooler side. This imbalance rotates the rack until the cylinders are equally shaded. The tracker completes its daily cycle facing westward and sleeps in this position throughout the night until the sun rises in the next morning. The performance of this tracker was test using three different liquids having following properties mentioned in Table 2.

The power output was calculated for both static mounted PV modules and the desired tracker PV modules. Using the desired tracker an increase of 23.33% in power output was recorded. Further, a solar system of 12-modules with the desired tracker delivers the same power as 15-modules mounted on static rack. Hence, time of three modules was saved.

Clifford et al. [26] designed a novel passive solar tracker that have low cost and is suitable for operation in equatorial regions. The tracker works on passive mechanism; high pressure and low boiling liquid was filled in the cylinders attached

Table 2. Liquid's properties test.

S. No	Properties	Volatile liquids		
		Thinner	Methanol	Acetone
1	Chemical formulae	CH ₂ Cl ₂	CH ₃ OH	(CH ₃) ₂ OH
2	Boiling point (°C)	4.00	64.6	56.2
3	Vapor pressure (mm Hg)	300.0	96.0	181.7
4	Density (g cm ⁻³)	1.325	0.271	0.784
5	Molar weight (g mol ⁻¹)	84.94	32.04	58.1
6	Specific gravity (at 25°C)	1.315	0.791	0.788

on two sides oppositely. The striking beam of sun rays produced imbalance of pressure, which moves the tracker. Computer modeling were performed which predicts an increase in efficiency up to 23% compared to static PV panels.

It is obvious from the above discussion that tracking system has good impact on the efficiency of the PV system. Furthermore, the literature review suggest that tracker is favorable in large power system however, not suitable for small scale power system because extra power is needed for its operation as well as technical persons are also need to ensure proper maintenance on time.

3. CONCLUSIONS

Solar tracker is employed to harvest maximum energy from the solar system. In tracking, it is essential to align the panels normal to solar irradiance. In this study, various developed tracking techniques were reviewed and analyzed. Obviously, the open loop trackers are simpler, less expensive to maintain compared with closed loop trackers and are reliable. The open loop trackers have no feedback mechanism; therefore, often their efficiency is lower than the closed loop trackers. The closed loop trackers can perform more efficiently by introducing the feedback phenomenon to track sun irradiance. Alternatively, closed loop trackers are expensive and complex to manage, compared to open loop trackers. Concentrated PV panels (multi junction solar cell) and concentrated solar power (tower solar system) need high accuracy while flat solar panels yield about 98%, if the target (sun) is off by 10 degrees. It was further observed that single axis tracker system might be one of the best options for operating flat panel solar power plants; however, for concentrated solar power plants dual

axis tracking system would produce an enhance amount of power.

5. REFERENCES

1. Karimov, K.S., A. Saqib, P. Akhter, M. Ahmed, J. Chattha, & S.A. Yousafzai. A simple photo-voltaic tracking system. *Solar Energy Materials and Solar Cells* 87: 49–59 (2005).
2. Parmar, N.J., A. Parmar, & V. Gautam. Analysis and implementation of passive solar tracking system. *International Journal of Emerging Technology and Advanced Engineering* 5(1): 138–145 (2015).
3. Mousazadeh, H., A. Keyhani, A. Javadi, H. Mobli, K. Abrinia, & A. Sharifi. A review of principle and sun-tracking methods for maximizing solar systems output. *Renewable and Sustainable Energy Reviews* 13(8) : 1800–1818 (2009).
4. Lewis, N., G. Crabtree, J. Nozik, M. Wasielewski, & P. Alivisatos. Basic research needs for solar energy utilization. In: *Proceedings of Basic Energy Sciences Workshop on Solar Energy Utilization*, p. 7–10 (2005).
5. Waleed, A., K. Hassan, & U. Virk. Designing a dual axis solar tracker for optimum power. *Journal of Electrical Engineering* 14(2) :173–178 (2014).
6. Samad, P., F. Xiumei, & N. Sangi. Current power generation and alternative trends in Pakistan. *Science International* 28(3) : 2321–2325 (2016).
7. Kumar, B. A study on global solar PV energy developments and policies with special focus on the top ten solar PV power producing countries. *Renewable and Sustainable Energy Reviews* 43: 621–634 (2015).
8. Huynh, D.C., T. Nguyen, M.W. Dunnigan, & M. Mueller. Comparison between open- and closed-loop trackers of a solar photovoltaic system. In: *IEEE Conference on Clean Energy and Technology (CEAT)*, p. 128–133 (2013).
9. Tania, H., & M. Alam. Sun tracking schemes for photovoltaic panels. In: *Proceedings of 3rd International Conference on the Developments in Renewable Energy Technology (ICDRET)*, p.1–5 (2014).

10. Finster, C. The heliostat of the Universidad Santa Maria. *Scientia* 119: 5–20 (1962).
11. Saavedra, A. Design of a solar tracking servomechanism for a recording instrument of the direct solar irradiation. *Scientia* 122: 40–48 (1963).
12. Ferdous, R.A., M. Mohammed, S. Rahman, S. Salehin, & M. Mannan. Energy efficient hybrid dual axis solar tracking system. *Journal of Renewable Energy* 14(1): 1–12 (2014).
13. Benner, R. *Zomeworks Corporations*. Available: <http://www.zomeworks.com/>. [Accessed: 16 Oct., 2016].
14. Khaliq, A., A. Ikram, & M. Salman. Quaid-e-azam solar power park : prospects and challenges. In: *Proceedings of IEEE Conference on Power Generation Systems and Renewable Energy Technology*, p. 1-6 (2015).
15. Lee, C.Y., P. Chou, C. Chiang, & C.F. Lin. Sun tracking systems: a review. *Sensors* 9(5): 3875–3890 (2009).
16. *Solar Tracker*. Wikiwand. Available: http://www.wikiwand.com/en/Solar_tracker. [Accessed: 18 Oct., 2016].
17. Akhmedyarov, K.A., B.A. Bazarov, & B. Ishankuliev. Economic efficiency of the FV-500 solar photoelectric station with automatic tracking of the sun. *Applied Solar Energy* 22: 44–47 (1986).
18. Moniruzzaman, H.M., M. Patwary, & M. Rahman. A three level solar panel system with an automated solar tracker. In: *Proceedings of 3rd International Conference on the Developments in Renewable Energy Technology (ICDRET)*, p. 1–7 (2014).
19. Zenan, A.H., S. Ahmed, M.K. Rhaman, & M. Rahman. A new multilevel solar panel system for urban areas. In: *Proceedings of IEEE Photovoltaic Specialists Conference (PVSC)*, p. 1526–1530 (2013).
20. Anuraj, A., & R. Gandhi. Solar tracking system using stepper motor. *International Journal Electronic and Electrical Engineering* 7(6) :561–566 (2014).
21. Kivrak, S., M. Gunduzalp, & F. Dincer. Theoretical and experimental performance investigation of a two-axis solar tracker under the climatic condition of Denizli, Turkey. *Przeglad Elektrotechniczny* 88(2): 332–336 (2012).
22. Mahmood, O. Programmable logic controller based design and implementation of multiple axes solar tracking system. In: *Proceedings of International Conference on Electrical, Communication, Computer, Power, and Control Engineering (ICECCPCE)* 1: 101–106 (2013).
23. Afrin, F., & T. Titirsha. Installing dual axis solar tracker on rooftop to meet the soaring demand of energy for developing countries. In: *Proceedings of IEEE India Conference (INDICON)*, p. 1-5 (2013).
24. Titirsha, T., & A. Siddique. Introducing dual axis solar tracker with reflector to increase optimal electricity generation in bangladesh. In: *Proceedings of 3rd International Conference on the Developments in Renewable Energy Technology (ICDRET)*, p. 127-133 (2014).
25. Bajpai, P., & S. Kumar. Design, development and performance test of an automatic two-axis solar tracker system. In: *Proceedings of IEEE India Conference: Engineering Sustainable Solutions (INDICON)*, p. 1-6 (2011).
26. Clifford, M.J., & D. Eastwood. Design of a novel passive solar tracker. *Solar Energy* 77(3): 269–280 (2004).
27. Mehmood, A., A. Shaikh, & A. Waqas. Modeling of the solar photovoltaic systems to fulfill the energy demand of the domestic sector of Pakistan using RETSCREEN software. In: *Proceedings of International Conference and Utility Exhibition on Green Energy for Sustainable Development (ICUE)*, p. 19–21 (2014).
28. Sabir, M. *Analysis and Experimentation of a Passive Solar Tracker*. MS thesis, University of Khartoum, Sudan (2015).
29. Parmar, A., A. Narendrasinh, & V.S. Gautam. Passive solar tracking system. *International Journal of Emerging Technology and Advcd Engineering* 2(3): 80–89 (2013).



Design of Broadband Matching Network for Complex Reactive Load using L-Matching

Jawad Yousaf*, Zubair Mehmood, Waseem Abbas, and Khuram Shehzad

Department of Electrical and Electronics Engineering,
Sungkyunkwan University, Suwon, Republic of Korea

Abstract: In this work, effect of single and multisection matching with and without ideal lumped components on the impedance matching bandwidth was analyzed. Single and multisection L-matching networks are designed for parallel reactive (RC) load configuration at 10 GHz. The analysis showed that higher section matching with ideal components did not produce significant improvement in fractional bandwidth of matching network for complex parallel RC load. However, more wider impedance bandwidth can be obtained with lower section matching constituting of finite component quality factor (Q) lumped components.

Keywords: L-matching, broadband impedance matching, ideal/non-ideal lumped matching

1. INTRODUCTION

Matching networks are designed to ensure the maximum power transfer between the transmitter and receiver at the desired frequency range [1]. The maximization of the power transfer reduces the input reflection which is essential at every interface of the complete RF network for the achievement of higher overall efficiency of network. Both kinds of short and broadband conjugate matching network are designed depending on the requirements of the RF product or system [2, 3]. Besides the maximum power transfer, impedance matching is done to minimize the noise figure in low noise amplifier (LNA), achievement of maximum saturated output power for the power amplifiers (PA) and minimization of the ripples in the gain response of transmission line terminations [2 - 6]. Also the commercial ports of all RF products are designed with $50\ \Omega$ source and load impedance which also invokes the needs of impedance matching [7, 8]. Fig. 1 illustrate the typical source and load side impedance matching networks. Matching bandwidth is defined as the range for which the input reflection i.e. S_{11} is lower than the threshold or the transfer characteristics, i.e., S_{21} are higher than the threshold.

The typical values of S_{11} and S_{21} threshold are -10 dB -3 dB respectively [1]. The matching network which has around 10 % fractional bandwidth is termed as narrow-band matching network, while the network with more than 30 % fractional bandwidth is known as broadband matching network [9]. L-matching, T-matching and single stub transmission line matching networks are common choices for the narrow band matching. For the broadband matching, multisection L/T matching, multisection quarter-wave transformer and tapered line matching are recommended [7, 8]. The lossless or low loss matching (with components having high quality factor Q like capacitors, inductors, transmission lines and transformers) have no or minimal power loss, and is usually results in narrow band matching [3-6]. The usage of lossy components having finite Q have power losses increase the power losses. However finite Q value increase the insertion loss which results in broadband matching.

In this work, we are presenting an analysis of the effect of single and multisection matching network with ideal and non-ideal passive components on the matching bandwidth. The single and multisection L-matching network are designed for the parallel RC load impedance using the step-down transformation. Non-ideal components are modeled by using finite Q characteristics of those components in circuit simulator. Advanced design system [10] is used for the simulation of all matching circuits. Fractional bandwidth is calculated and compared for all matching strategies. Details of the matching network design strategy and analysis of results for ideal and lossy components are elaborated in the following sections.

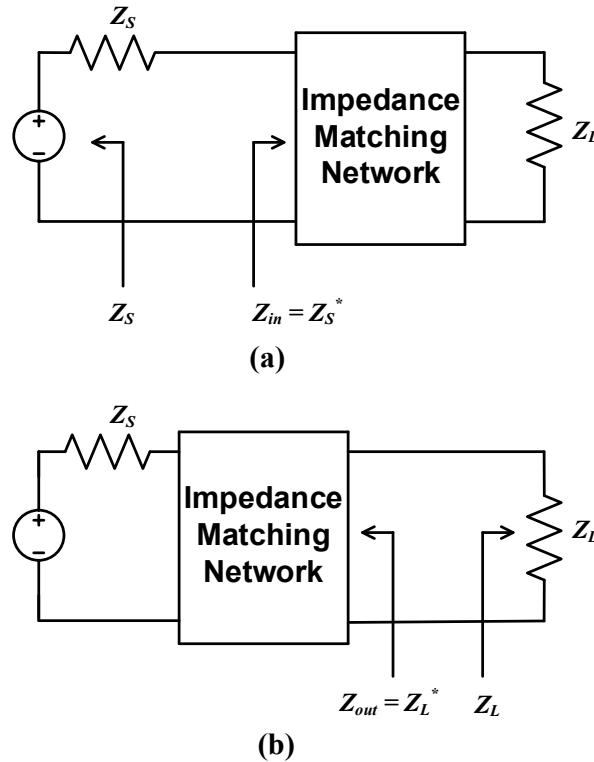


Fig. 1. Impedance matching network: (a) Source side matching; (b) Load-side matching.

2. LOAD CONFIGURATION

The analysis is performed for the a complex load impedance configuration constituting of resistive and capacitive components. The purpose is to the evaluate the effect of different matching strategies for the prototype load. Fig. 2 shows the load configuration. The load impedance contains a parallel network of resistor ($R=200\ \Omega$) and capacitor ($C=1.2\ pF$). This complex load impedance (Z_L) needs to be matched with standard $50\ \Omega$ source impedance (Z_S).

3. L-MATCHING

L-matching is categorized into two classes: step-up and step-down transformation. Fig. 3 depicts the difference between these two classes. Step-up transformation is done when the source impedance is higher than the load impedance. For the case where load impedance is higher than source impedance, step down transformation is applied. The main difference occurs in the calculations of the transformation ratio (m) and transformation quality factor (Q) depending on the type of the selected transformation. Fig. 2 in our case, is the step down transformation scenario.

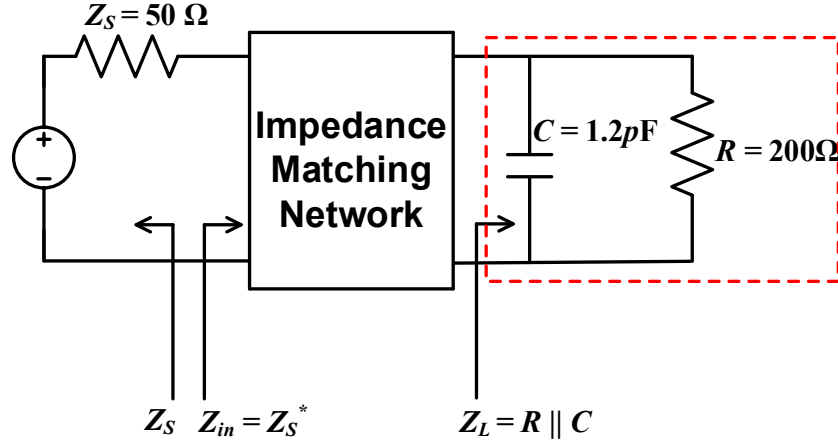


Fig. 2. Load impedance details.

The value of m and Q for a single section L-matching are computed using the Eq. 1. The computation of matching network components is dependent on the calculated values of m and Q .

$$\begin{aligned}
 m &= \frac{R_S}{R_L} \rightarrow \text{for step-up} \\
 m &= \frac{R_L}{R_S} \rightarrow \text{for step-down} \\
 Q &= (m - 1)^{\frac{1}{2}}
 \end{aligned} \tag{1}$$

For a multisection step-down transformation scenario as shown in Fig. 4.

The overall transformation ratio (m), overall transformation Q , per-stage ratio of transformation (m_i) and per-stage transformation (Q_i) can be computed as follows [1]:

$$\begin{aligned}
 \text{Overall Transformation Ratio: } m &= \frac{R_L}{R_S} = m_i^N \\
 \text{Overall Transformation - } Q: Q &= (m - 1)^{\frac{1}{2}} \\
 \text{Per - Stage Transformation Ratio: } m_i &= \left(\frac{R_L}{R_S} \right)^{\frac{1}{N}} \\
 m_i &= \frac{R_L}{R_{i1}} = \frac{R_{i1}}{R_{i2}} = \frac{R_{i2}}{R_{i3}}, \dots, = \frac{R_{i(N-1)}}{R_{iN}} \\
 \text{Per - Stage Transformation - } Q: Q_i &= (m_i - 1)^{\frac{1}{2}}
 \end{aligned} \tag{2}$$

For a step-up transformation, the position of the R_L and R_S can be exchanged in the above design steps.

4. MATCHING STRATEGY WITH IDEAL COMPONENTS

The impedance matching network for the load impedance of Fig. 2 are designed using step-down L-matching technique. Three kinds of matching network: single section, double section and triple section are designed. It should be noted that the complex load impedance needs to be converted to pure resistive impedance for the start of the impedance matching process using L section matching. For the complex load of Fig. 2, a shunt inductive component has to be added across the capacitive components to cancel the effect of complex components of load impedance.

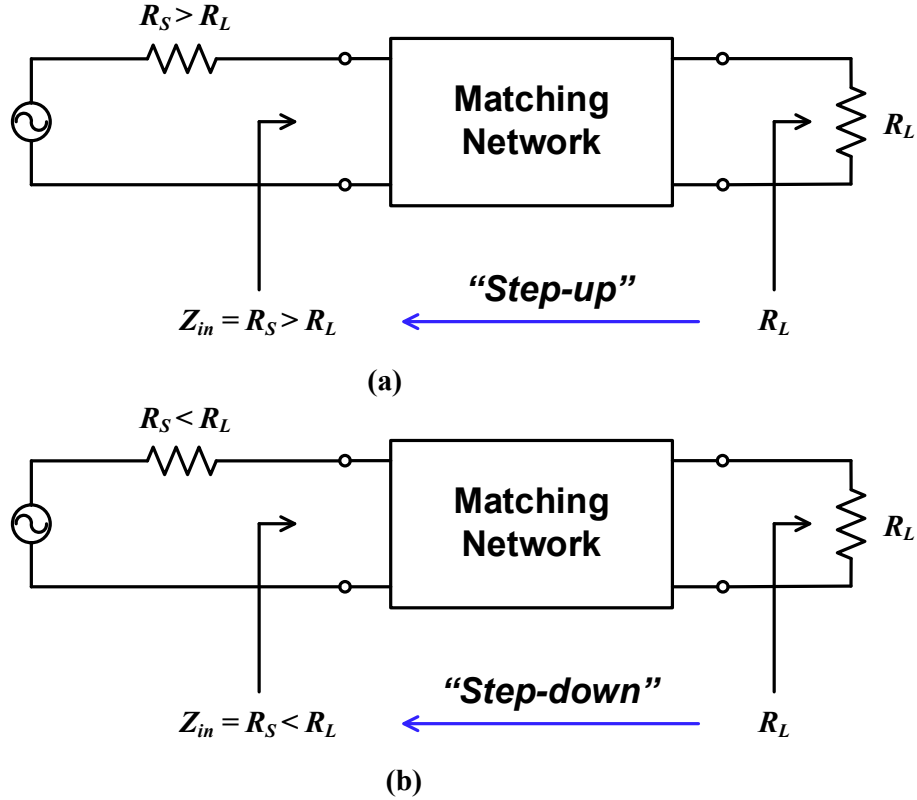


Fig. 3. L-matching configurations (a) Step-up transformation (b) Step-down transformation.

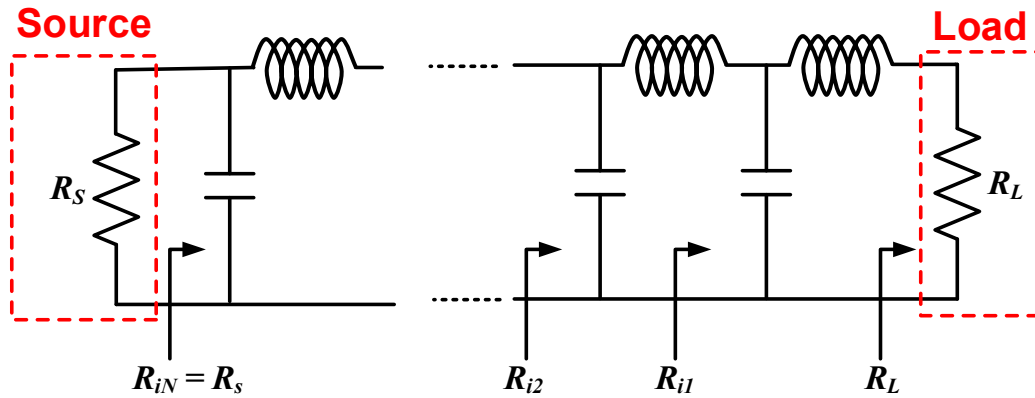


Fig. 4. Multisection L-matching configuration for step-down transformation ($R_S < R_L$).

The value of the shunt inductive element is calculated to make the complex part of the load impedance to zero. The value of L_{shunt} can be computed using the Eq. 3 at design frequency $f = 10 \text{ GHz}$. The adding of L_{shunt} makes the load impedance pure resistive i.e $Z_L = R_L = 200\Omega$. The values of this shunt inductive component can be combined with the final matching components of impedance matching network.

$$L_{shunt} = \frac{1}{\omega^2 C} = 0.211 \text{ nH} ; \omega = 2 \pi f \quad (3)$$

The comparison of the fractional bandwidth for each case is illustrated in the following subsections.

4.1 Single Section L-matching

The design steps for the single section L -matching with $R_L = 200 \Omega$ and $R_s = 50 \Omega$ based on Eq. 2 are given below.

$$m = \frac{R_L}{R_s} = 4$$

$$Q = (m - 1)^{\frac{1}{2}} = 1.73$$

$$X_{L1} = \frac{R_L}{Q} = 115.47 \Omega$$

$$L_1 = \frac{X_{L1}}{\omega} = 1.83 \text{ nH}$$

$$X_{C1} = Q \times R_s = 86.5 \Omega$$

$$C_1 = \frac{1}{\omega C} = 0.183 \text{ pF}$$

For the single section matching, the value of combined inductance of matching network is 0.189 nH . Table 1 depicts the all parameters of the single section L -matching. The designed matching network is simulated in ADS and its schematic is shown in Fig. 5. As depicted from the smith chart result [Fig. 6], the network is perfectly matched with the 50Ω source load. The simulated S -parameters of the designed single section matching network are shown in Fig. 7. The fractional bandwidth of the matching network is computed using the formula of Eq. 4. For the single section matching network, the fractional bandwidth is 4.04 % which can be computed from Fig. 7.

$$\text{Fractional Bandwidth} = \frac{f_{\text{high}|limit} - f_{\text{low}|limit}}{f_r} \% ; \text{ Where } limit = S_{11} \leq -10\text{dB} \quad (4)$$

Table 1. Single section L-matching parameters.

	1st Section
m	4
Q	1.73
$L_{\text{shunt}} (\text{nH})$	0.211
$X_L (\Omega)$	115.4
$L (\text{nH})$	1.83
$X_C (\Omega)$	86.5
$C (\text{pf})$	0.183
$Z_{\text{in}} (\Omega)$	50.0

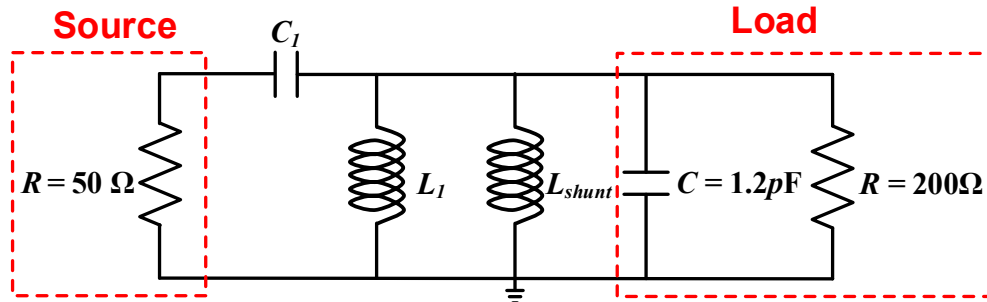


Fig. 5. Single section matching network (see Table 1 for Component values).

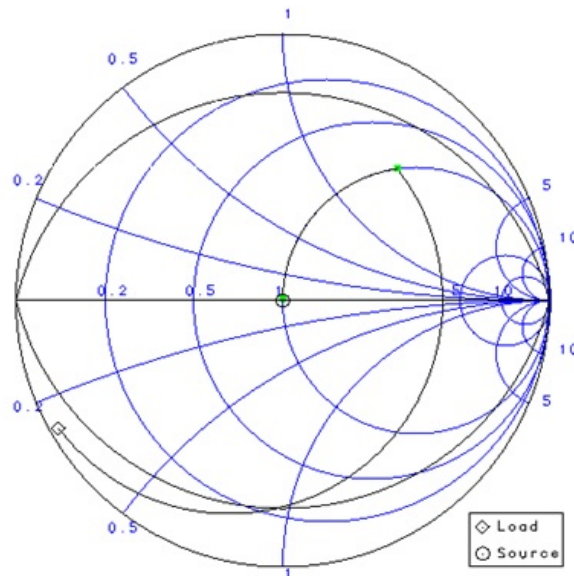


Fig. 6. Smith chart results of single section matching network.

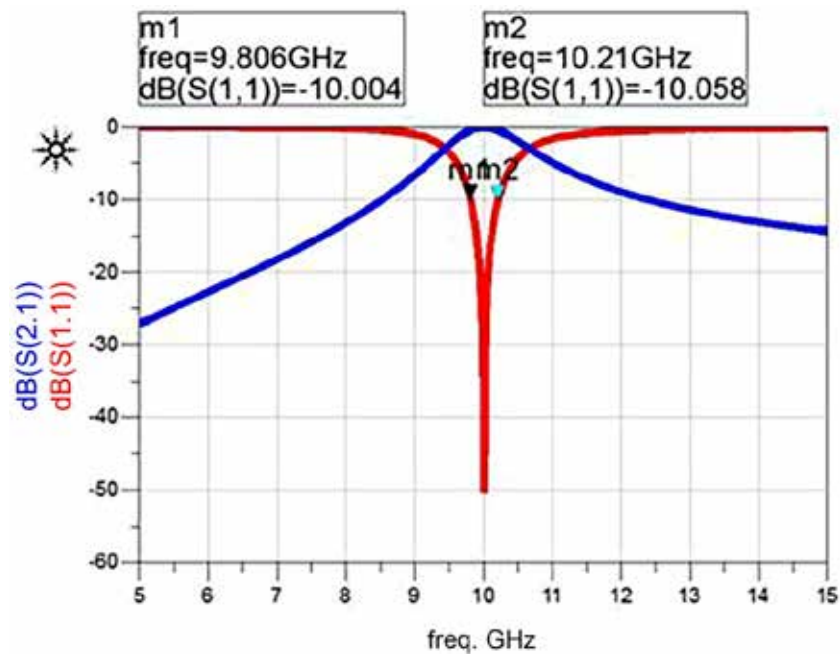


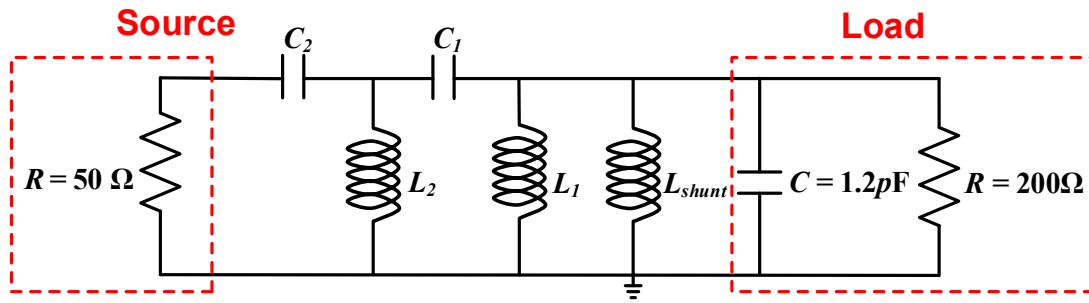
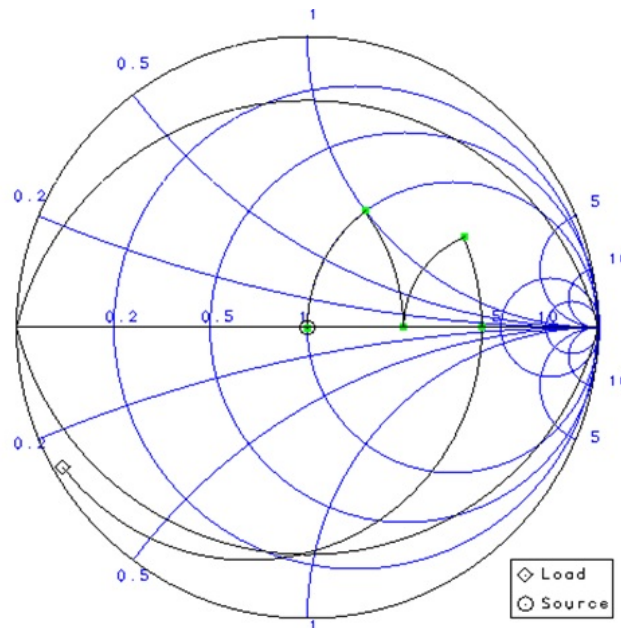
Fig. 7. S-parameter results of single section matching network.

4.2 Double Section L-matching

The parameters of the designed dual section *L*-matching network are computed using Eq. 2 and are shown in Table 2. The matching network is designed using the calculated parameters of Table 2 and its ADS schematic is shown in Fig. 8. Smith chart and scattering parameters of the matching network are shown in Fig. 9 and 10, respectively. The simulated fractional bandwidth in this case [Fig. 10] is 4.15 %.

Table 2. Double section L-matching parameters.

	1st Section	2nd Section
m	2	2
Q	1	1
$L_{shunt} (nH)$	0.211	
$X_L (\Omega)$	200	100
$L (nH)$	3.18	1.59
$X_C (\Omega)$	100	50
$C (pf)$	0.159	0.318
$Z_{in} (\Omega)$	150	50.0

**Fig. 8.** Double section matching network (see Table 2 for Component values).**Fig. 9.** Smith chart results of double section matching network.

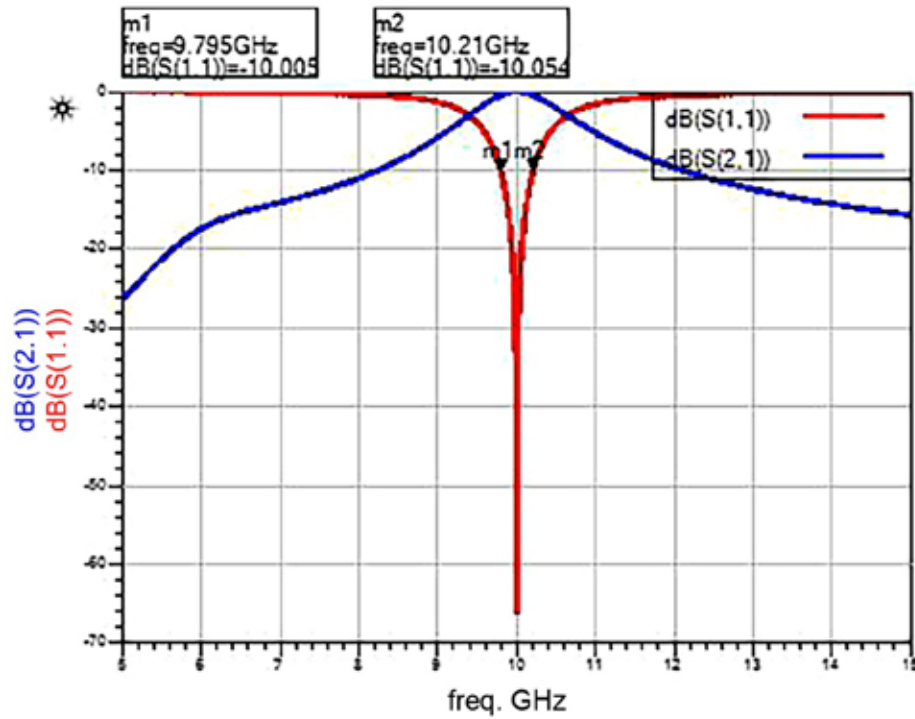


Fig. 10. S-parameter results of double section matching network.

4.3 Triple Section L-matching

The triple section matching network constitutes of three individual networks of L and C . Table 3 illustrate the parameters values for this scenario which can be computed using Eq. 2. Fig. 11 depicts the circuit diagram of the triple section L -matching network with source and load. Scattering parameter results for this case are shown in Fig. 13. It can be noted from Fig. 13 that triple section matching network exhibit only 4.21 % which is slight higher than single and double section matching networks but still is quite low.

Table 3. Triple section L-matching parameters.

	1st Section	2nd Section	Third Section
m	1.58	1.58	1.58
Q	0.76	0.76	0.76
$L_{shunt} (nH)$		0.211	
$X_L (\Omega)$	260.95	164.39	103.55
$L (nH)$	4.153	2.616	1.648
$X_C (\Omega)$	95.56	60.83	38.32
$C (pf)$	0.1648	0.2616	0.415
$Z_{in} (\Omega)$	125.9	79.37	50.0

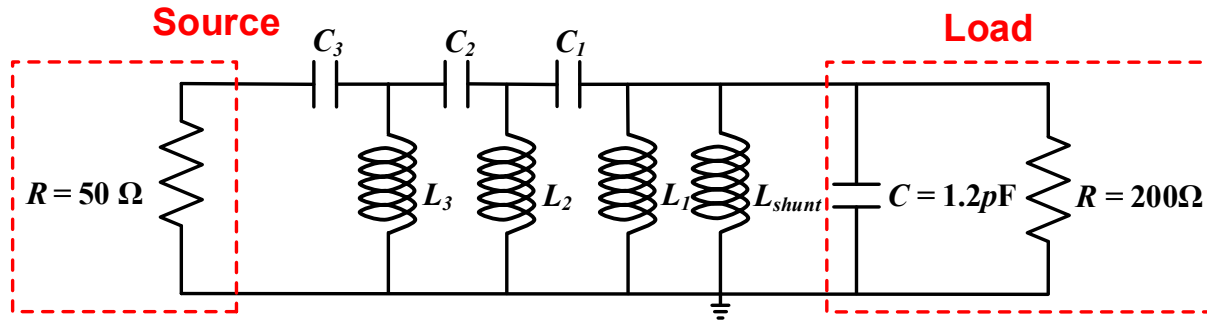


Fig. 11. Triple section matching network (see Table 3 for Component values).

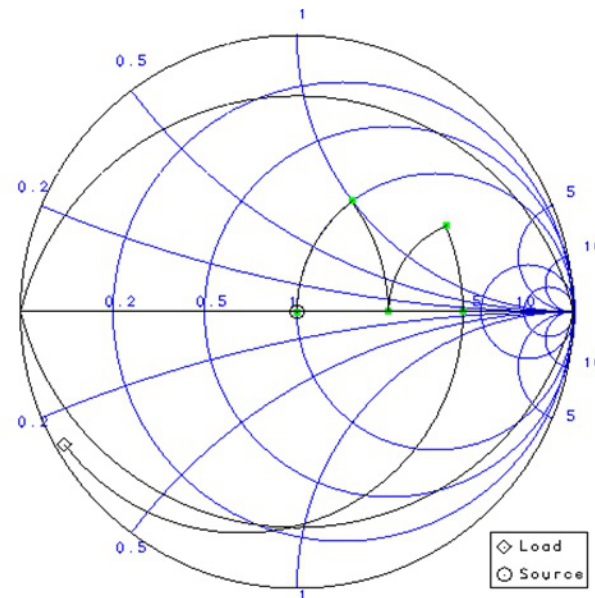


Fig. 12. Smith chart results of triple section matching network.

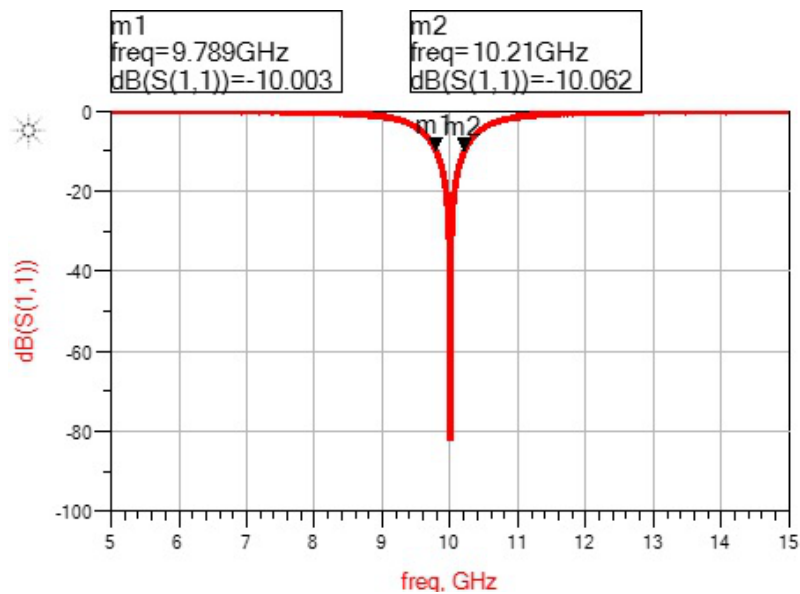


Fig. 13. S-parameter results of triple section matching network.

4.4 Four Section L-matching

The designed parameter for the four section matching are shown in Table 4. ADS schematic of the four section L -matching network is depicted in Fig. 14. Fig. 15 and Fig.16 show the simulated smith chart and S -parameters results of the the designed matching network respectively. The computed fractional bandwidth of this higher section matching network (4.35 %) is still lower than even 10 % of the narrow-band matching network limit.

Table 4. Fourth section L-matching parameters.

	1st Section	2nd Section	Third Section	Fourth Section
m	1.41	1.41	1.41	1.41
Q	0.64	0.64	0.64	0.64
$L_{shunt} (nH)$			0.211	
$X_L (\Omega)$	310.7	219.73	155.37	109.86
$L (nH)$	4.958	3.497	2.472	1.748
$X_C (\Omega)$	91.018	64.359	45.509	32.179
$C (pf)$	0.174	0.247	0.349	0.494
$Z_{in} (\Omega)$	141.42	100.0	70.71	50.0

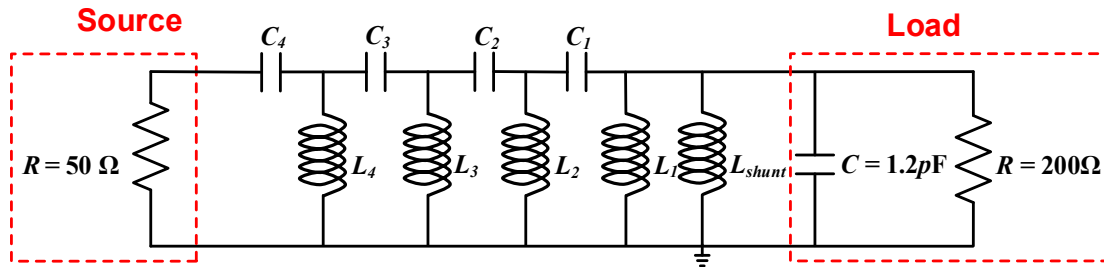


Fig. 14. Fourth section matching network (see Table 4 for Component values).

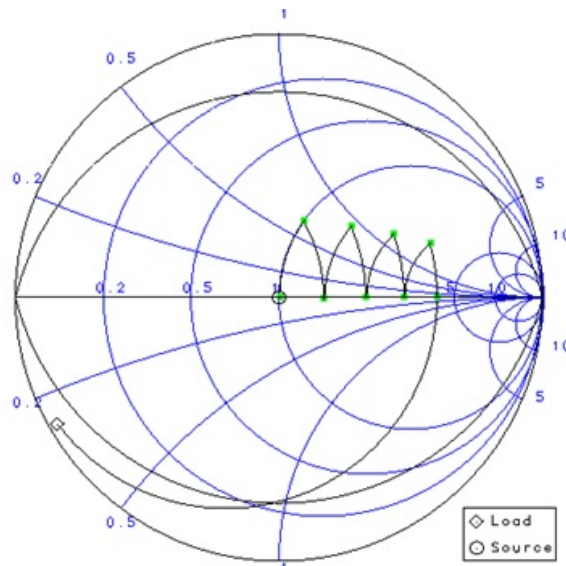


Fig. 15. Smith chart results of fourth section matching network.

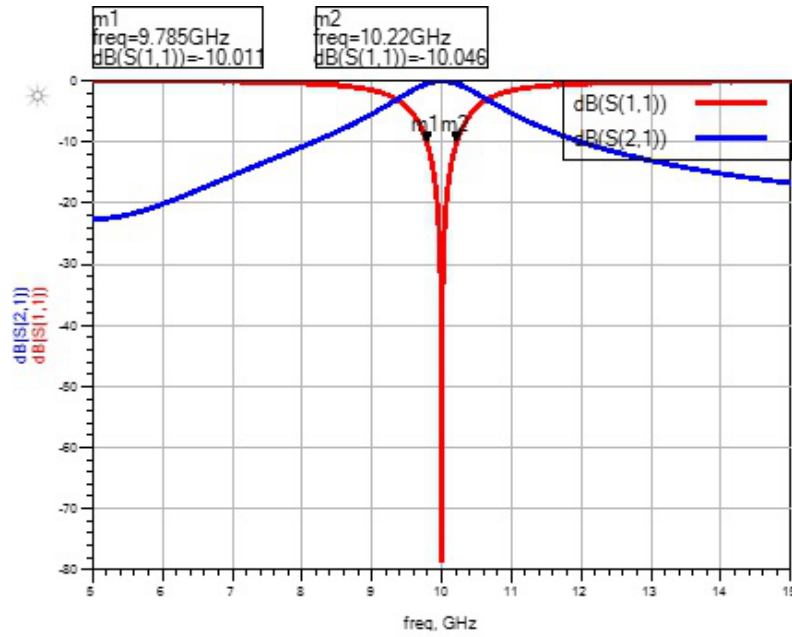


Fig. 16. S-parameter results of fourth section matching network.

4.5 Comparison of Results

The comparison of the fractional bandwidth for all four cases of single, double, triple and four section L -matching network is shown in Fig. 17. The results of Fig. 17 depicts that even the increase in number of matching section did not produce any significant improvement in the fractional bandwidth. The fractional bandwidth improvement difference is also not very high with the increase in matching network from three to four section. It shows that higher fractional bandwidth of more than 10 % or 30 % cannot be achieved with the ideal lumped components used for the all cases of single and multisection matching networks. For the achievement of broadband matching, the non-ideal components are good choice. The details of the enhancement in the matching bandwidth with non-ideal lumped components is elaborated in next section.

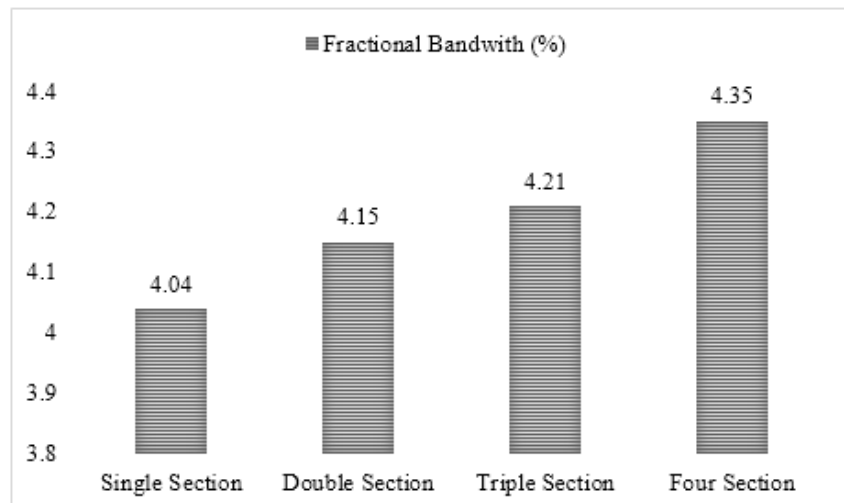


Fig. 17. Comparison of single and multisection L -matching with ideal L/C .

5. MATCHING STRATEGY WITH NON-IDEAL COMPONENTS

The fractional bandwidth can be increased by using lossy L and C components. The lossy L/C are modeled using finite Q value in the circuit simulation environment of ADS. The selected individual Q value for the lossy components is 2. The value of 2 is chosen after the turning of the matching network for good results. The schematic of the matching network with finite Q for triple section matching network is similar to shown in Fig. 11 with same component values as shown in Table 3 with the finite Q values. Fig. 18 reflects the comparison of the increase in the fractional bandwidth with the lossy L/C . Fig. 18 shows that fractional bandwidth for the three-section L -matching network with finite Q is 62.8 %. The lower section matching did not produce good results for the fractional bandwidth with the finite Q values.

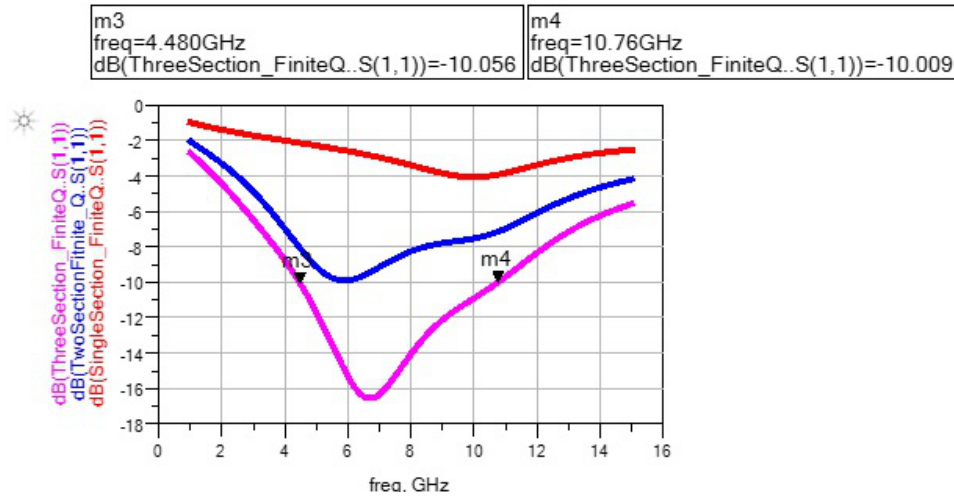


Fig. 18. Comparison of multisection L -matching with finite component Q .

6 COMPARISON OF IDEAL AND LOSSY MATCHING

The comparison of the fractional bandwidth of the matching network with lossy and ideal components is discussed in this section. Fig. 19 depicts the differences between the fractional bandwidth with ideal and lossy components having finite Q . It shows that significant improvement in fractional bandwidth (around 60 %) is observed for the three section L -matching network with ideal (infinite component Q) and lossy components (finite component Q). This increase in bandwidth is due to the reduction in the insertion loss of the matching network with finite component Q .

The insertion loss for the multisection L -matching network can be written as in Eq. 5 [1]. The adding of additional sections lower the Q values which eventually reduces the insertion loss. However the optimum number of matching network has to be chosen as the adding of too many matching networks can counterbalance the benefit of lowering of the insertion loss and consequentially improvement in the fractional bandwidth of the matching network [1, 2, 6].

$$Insertion\ Loss\ (IL) \equiv \frac{P_L}{P_{in}} = \left(\frac{1}{1 + \frac{Q_i}{Q_c}} \right)^{2N} \quad (5)$$

$$IL \cong \frac{1}{1 + 2N \left(\frac{Q^{\frac{1}{N}}}{Q_c} \right)}$$

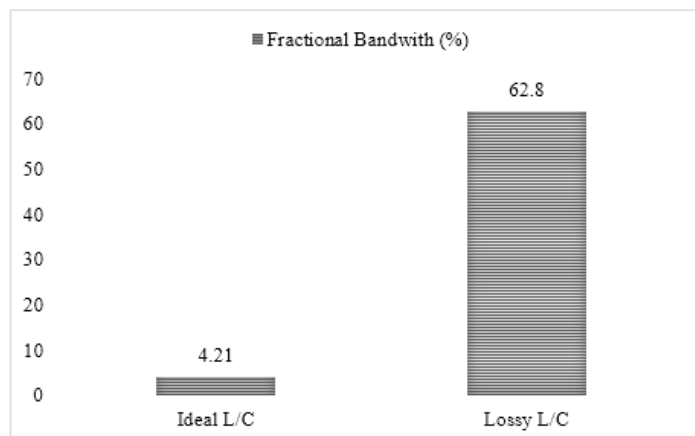


Fig. 19. Comparison of three-section L-matching with Finite and Infinite Q .

7 CONCLUSIONS

This study has presented an in-depth analysis of effect of ideal and lossy components on bandwidth of the matching network using L-matching. The ideal components produces very low fractional bandwidth even with four-section L-matching, for a complex load of $200 \Omega || 1.2 pF$. The three-section L-matching with finite component Q value of 2 produces the 62.8 % fractional bandwidth. The lowering of quality factor of individual components of the matching network reduces the insertion loss values and, hence, results in a wider bandwidth of the matching circuit. The presented design of three-section L-matching with finite Q value produces approximately 63 % matching bandwidth for $S_{11} \leq -10$ dB.

8. ACKNOWLEDGMENTS

We would like to thank Mr. Zaffar Hayat Nawaz Khan for his interactive discussions on impedance matching.

9. REFERENCES

1. Amin, M., J. Yousaf, & S. Iqbal. Single feed circularly polarised omnidirectional bifilar helix antennas with wide axial ratio beamwidth. *IET Microwaves, Antennas Propagation* 10: 825–830 (2013).
2. Chen, L-Y V., R. Forse, D. Chase, & R.A. York. Analog tunable matching network using integrated thin-film bst capacitors. In: *Proceedings Microwave Symposium Digest, 2004 IEEE MTT-S International*, p. 261–264 (2004).
3. Oraizi, H. & A-R Sharifi. Design and optimization of broadband asymmetrical multisection wilkinson power divider. *IEEE Transactions on Microwave Theory and Techniques* 54: 2220–2231 (2006).
4. Pozar, D. *Microwave Engineering*. John Wiley & Sons, NJ, USA (2009).
5. Vendelin, G.D., A.M. Pavio, & U.L. Rohde. *Microwave Circuit Design using Linear and Nonlinear Techniques*. John Wiley & Sons, NJ, USA (2005).
6. Yang, Y., J. Yi, Y.Y. Woo, & B. Kim. Optimum design for linearity and efficiency of a microwave doherty amplifier using a new load matching technique. *Microwave Journal* 44: 20-36 (2001).
7. Yousaf, J., H. Jung, K. Kim, & W. Nah. Design, analysis, and equivalent circuit modeling of dual band pifa using a stub for performance enhancement. *Journal of Electromagnetic Engineering and Science* 16: 169–181 (2016).
8. Yousaf, J., M. Amin, S. Iqbal, & H. Durrani. Analysis of conducted emission measurements of dc-dc converter with load for proper filter design. *International Journal of Microwave and Optical Technology* 10: 464–470 (2015).
9. Yousaf, J., M. Amin, & S. Iqbal. Circularly polarized wide axial ratio beamwidth omnidirectional bifilar helix antennas. In: *Proceedings IEEE First AESS European Conference on Satellite Telecommunications (ESTEL)*, p. 1–6 (2012).
10. *Advanced Design System (ADS)*. KEYSIGHT Technologies (2017) <http://literature.cdn.keysight.com/litweb/pdf/5988-3326EN.pdf?id=921864>.



On Classes of Analytic Functions Associated by a Parametric Linear Operator in a Complex Domain

Rabha W. Ibrahim¹, Adem Kilicman², and Zainab E. Abdulnaby^{2,3,*}

¹Faculty of Computer Science and Information Technology, University of Malaya, 50603, Malaysia

²Department of Mathematics, Faculty of Science, Universiti Putra Malaysia,
43400 UPM Serdang, Selangor, Malaysia

³Department of Mathematics, College of Science, Al-Mustansiriyah University, Baghdad, Iraq

Abstract: The present paper deals with some geometric classes of analytic functions, such as starlike, convex and bounded turning property in a complex domain. These classes are defined by a new linear operator in the normalized space of analytic functions. The linear operator is introduced by a convolution of Szego function involving parametric coefficients type *Laguerre* polynomial, with the normalized function. Sufficient conditions on this operator are illustrated to study the geometric properties. Our tool is based on some recent results in this direction. The main strategy for this work is to provide parametric functional inequalities in the open unit disk.

Keywords: analytic functions, univalent function, starlike function; convex function, bounded turning function, *Laguerre* polynomial, convolution (or Hadamard product), Riemann zeta function

1. INTRODUCTION

Special function is a major topic in classical analysis which deals with class of mathematical functions and that may arise in the solution of various classical problems of some branch of mathematics and mathematical physics. In particular, most special functions are considered as a function of a complex variable. An intricate special function can be expressed in terms of simpler function and the simplest way to assess a function is to expand it by a Taylor series.

Further, special functions have proven their eligibility in associated with an analytic function via convolution technique (or Hadamard product) to define, prove, represent and extend several types of operators, here we suggest a number of the well-known and recent linear operators defined according to special function (see [1-5]). Hohlov [6] derived sufficient conditions that guarantee such mappings for the operator defined by means of the Hadamard product with the Gauss hypergeometric function. Carlson and Shaffer [7] adopted the incomplete beta function to define a linear operator, which has been widely used in the space of analytic and univalent functions in the open unit disk \mathbb{U} (see [8]). After more decades Dzoik and Srivastava [9] investigated a convolution linear operator which has been formulated in terms of the generalized hypergeometric function. Several interesting properties and characteristics of the Dziok–Srivastava operator are derived (see [10], [20]). Following, by interesting related work, Srivastava [11] determined also, another extension covering the Wright function which is known as Srivastava-Wright operator (see [12]). Recently, in Srivastava and Attiya [13] defined an integral operator in terms of convolution with Hurwitz–Lerch Zeta function and studied some differential subordination results associated with the operator. It is worth mentioning that, Srivastava-Attiya operator is a generalized of many operators.

Ibrahim [14] introduced a linear operator for analytic functions derived by using the basic hypergeometric series, also investigated some applications of differential subordinate on Jack's lemma.

The paper is organized as follows: Section 2 revises a new linear operator in the normalized space of analytic functions is defined. The linear operator is introduced by a convolution of Szego function involving parametric coefficients type *Laguerre* polynomial, with the normalized function. Further, some geometric classes of analytic functions, such as starlike, convex and bounded turning property in a complex domain are investigated in Section 3. These classes are sufficient conditions on this operator are illustrated to study the geometric properties. Our method is based on some recent results in this direction. The main strategy of this work is to provide parametric functional inequalities in the open unit disk.

2. PRELIMINARIES

Let \mathcal{A} denote the class of functions of the form

$$f(z) = z + \sum_{k=2}^{\infty} a_k z^k = z + a_2 z^2 + a_3 z^3 \dots, \quad a_1 = 1 \quad (1)$$

which are analytic in the open unit disk $\mathbb{U} := \{z \in \mathbb{C} : |z| < 1\}$ normalized by $f(0) = 1 - f'(0) = 0$, and let \mathcal{S} be the subclass of the \mathcal{A} of the univalent functions in \mathbb{U} . Further, a function $f(z) \in \mathcal{S}$ is said to be starlike and convex, if their geometric condition satisfies

$$\Re \left\{ \frac{z f'(z)}{f(z)} \right\} > 0 \quad \text{and} \quad \Re \left\{ 1 + \frac{z f''(z)}{f'(z)} \right\} > 0,$$

respectively, these subclasses of \mathcal{S} are denoted by \mathcal{S}^* and \mathcal{K} . The convolution (or Hadamard product), between two analytic functions, function of the form (1) and $g(z) = z + \sum_{k=2}^{\infty} b_k z^k$ in \mathbb{U} , is defined by

$$(f * g)(z) = z + \sum_{k=2}^{\infty} a_k b_k z^k = (g * f)(z). \quad (2)$$

A function of bounded turning \mathcal{B} if it satisfies the inequality

$$\Re \{f'(z)\} > 0, \quad z \in \mathbb{U}.$$

We begin our current consideration by recalling that a generating function of the associated *Laguerre* polynomials $G(b, \tau, z)$ defined by Szego [15].

$$G(b, \tau, z) = (1 - z)^{-b-1} e^{(-\tau z / (1-z))} = \sum_{k=0}^{\infty} L_k^{(b)}(\tau) z^k, \quad z \in \mathbb{U} \quad (3)$$

$$(b \in \mathbb{C} \setminus \{-1, -2, \dots\}; \Re(b) > 1; \tau \in \mathbb{R}; |z| < 1)$$

where $L_k^{(b)}(\tau)$ is the form of generalized Laguerre polynomials of degree k on the interval $(0, \infty)$, is given by

$$\begin{aligned} L_k^{(b)}(\tau) &= \sum_{i=0}^k \binom{k+b}{k-i} \frac{(-\tau)^i}{i!}, \quad k = 0, 1, \dots \\ &= b + \binom{1+b}{1} - \binom{1+b}{0} \tau + \binom{2+b}{2} - \binom{2+b}{1} \tau + \binom{2+b}{0} \frac{\tau^2}{2!} + \dots \end{aligned} \quad (4)$$

where $\binom{\alpha}{\mu}$ is the generalized binomial coefficient

$$\binom{\alpha}{\mu} = \frac{\Gamma(\alpha + 1)}{\Gamma(\mu + 1)\Gamma(\alpha - \mu + 1)}.$$

Now, for $f \in \mathcal{A}$, $b \in \mathbb{C} \setminus \{-1, -2, \dots\}$ and $\tau \in \mathbb{R}$, let define the function $\Lambda(b, \tau, z)$ by

$$\Lambda(b, \tau, z) = \frac{G(b, \tau, z)}{L_1^{(b)}(\tau)}, \quad (z \in \mathbb{U}) \quad (5)$$

where

$$L_1^{(b)}(\tau) = \binom{1+b}{1} - \binom{1+b}{0}\tau \neq 0,$$

We proceed to define a linear operator $\mathcal{G}_\tau^b : \mathcal{A} \rightarrow \mathcal{A}$ by

$$\mathcal{G}_\tau^b f(z) = \Lambda(b, \tau, z) * f(z), \quad (6)$$

$$(f \in \mathcal{A}; z \in \mathbb{U}; \tau \in \mathbb{R}; b \in \mathbb{C} \setminus \{-1, -2, \dots\})$$

by the following Hadamard product (2), we obtain

$$\mathcal{G}_\tau^b f(z) = z + \sum_{k=2}^{\infty} \Omega_{b,k}(\tau) a_k z^k \quad (z \in \mathbb{U}), \quad (7)$$

where

$$\Omega_{b,k}(\tau) = \frac{L_k^{(b)}(\tau)}{L_1^{(b)}(\tau)}, \quad L_1^{(b)}(\tau) \neq 0. \quad (8)$$

Remark 2.1: From (7) and (8), we have

$$\mathcal{G}_\tau^0 f(z) = \lim_{b \rightarrow 0} \{\mathcal{G}_\tau^b f(z)\}. \quad (9)$$

It is clear that

$$\mathcal{G}_0^0 f(z) = z + \sum_{k=2}^{\infty} a_k z^k = f(z) \quad \text{and} \quad \mathcal{G}_0^{\alpha-1} f(z) = z(1-z)^{-\alpha}.$$

Using the relation (7), we obtain

$$z \left(\mathcal{G}_\tau^{b+1} f(z) \right)' = b \mathcal{G}_\tau^b f(z) - (b-1) \mathcal{G}_\tau^{b+1} f(z),$$

and

$$\mathcal{G}_\tau^b (z f'(z)) = z \left(\mathcal{G}_\tau^b f(z) \right)'. \quad (10)$$

Our aim is to study the operator (7) in view of the geometric function theory, by introducing some conditions on $\Omega_{b,k}(\tau)$. For this purpose we need, the following results.

Theorem 2.2: (Nunokawa [16]) . If $f(z)$ is analytic function in \mathcal{A} , satisfies $|f''(z)| < 1$, ($z \in \mathbb{U}$), then $f(z) \in \mathcal{S}$.

Theorem 2.3: (Mocanu [17]) . If $f(z)$ is analytic function defined by (1) and satisfies

$$|f'(z) - 1| < \frac{\sqrt{20}}{5} \quad (z \in \mathbb{U}), \quad (11)$$

then $f(z)$ belongs to \mathcal{S} .

3. RESULTS

In this section, we concentrate on some results for coefficient of $f(z)$ to be in the class \mathcal{S} and for related classes.

Theorem 3.1: Let $0 \leq \tau < 1$ and $\Re(b) > 1$. If $\mathcal{G}_\tau^b f(z) \in \mathcal{A}$ such that

$$|a_k| \leq \frac{b-1}{k^{2(1+b)}}, \quad k \geq 2.$$

Then $f(z) \in \mathcal{S}$.

Proof: Our aim to apply Theorem 2.2. It is well-known that, when $0 \leq \tau < 1$, the polynomial $L_k^{(b)}(\tau)$ takes its maximality at $\tau = 0$ for all $k \geq 2$ and $\Re(b) > 1$, such that

$$L_k^b(0) = \frac{k^b}{\Gamma(b+1)}.$$

Consequently, we obtain

$$|\Omega_{b,k}(\tau)| \leq k^b, \quad \Re(b) > 1.$$

By the definition of $\mathcal{G}_\tau^b f(z)$, we have the following assertion:

$$\begin{aligned} |[G_\tau^b f(z)]''| &\leq \sum_{k=2}^{\infty} k(k-1)|a_k| |\Omega_{b,k}(\tau)| \\ &\leq \sum_{k=2}^{\infty} k^{2+b} |a_k| \\ &\leq (b-1) \left[1 + \sum_{k=2}^{\infty} \frac{1}{k^b} \right] \\ &:= (b-1) \zeta(b), \quad \Re(b) \rightarrow 1, \end{aligned}$$

where $\zeta(b)$ is denoted the Riemann zeta function $\left(\zeta(\varsigma) = \sum_{k=1}^{\infty} \frac{1}{k^\varsigma} \right)$, (see [18]). But

$$\lim_{b \rightarrow 1} (b-1) \zeta(b) = 1.$$

Thus, $|[G_\tau^b f(z)]''| < 1$, i.e. $\mathcal{G}_\tau^b f(z) \in \mathcal{S}$.

Theorem 3.2: Let $0 \leq \tau < 1$ and $\Re(b) > 1$. If $\mathcal{G}_\tau^b f(z) \in \mathcal{A}$ such that

$$|a_k| \leq \frac{\zeta(k) - 1}{k^{3+b}}, \quad k \geq 2$$

where $\zeta(k) > 1$ is denoted the Riemann zeta function, then $\mathcal{G}_\tau^b f(z) \in \mathcal{S}$.

Proof: Since

$$\begin{aligned} |[G_\tau^b f(z)]''| &\leq \sum_{k=2}^{\infty} k(k-1)|a_k| |\Omega_{b,k}(\tau)| \\ &\leq \sum_{k=2}^{\infty} k^{2+b} |a_k| \\ &\leq \sum_{k=2}^{\infty} \frac{\zeta(k) - 1}{k} = 1 - \delta < 1, \end{aligned}$$

where $\delta = 0.57721 \dots$ is Euler's constant. Hence, this indicates that $G_\tau^b f(z) \in \mathcal{S}$.

Theorem 3.3: Let $0 \leq \tau < 1$ and $\Re(b) > 1$. If $G_\tau^b f(z) \in \mathcal{A}$ such that

$$|a_k| \leq \frac{\zeta(k) - 1}{k^{2+b}}, \quad k \geq 2, \quad \zeta(k) > 1,$$

where $\zeta(k)$ is denoted the Riemann zeta function, then $G_\tau^b f(z) \in \mathcal{S}$. Moreover, $G_\tau^b f(z) \in \mathcal{B}$.

Proof: Since

$$\begin{aligned} |[G_\tau^b f(z)]''| &\leq \sum_{k=2}^{\infty} k(k-1)|a_k| |\Omega_{b,k}(\tau)| \\ &\leq \sum_{k=2}^{\infty} k^{2+b} |a_k| \\ &\leq \sum_{k=2}^{\infty} \zeta(k) - 1 = 1, \end{aligned}$$

Hence, this refers to $G_\tau^b f(z) \in \mathcal{S}$. To prove that $G_\tau^b f(z) \in \mathcal{B}$ it is sufficient to show that $|[G_\tau^b f(z)]'| > 0$.

$$\begin{aligned} |[G_\tau^b f(z)]'| &= 1 + \sum_{k=2}^{\infty} k |a_k| |\Omega_{b,k}(\tau) z^{k-1}| \\ &\geq 1 - \sum_{k=2}^{\infty} k^{1+b} |a_k| \\ &\geq 1 - \sum_{k=2}^{\infty} \frac{\zeta(k) - 1}{k} \\ &= \delta > 0. \end{aligned}$$

This completes the proof.

Theorem 3.4: Let $0 \leq \tau < 1$ and $\Re(b) > 1$. If $G_\tau^b f(z) \in \mathcal{A}$ such that

$$|a_k| \leq \frac{\zeta(2k) - 1}{2^{2k} k^{2+b}}, \quad k \geq 2, \quad \zeta(k) > 1,$$

where $\zeta(2k)$ is refereed the Riemann zeta function, then $\mathcal{G}_\tau^b f(z) \in \mathcal{S}$.

Proof: Since

$$\begin{aligned} |[G_\tau^b f(z)]''| &\leq \sum_{k=2}^{\infty} k(k-1)|a_k| |\Omega_{b,k}(\tau)| \\ &\leq \sum_{k=2}^{\infty} k^{2+b}|a_k| \\ &\leq \sum_{k=2}^{\infty} \frac{\zeta(2k)-1}{2^{2k}} = \frac{1}{6} < 1, \end{aligned}$$

Hence, this refers to $\mathcal{G}_\tau^b f(z) \in \mathcal{S}$.

Theorem 3.5: Let $0 \leq \tau < 1$ and $\Re(b) > 1$. If $\mathcal{G}_\tau^b f(z) \in \mathcal{A}$ such that

$$|a_k| \leq \frac{\zeta(2k-1)-1}{(k-1)k^{1+b}}, \quad k \geq 2, \quad \zeta(k) > 1,$$

where $\zeta(2k)$ is refereed the Riemann zeta function, then $\mathcal{G}_\tau^b f(z) \in \mathcal{S}$.

Proof: Our aim is to apply Theorem 2.3. Since

$$\begin{aligned} \left| \sum_{k=2}^{\infty} k a_k \Omega_{b,k}(\tau) \right| &\leq \sum_{k=2}^{\infty} k |a_k| |\Omega_{b,k}(\tau)| \\ &\leq \sum_{k=2}^{\infty} k^{1+b} |a_k| \\ &\leq \sum_{k=2}^{\infty} \frac{\zeta(2k)-1}{(k-1)}. \end{aligned}$$

Consequently, we obtain

$$|[G_\tau^b f(z)]' - 1| \leq \sum_{k=1}^{\infty} \frac{\zeta(2k)-1}{k} = \log 2 = 0.30102 \dots < \frac{\sqrt{20}}{5} = 0.8944.$$

Thus, $\mathcal{G}_\tau^b f(z) \in \mathcal{S}$.

Next, we illustrate some geometric properties of the operator $\mathcal{G}_\tau^b f(z)$ to be starlike and convex. For this purpose, we recall that the function belongs to $\mathcal{S}^*(\beta)$, $0 < \beta < 1$, if it achieves the inequality (see [19]).

$$\left| \frac{f(z)}{z f'(z)} - \frac{1}{2\beta} \right| < \frac{1}{2\beta}.$$

Moreover, the function f is in the class $\kappa(\beta)$, $0 < \beta < 1$ if and only if $z f' \in \mathcal{S}^*(\beta)$. We have the following results:

Theorem 3.6: Let $\mathcal{G}_\tau^b f(z) \in \mathcal{A}$, $\tau \in (0,1)$ and $\Re(b) > 1$. If $\beta \in \left(0, \frac{1}{2}\right)$ and

$$\sum_{k=2}^{\infty} k^{b+1} |a_k| \leq \sum_{k=2}^{\infty} \frac{1-2\beta}{1+2\beta}$$

Then, $\mathcal{G}_\tau^b f(z) \in \mathcal{S}^*(\beta)$.

Proof: By the assumption of the theorem, we have the following conclusion:

$$\begin{aligned} \left| \frac{[\mathcal{G}_\tau^b f(z)]}{z [\mathcal{G}_\tau^b f(z)]'} - \frac{1}{2\beta} \right| &\leq \left| \frac{[\mathcal{G}_\tau^b f(z)]}{z [\mathcal{G}_\tau^b f(z)]'} \right| \\ &\leq \frac{1 + \sum_{k=2}^{\infty} k^b |a_k|}{1 - \sum_{k=2}^{\infty} k^{b+1} |a_k|} \\ &\leq \frac{1 + \sum_{k=2}^{\infty} k^{b+1} |a_k|}{1 - \sum_{k=2}^{\infty} k^{b+1} |a_k|} \\ &\leq \frac{1}{2\beta}. \end{aligned}$$

This yields that $\mathcal{G}_\tau^b f(z) \in \mathcal{S}^*$, $0 < \beta < 1/2$.

Theorem 3.7: Let $\mathcal{G}_\tau^b f(z) \in \mathcal{A}$, $\tau \in (0,1)$ and $\Re(b) > 1$. If $\beta \in (0, \frac{1}{2})$ and

$$\sum_{k=2}^{\infty} k^{b+2} |a_k| \leq \sum_{k=2}^{\infty} \frac{1-2\beta}{1+2\beta}$$

then $\mathcal{G}_\tau^b f(z) \in \mathcal{K}(\beta)$.

Proof: By the assumption of the theorem, we have the following assertion:

$$\begin{aligned} \left| \frac{z [\mathcal{G}_\tau^b f(z)]}{z (z [\mathcal{G}_\tau^b f(z)]')'} - \frac{1}{2\beta} \right| &\leq \left| \frac{z [\mathcal{G}_\tau^b f(z)]}{z (z [\mathcal{G}_\tau^b f(z)]')'} \right| \\ &\leq \frac{1 + \sum_{k=2}^{\infty} k^{b+1} |a_k|}{1 - \sum_{k=2}^{\infty} k^{b+2} |a_k|} \\ &\leq \frac{1 + \sum_{k=2}^{\infty} k^{b+2} |a_k|}{1 - \sum_{k=2}^{\infty} k^{b+2} |a_k|} \\ &\leq \frac{1}{2\beta} \end{aligned}$$

This implies that $\mathcal{G}_\tau^b f(z) \in \mathcal{K}(\beta)$, $0 < \beta < 1/2$.

Theorem 3.8: Let $\mathcal{G}_\tau^b f(z) \in \mathcal{A}$, $\tau \in (0,1)$ and $\Re(b) > 1$. If $\beta \in (0, \frac{5}{6})$ and

$$|a_k| \leq \frac{1}{k^{b+1}}$$

then $\mathcal{G}_\tau^b f(z) \in \mathcal{S}^*(\beta)$.

Proof: To show that the operator $\mathcal{G}_\tau^b f(z) \in \mathcal{S}^*(\beta)$, we conclude

$$\begin{aligned}
\left| \frac{z [\mathcal{G}_\tau^b f(z)]}{z (z [\mathcal{G}_\tau^b f(z)]')'} - \frac{1}{2\beta} \right| &\leq \frac{1 + \sum_{k=2}^{\infty} k^{b+1} |a_k|}{1 - \sum_{k=2}^{\infty} k^{b+1} |a_k|} \\
&\leq \frac{1 + \sum_{k=2}^{\infty} \frac{1}{k^0}}{1 - \sum_{k=2}^{\infty} \frac{1}{k^0}} \leq \frac{2 + \sum_{k=1}^{\infty} \frac{1}{k^0}}{2 - \sum_{k=1}^{\infty} \frac{1}{k^0}} \\
&\leq \frac{2 + \zeta(0)}{2 - \zeta(0)} = \frac{3/2}{5/2} = \frac{3}{5}, \quad \zeta(0) = -\frac{1}{2} \\
&\leq \frac{1}{2\beta}.
\end{aligned}$$

This yields that $\mathcal{G}_\tau^b f(z) \in \mathcal{S}^*(\beta)$, $0 < \beta < 5/6$.

Theorem 3.9: Let $\mathcal{G}_\tau^b f(z) \in \mathcal{A}$, $\tau \in (0,1)$ and $\Re(b) > 1$. If $\beta \in \left(0, \frac{5}{6}\right)$ and

$$|a_k| \leq \frac{1}{k^{b+2}}$$

Then, $\mathcal{G}_\tau^b f(z) \in \mathcal{K}(\beta)$.

Proof: To prove that the operator $\mathcal{G}_\tau^b f(z) \in \mathcal{K}(\beta)$, we conclude

$$\begin{aligned}
\left| \frac{z [\mathcal{G}_\tau^b f(z)]}{z (z [\mathcal{G}_\tau^b f(z)]')'} - \frac{1}{2\beta} \right| &\leq \frac{1 + \sum_{k=2}^{\infty} k^{b+2} |a_k|}{1 - \sum_{k=2}^{\infty} k^{b+2} |a_k|} \\
&\leq \frac{1 + \sum_{k=2}^{\infty} \frac{1}{k^0}}{1 - \sum_{k=2}^{\infty} \frac{1}{k^0}} \leq \frac{2 + \sum_{k=1}^{\infty} \frac{1}{k^0}}{2 - \sum_{k=1}^{\infty} \frac{1}{k^0}} \\
&\leq \frac{2 + \zeta(0)}{2 - \zeta(0)} = \frac{3/2}{5/2} = \frac{3}{5}, \quad \zeta(0) = -\frac{1}{2} \\
&\leq \frac{1}{2\beta}.
\end{aligned}$$

This gives that $\mathcal{G}_\tau^b f(z) \in \mathcal{K}(\beta)$, $0 < \beta < 5/6$.

Theorem 3.10: Let $\mathcal{G}_\tau^b f(z) \in \mathcal{A}$, $\tau \in (0,1)$ and $\Re(b) > 1$. If $\beta \in \left(0, \frac{12-\pi^2}{2(12+\pi^2)}\right) \approx (0, 0.05)$ and

$$|a_k| \leq \frac{1}{k^{b+3}},$$

Then, $\mathcal{G}_\tau^b f(z) \in \mathcal{S}^*(\beta)$.

Proof: To demonstrate that the operator $\mathcal{G}_\tau^b f(z) \in \mathcal{S}^*(\beta)$, we conclude

$$\begin{aligned} \left| \frac{z [\mathcal{G}_\tau^b f(z)]}{z (z [\mathcal{G}_\tau^b f(z)]')'} - \frac{1}{2\beta} \right| &\leq \frac{1 + \sum_{k=2}^{\infty} k^{b+1} |a_k|}{1 - \sum_{k=2}^{\infty} k^{b+1} |a_k|} \\ &\leq \frac{1 + \sum_{k=2}^{\infty} \frac{1}{k^2}}{1 - \sum_{k=2}^{\infty} \frac{1}{k^2}} \\ &\leq \frac{2 + \sum_{k=1}^{\infty} \frac{1}{k^2}}{2 - \sum_{k=1}^{\infty} \frac{1}{k^2}} \\ &\leq \frac{2 + \zeta(2)}{2 - \zeta(2)}, \quad \zeta(2) = \frac{\pi^2}{6} \\ &\leq \frac{1}{2\beta} \end{aligned}$$

This gives that $\mathcal{G}_\tau^b f(z) \in \mathcal{S}^*(\beta)$, $0 < \beta < 0.05$.

Theorem 3.11: Let $\mathcal{G}_\tau^b f(z) \in \mathcal{A}$, $\tau \in (0,1)$ and $\Re(b) > 1$. If $\beta \in \left(0, \frac{12-\pi^2}{2(12+\pi^2)}\right) \approx (0, 0.05)$ and

$$|a_k| \leq \frac{1}{k^{b+4}},$$

Then, $\mathcal{G}_\tau^b f(z) \in \mathcal{K}(\beta)$.

Proof: To show that the operator $\mathcal{G}_\tau^b f(z) \in \mathcal{K}(\beta)$, we conclude

$$\begin{aligned} \left| \frac{z [\mathcal{G}_\tau^b f(z)]}{z (z [\mathcal{G}_\tau^b f(z)]')'} - \frac{1}{2\beta} \right| &\leq \frac{1 + \sum_{k=2}^{\infty} k^{b+2} |a_k|}{1 - \sum_{k=2}^{\infty} k^{b+2} |a_k|} \\ &\leq \frac{1 + \sum_{k=2}^{\infty} \frac{1}{k^2}}{1 - \sum_{k=2}^{\infty} \frac{1}{k^2}} \\ &\leq \frac{2 + \sum_{k=1}^{\infty} \frac{1}{k^2}}{2 - \sum_{k=1}^{\infty} \frac{1}{k^2}} \\ &\leq \frac{2 + \zeta(2)}{2 - \zeta(2)}, \quad \zeta(2) = \frac{\pi^2}{6} \\ &\leq \frac{1}{2\beta}. \end{aligned}$$

This gives that $\mathcal{G}_\tau^b f(z) \in \mathcal{K}(\beta)$, $0 < \beta < 0.05$.

Theorem 3.12: Let $\mathcal{G}_\tau^b f(z) \in \mathcal{A}$, $\tau \in (0,1)$ and $\Re(b) > 1$. If $\beta \in \left(0, \frac{1}{8}\right)$ and

$$|a_k| \leq \frac{1}{k^{b+4}},$$

Then, $\mathcal{G}_\tau^b f(z) \in \mathcal{S}^*(\beta)$.

Proof: To show that the operator $\mathcal{G}_\tau^b f(z) \in \mathcal{S}^*(\beta)$, we conclude

$$\begin{aligned} \left| \frac{z [\mathcal{G}_\tau^b f(z)]}{z (z [\mathcal{G}_\tau^b f(z)]')'} - \frac{1}{2\beta} \right| &\leq \frac{1 + \sum_{k=2}^{\infty} k^{b+1} |a_k|}{1 - \sum_{k=2}^{\infty} k^{b+1} |a_k|} \\ &\leq \frac{1 + \sum_{k=2}^{\infty} \frac{1}{k^3}}{1 - \sum_{k=2}^{\infty} \frac{1}{k^3}} \\ &\leq \frac{2 + \sum_{k=1}^{\infty} \frac{1}{k^3}}{2 - \sum_{k=1}^{\infty} \frac{1}{k^3}} \\ &\leq \frac{2 + \zeta(3)}{2 - \zeta(3)}, \quad \zeta(3) = 1.2 \\ &\leq \frac{1}{2\beta}. \end{aligned}$$

This gives that $\mathcal{G}_\tau^b f(z) \in \mathcal{S}^*(\beta)$, $0 < \beta < 1/8$.

Theorem 3.13: Let $\mathcal{G}_\tau^b f(z) \in \mathcal{A}$, $\tau \in (0,1)$ and $\Re(b) > 1$. If $\beta \in (0, \frac{1}{8})$ and

$$|a_k| \leq \frac{1}{k^{b+5}},$$

Then, $\mathcal{G}_\tau^b f(z) \in \mathcal{K}(\beta)$.

Proof: To show that the operator $\mathcal{G}_\tau^b f(z) \in \mathcal{S}^*(\beta)$, we conclude

$$\begin{aligned} \left| \frac{z [\mathcal{G}_\tau^b f(z)]}{z (z [\mathcal{G}_\tau^b f(z)]')'} - \frac{1}{2\beta} \right| &\leq \frac{1 + \sum_{k=2}^{\infty} k^{b+2} |a_k|}{1 - \sum_{k=2}^{\infty} k^{b+2} |a_k|} \\ &\leq \frac{1 + \sum_{k=2}^{\infty} \frac{1}{k^3}}{1 - \sum_{k=2}^{\infty} \frac{1}{k^3}} \\ &\leq \frac{2 + \sum_{k=1}^{\infty} \frac{1}{k^3}}{2 - \sum_{k=1}^{\infty} \frac{1}{k^3}} \\ &\leq \frac{2 + \zeta(3)}{2 - \zeta(3)}, \quad \zeta(3) = 1.2 \\ &\leq \frac{1}{2\beta}. \end{aligned}$$

This gives that $\mathcal{G}_\tau^b f(z) \in \mathcal{K}(\beta)$, $0 < \beta < 1/8$.

4. CONCLUSIONS

We defined a new linear operator in terms of the generating function of the *Laguerre* polynomials. The method is concluded by Hadamard product. Based on this operator, we defined new classes of parametric coefficients in the open unit disk. Different studies have been illustrated, involving the geometric properties of these classes. We conclude that the best upper bound of these classes is determined by the Riemann zeta function.

5. REFERENCES

1. Srivastava, H.M., M. Darus & R.M. Ibrahim. Classes of analytic functions with fractional powers defined by means of a certain linear operator. *Integral Transforms and Special Functions* 22: 17-28 (2011).
2. Srivastava, H.M. A new family of the λ -generalized Hurwitz-Lerch zeta functions with applications. *Applied Mathematics & Information Science* 8: 1485-1500 (2014).
3. Ibrahim, R. M. & M. Darus. On operator defined by double Zeta functions. *Tamkang Journal Mathematics* 42: 1-9 (2011).
4. Srivastava, H.M., L.U.O. Minjie & R.K. Raina. A new integral transform and its applications. *Acta Mathematica Scientia* 35: 1386-1400 (2015).
5. Ibrahim, R.W. & J. Sokol. On a new class of analytic function derived by a fractional differential operator. *Acta Mathematica Scientia* 34: 1417-1426 (2014).
6. Hohlov, Y. Convolutional operators preserving univalent functions. *Ukrainian Mathematical Journal* 37(2): 188-192 (1985).
7. Carlson, B.C. & D.B. Shaffer. Starlike and prestarlike hypergeometric functions. *SIAM Journal on Mathematical Analysis* 15(4): 737-745 (1984).
8. Kim, Y.C. & H.M. Srivastava. Fractional integral and other linear operators associated with the Gaussian hypergeometric function. *Complex Variables and Elliptic Equations* 34(3): 293-312 (1997).
9. Dziok, J. & H.M. Srivastava. Classes of analytic functions associated with the generalized hypergeometric function. *Applied Mathematics and Computation* 103(1): 1-13 (1999).
10. Liu, J.L. & H.M. Srivastava. Certain properties of the Dziok-Srivastava operator. *Applied Mathematics and Computation* 159(2): 485-493 (2004).
11. Srivastava, H.M. Some Fox-Wright generalized hypergeometric functions and associated families of convolution operators. *Applicable Analysis and Discrete Mathematics* 1: 56-71 (2007).
12. Kiryakova, V. Criteria for univalence of the Dziok-Srivastava and the Srivastava-Wright operators in the class A. *Applied Mathematics and Computation* 218(3): 883-982 (2011).
13. Srivastava, H.M. & A.A. Attiya. An integral operator associated with the Hurwitz-Lerch Zeta function and differential subordination. *Integral Transforms and Special Functions* 18(3): 207-216 (2007).
14. Ibrahim, R.W. On certain linear operator defined by basic hypergeometric functions. *Matematiski Vesnik* 65(1): 1-7 (2013).
15. Szego, G. *Orthogonal Polynomials*, 4th ed. American Mathematical Society, Providence, R.I., Colloquium Publications, Vol. XXIII. MR 0372517 (1975).
16. Nunokawa, M. On the order of strongly starlikeness of strongly convex functions. *Proceedings of the Japan Academy, Series A, Mathematical Sciences* 69(7): 234-237 (1993).
17. Mocanu, P.T. Some simple criteria for starlikeness and convexity. *Libertas Mathematica* 13: 27-40 (1993).
18. Karatsuba, A.A. Density theorem and the behavior of the argument of the Riemann zeta function. *Mathematical Notes* 60(3): 333-334 (1996).
19. Ochiai, K., S. Owa & M. Acu. Applications of Jack's lemma for certain subclasses of analytic functions. *General Mathematics* 13(2): 73-82 (2005).
20. Dziok, J. & H.M. Srivastava. Certain subclasses of analytic functions associated with the generalized hypergeometric function. *Integral Transforms and Special Functions* 14(1): 7-18 (2003).



Automatic Signature Extraction from Document Images using Hyperspectral Unmixing

Kashif Iqbal, and Khurram Khurshid*

Department of Electrical Engineering, Institute of Space Technology,
Islamabad 44000, Pakistan

Abstract: Signature is one of the most important and widely accepted biometric modality. It is the most common biometric used in documents like financial transactions, legal documents, contracts, etc. Over the years, many signature verification methods have been proposed; however, it is a common notion in most of these methods that signature is available separately for verification purposes. In real world scenarios, signatures are not always available separately particularly in forensics. In documents, signatures usually overlap with other parts of the document, like printed text, lines and graphics, where it becomes practically impossible to detect and localize the signature pixels. In this paper, we present a robust and very effective method for signature segmentation from documents using hyperspectral imaging. A comparative analysis of state of the art *key-point detection based method* and proposed *hyperspectral unmixing method* are provided. The preliminary study shows that spectral unmixing offers great potential for automatic signature extraction from document images.

Keywords: Hyperspectral imaging, document image analysis, hyperspectral unmixing, end-member identification, abundance map, HySime, MVES, MVSA

1. INTRODUCTION

The modern day technologies and security requirements demand user authentication at every step. The user authentication and verification is performed based on different biometrics like fingerprint, iris, voice and handwritten signatures [1]. With the advancements in automated user verification and authentication, many methods for the extraction of information and authentication are presented [2- 4].

The handwritten signature is most accepted and commonly used biometric feature [5]. In forensic science, paper document examination is performed to establish genuineness or non-genuineness, or to expose forgery, or to reveal alterations; additions or deletions in the document. The type of documents that prominently come under question may be a sheet of paper bearing handwriting or mechanically-produced text or signatures such as invoices, a forged cheque or a business contract. There are many methods reported over the years

for verification of signatures on paper documents [2–4, 6, 7].

The majority of signature verification and writer identification methods reported assume that signatures are available pre-segmented (taken out of the document – having no overlap with other document contents like text, lines, stamps or graphics), and these pre-extracted signatures are directly provided to the system. Moreover, the publicly available signature databases also provide pre-segmented handwritten signatures from the documents for verification.

On the other hand, in real world, signatures are usually written on documents like bank cheques, invoices, wills, letters and business contracts, where they overlap with other information present in the document i.e. text, lines, stamps or graphics. In such cases it becomes very difficult to extract signature pixels from these overlapping regions using simple image processing techniques. In order to acquire effective results from state of the art

signature verification methods, it is necessary to segment signatures out of the document [8].

Hyperspectral imagery has found its application in many remote sensing, biomedical and vegetation analysis fields and is now becoming an effective forensic tool for many applications. In this work, a method is presented to segment signatures from paper documents using the hyperspectral document images. Spectral unmixing techniques [9, 10] proposed for remote sensing satellite hyperspectral images are used in this research for the segmentation of signature pixels from the paper documents.

2. SIGNATURE EXTRACTION AND HYPERSPECTRAL UNMIXING METHODS

Signature segmentation using hyperspectral image processing techniques is an emerging field in the area of document analysis. There are many methods reported to extract handwritten text from the printed text based on neural networks, hidden Markov model (HMM), trained Fisher classifier and Markov random fields, etc. [11–15].

The filiformity criteria and hamming measure

have also been reported in the literature for signature extraction [16–18]. A public dataset, namely Tobacco-800, consisting of complex document images containing patch level information for 900 signatures and other related information is available [19]. A Speeded up Robust Feature (SURF) [20] key point detection based technique is presented in the literature for segmentation of signatures from documents in Tobacco-800 dataset [8].

All these techniques, work well in cases where signatures are available pre segmented without any overlap, but if the signature overlaps any other part of the document like lines, text, stamps and graphics, the performance of these techniques drop significantly.

A database of 100 hyperspectral signature documents is reported in [21, 22]. The dataset contains patches of signature documents with different scenarios like partial, none and complete overlap of signatures with text and graphics as illustrated in Fig. 1. SURF [20] key point detection based method is used in this reported paper to segment the signatures from documents. This method uses the spectral property of the

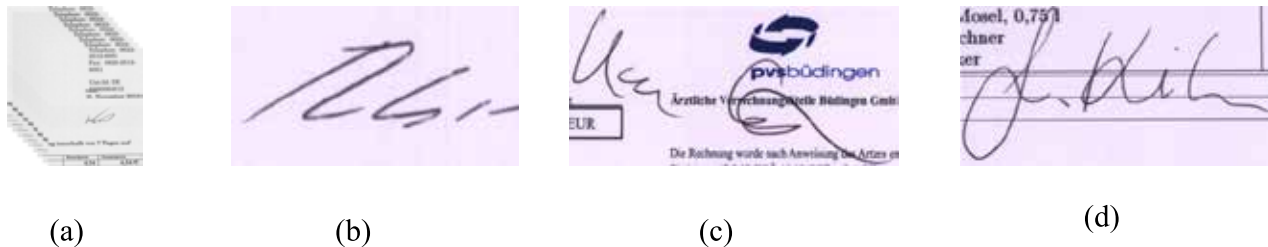


Fig. 1. Signature samples : (a) Sample data-cube; (b) None; (c) Partial; (d) Complete overlap.

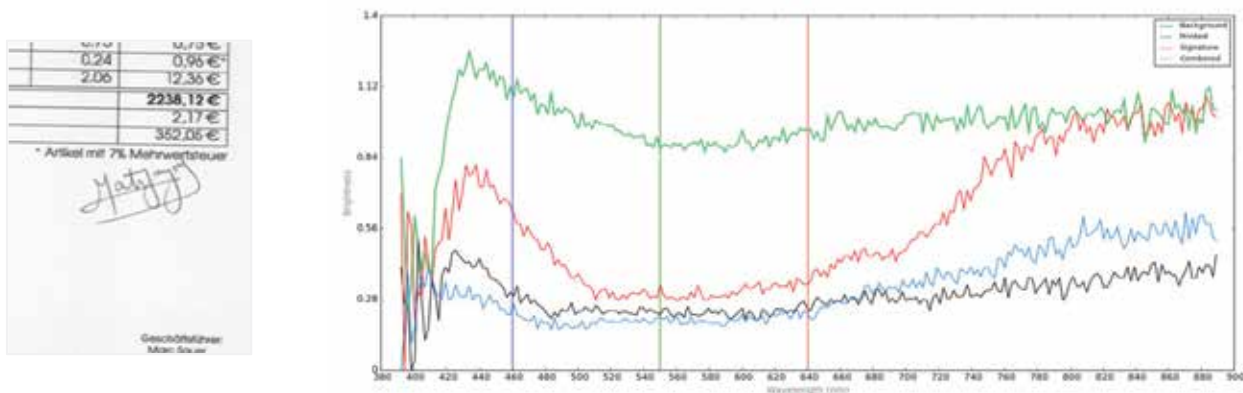


Fig. 2. Signature image band and its spectral signatures.

hyperspectral documents i.e. the signature is present in lower wavelengths and vanishes from the high wavelength bands of the document as shown in Fig 2. The spectral curve in blue is showing the combined spectral behavior of the overlapping region of the document. The reported key point detection based method shows promising results when the signature is not overlapping with other parts of the document i.e. printed text, lines and stamps, but the performance of the key point detection based method decreases in cases where signature is overlapping with other parts. In the field of hyperspectral remote sensing, various hyperspectral unmixing techniques are reported to identify and extract end-members (pure materials) and their respective abundance fractions present in the dataset [23]. The geometrical based spectral unmixing approaches for the linear mixing model like minimum volume enclosing simplex (MVES) [9] and minimum volume simplex analysis (MVSA) [10] are state of the art methods for the solution of hyperspectral unmixing problem. MVES uses a cyclic minimization using linear programs for the solution of minimum volume (MV) problem [24], while MVSA is a robust and enhanced version of MV concept.

In hyperspectral images, if A denotes the end-member signature matrix, $s[n]$ denote the abundance map of n th abundance vector and $w[n]$ denotes noise then linear mixture model can be given by Eq. 1, where $x[n]$ shows the hyperspectral data-cube.

$$x[n] = As[n] + w[n] \quad (1)$$

The hyperspectral signature documents can be considered as a linear mixture of the different materials present in the document i.e. paper, printed text, signature and other graphics.

Therefore, the problem of our signature mixture (overlap) with other parts of the document is treated as a hyperspectral unmixing problem and state of the art spectral unmixing algorithms can be used to segment signature pixels from the documents which are difficult to extract otherwise. The unmixing techniques identify the end-members present in the document, along with their abundances. The MVES and MVSA techniques do not require pure pixels to be present in the dataset. The method

successfully extracts signatures from all kind of documents (none, partial and complete overlap). The methodology is discussed in detail in the next section.

3. METHODOLOGY

3.1 Dataset and Preprocessing

The dataset reported by Malik et al. [21] is used in this work. The dataset contains patches from 100 document images, scanned using hyperspectral camera with a spectral resolution of 2.1 nm. The documents used contain printed text mostly in black but include colored graphics and logos.

Signatures are performed using different type of pens including oil and gel pens, having blue and black inks. The dataset contain document examples of partial, none and complete overlapping signatures. The ground truth reported previously for this dataset was available at signature bounding box level [21].

The bounding box level ground truth serves well in cases where signature is not overlapping with other parts of the document, but in partial or complete overlap of the signatures this ground truth does not give us the true evaluation of the performance of our system. The pixel level ground truth for the complete dataset was generated in this research, which will also be beneficial for any future work on this dataset. The pixel level ground truth is generated by manually marking the overlapping pixels of the signature; the results at different steps of the ground truth generation process are given in Fig. 4.

The drawback of hyperspectral data is that along with huge amount of information it contains noise. In this dataset, it was observed that low wavelength bands near 400 nm contain huge amount of noise (Fig. 3) and it is essential to remove these bands to produce correct results. An automatic noise level detection and estimation technique is used in this work. It uses patch-based noise level estimation algorithm for images to estimate noise level in each band of the document [25].

A threshold based on median value of noise levels is selected to successfully remove the noisy bands from the signature documents. The remaining



Fig. 3. Noisy bands.

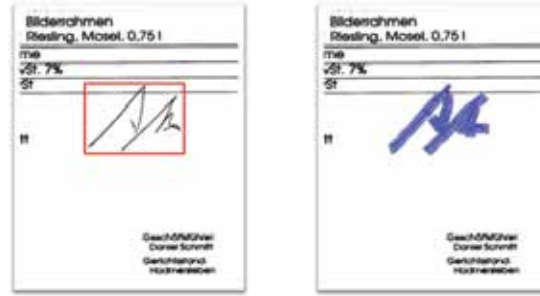


Fig. 4. Pixel level ground truth generation steps.

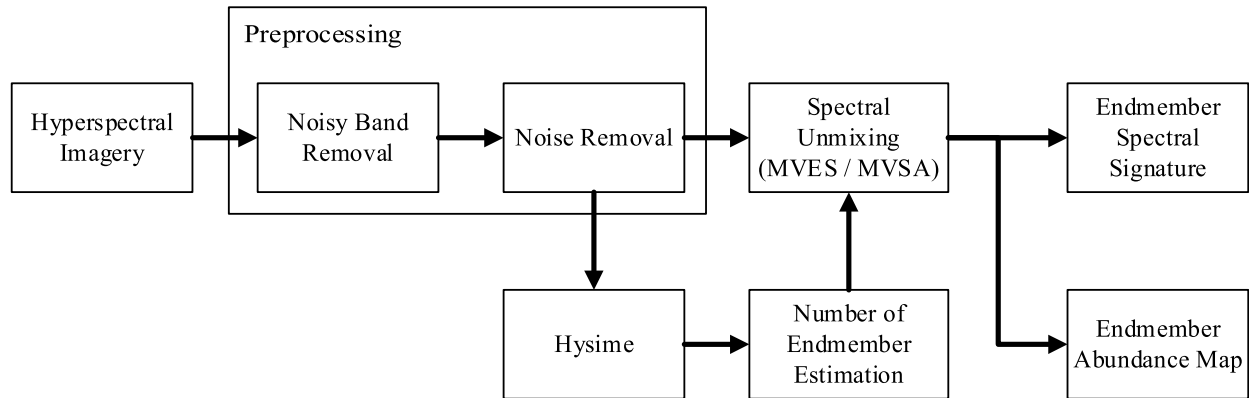


Fig. 5. Flow diagram of Hyperspectral Unmixing method for signature segmentation.

dataset is used to effectively segment signatures from the documents. There is also small noise present in remaining bands hence averaging and median filters are applied to minimize the effect of this noise.

3.2 Hyperspectral Unmixing Methods

The SURF key-point based method reported by Malik et al. [21] was very successful in segmenting signature from documents in which there was no overlap between signature and other parts of the document i.e. text, line and stamps. But with almost all the signatures that were in partial or complete overlap with other parts; the key-point based method reported was not successful to segment the overlap portion of the document (Fig. 6). In real scenarios signatures usually overlap with other parts of the document; so there is a need for signature segmentation techniques that could extract these overlapping pixels in a more effective manner. In this research, spectral unmixing methods are used to segment signatures from documents; i.e., MVES and MVSA. Along with these methods,

two variants are also implemented to improve the signature extraction results. The MVES and MVSA algorithms require an estimate of the number of end-members present in the document to calculate the spectral response of end-members along with their fractional abundances. Hyperspectral signal subspace identification by minimum error (Hysime) [26] is used for the subspace identification and number of end-member estimation. This estimated number of end-members is used by the MVES and MVSA algorithms. The unmixing algorithms provide the spectral signatures and abundance maps of the end-members present in the dataset. The flow diagram of the unmixing methods for hyperspectral document images is given in Fig. 5.

Once the abundance maps of the end-members are generated, we discard those abundance maps which spread throughout the document and select the abundance maps relating to the signatures. The selected abundance map corresponding to the signature is used to generate the segmented signature pixels by applying Sauvola binarization algorithm [27]. The results obtained from MVES

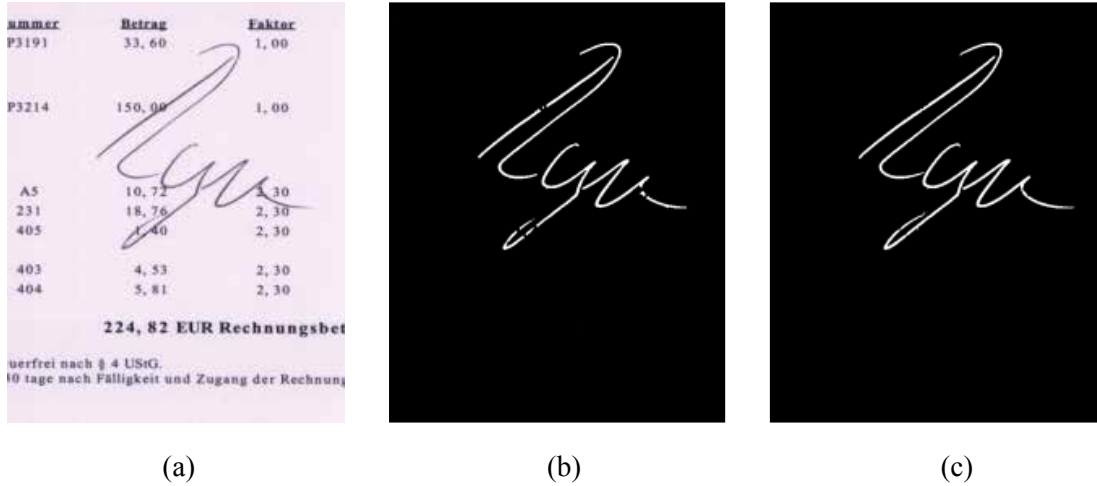


Fig. 6. (a) RGB Image; (b) Key-point Detection Method result; (c) Method 2 result.

and MVSA algorithms are given in Table 1. These results outperform previously proposed key-point detection method [21] especially in cases where signatures are overlapping with other parts of the document. Due to highly mixed nature of the signature and text/lines/stamp pixels in the overlapping regions of the document as depicted in the spectral signatures of the document (Fig. 3), few signature pixels are still missing in the final output. To improve the signature pixel count in the overlapping parts of the signature, it is proposed to combine the signature output of both methods (MVES and MVSA) to get better results. For future reference in this paper the union of MVES and MVSA results is called Method 1 and its results are given in Table 1. Also to further improve the performance of our system and signature pixels that

are still missing in overlapping regions; signatures obtained from Method 1 are skeletonized as shown in Fig. 5 and based on small minimum distance (< 5 pixels) between the edges of skeletonized structure pixel filling is performed. For further reference in this paper this method is called Method 2. The noise removal is performed at each step to remove small noisy objects that does not belong to the signatures. The final results of Method 2 are also given in Table 1.


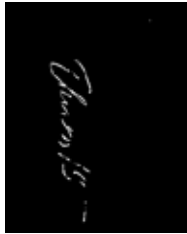



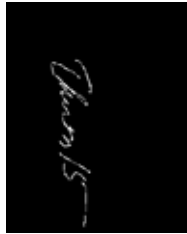

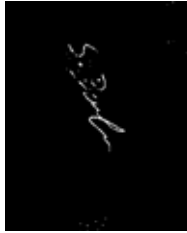





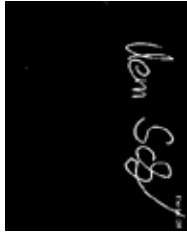










4. RESULTS AND EVALUATION

The results obtained from different methods are given in this section. The results shown in Table 1 clearly depict that the signatures with overlapping parts are segmented more accurately by using



Fig. 7. Skeleton structure for signature.

Table 1. RGB images and final results of different methods.

RGB Image	Key-point Method	MVES	MVSA	Method 1	Method 2
					
					
					
					

spectral unmixing methods.

The bounding box method used by Malik et al. [21] to report the performance of system gave good results for the documents where the signatures had very little or no overlap with other parts of the document and where there was little noise present in the segmented signature bounding box. But when the overlap of signature happens, this evaluation method does not give clear understanding of the missing overlapping pixels. So a pixel level evaluation method is adopted in this study, to get clear understanding of the segmented signature pixels that are overlapping.

The performance of our system is reported by using precision, recall and F measure values.

Precision representing how relevant our retrieved signatures are, i.e. what percentage out of the retrieved signature pixels are corresponding to signatures, and Recall is indicating that out of all signatures pixels which are present in the document how many of them are part of retrieved signature pixels. The F measure is the harmonic mean of precision and recall and it gives an overall performance measure of the system. The precision, recall and F measure for the database of 100 documents is calculated for different methods and is given in Table 2.

Key point detection based method performs with very high precision but the recall is low meaning that there are many signature pixels that

Table 2. Precision and recall complete dataset.

	Precision (%)	Recall (%)	F Measure (%)
Key Point Detection Method	92	80	85.6
MVES	85	86	85.5
MVSA	90	82	85.8
Method 1	81	95	87.5
Method 2	81	95	87.5

Table 3. Precision and recall overlapping signature documents.

	Precision (%)	Recall (%)	F Measure (%)
Key Point Detection Method	76	76	76
MVES	80	81	82
MVSA	83	84	84
Method 1	76	91	83
Method 2	75	92	83

are missed in the final segmented signature. The unmixing algorithms give us good precision but the recall is very high meaning that we are extracting most of original signature pixels. The F measure clearly gives unmixing methods edge over the previously reported methods.

The better performance of unmixing methods gets clearer when we evaluate our system on the basis of documents in which signatures are overlapping with other parts of the document. The results obtained for only the overlapping signature are shown in Table 3. It depicts that result for the key-point detection method has dropped down in comparison to the hyperspectral unmixing methods. The unmixing algorithms have significantly improved the precision and recall of our system in cases where signatures are overlapping. The system is successfully extracting most of the signature pixels as compared to the key point based methods. The F measure is also showing clear superiority of unmixing methods over other methods.

5. CONCLUSIONS

In real world scenario, signatures on documents overlap with other parts of the document like text, lines, stamps and graphics, and it becomes very difficult to segment signature pixels from these documents if signatures are not available pre-segmented. In this work hyperspectral unmixing methods using minimum volume simplex are used

for signature segmentation from document images. The proposed unmixing methods successfully extract signature pixels; which is difficult using other image processing techniques like key point detection. The images captured in visible range of electromagnetic spectra are also not sufficient for overlapping signature extraction. The signature extraction techniques using hyperspectral unmixing will open new dimensions in the field of signature extraction and verification. The proposed signature extraction methods can play a vital role in determination of authenticity of documents. In future work the signature segmentation process can be automated to work as a pre-processor for signature verification systems. It can enhance the handwritten signature analysis capabilities performed by different forensic systems.

6. REFERENCES

1. Boyer, K.W., V. Govindaraju & E.N.K. Ratha. Special issue on recent advances in biometric systems. *IEEE Transactions on Systems, Man, and Cybernetics* 37(5): 1091-1095 (2007).
2. Impedovo, D. & G. Pirlo. Automatic signature verification: The state of the art. *IEEE Transactions on Systems, Man, and Cybernetics, Part C (Applications and Reviews)* 38(5): 609-635 (2008).
3. Salama, M.A. & W. Hussein. Invariant Directional Feature Extraction and Matching Approach for Robust Offline Signature Verification. In: *Proceedings of IEEE International Conference on Image, Vision and Computing*. IEEE, Portsmouth, UK, p. 91-95 (2016).
4. Marušić, T., Ž. Marušić & Ž. Šeremet. Identification

- of authors of documents based on offline signature recognition. In: *Proceedings of 38th International Convention on Information and Communication Technology, Electronics and Microelectronics MIPRO*. IEEE, Opatija, Croatia, p. 1144-1149 (2015).
5. Chambers, J., W. Van, A. Garhwal & M. Kankanhalli. Currency security and forensics: a survey. *Multimedia Tools and Applications* 74(11): 4013-4043 (2015).
 6. Malik, M.I., M. Liwicki & A. Dengel. Part-based Automatic System in Comparison to Human Experts. In: *Proceedings of 12th IAPR International Conference on Document Analysis and Recognition*. IEEE, Washington DC, USA, p. 872-876 (2013).
 7. Jain, A.K., F.D. Griess & S.D. Connell. On-line signature verification. *Pattern Recognition* 35(no. 12): 2963-2972 (2002).
 8. Ahmed, S., M.I. Malik, M. Liwicki & A. Dengel. Signature Segmentation from Document Images. In: *Proceedings of International Conference on Frontiers in Handwriting Recognition*. IEEE, Bari, Italy, p. 425-429 (2012).
 9. Chan, T.H., C.Y. Chi, Y.M. Huang & W.K. Ma. A convex analysis-based minimum-volume enclosing simplex algorithm for hyperspectral unmixing. *IEEE Transactions on Signal Processing* 57: 4418-4432 (2009).
 10. Li, J., A. Agathos, D. Zaharie, J.M.B. Dias, A. Plaza & X. Li. Minimum Volume Simplex Analysis: A Fast Algorithm for Linear Hyperspectral Unmixing. *IEEE Transactions on Geoscience and Remote Sensing* 53(9): 5067-5082 (2015).
 11. Guo, J.K. & M.Y. Ma. Separating handwritten material from machine printed text using hidden Markov models. In: *Proceedings of IAPR International Conference on Document Analysis and Recognition*. IEEE, Washington DC, USA, p. 439-443 (2001).
 12. Imade, S., S. Tatsuta & T. Wada. Segmentation and classification for mixed text/image documents using neural network. In: *Proceedings of IAPR International Conference on Document Analysis and Recognition*. IEEE, Tsukuba Science City, Japan, p. 930-934 (1993).
 13. Zheng, Y., H. Li & D. Doermann. Machine printed text and handwriting identification in noisy document images. *IEEE Transactions on Pattern Analysis and Machine Intelligence* 26(3): 337-353 (2004).
 14. Chanda, S., K. Franke & U. Pal. Structural handwritten and machine print classification for sparse content and arbitrary oriented document fragments. In: *Proceedings of the 2010 ACM Symposium on Applied Computing*. ACM, Sierre, Switzerland, p. 18-22 (2010).
 15. Kuhnke, K., L. Simoncini & Z.M. Kovacs-V. A system for machine-written and hand-written character distinction. In: *Proceedings of IAPR International Conference on Document Analysis and Recognition*. IEEE, Montreal, Canada, p. 811-814 (1995).
 16. Djeziri, S., F. Nouboud & R. Plamondon. Extraction of signatures from check background based on a filiformity criterion. *IEEE Transactions on Image Processing* 7(10): 1425-1438 (1998).
 17. Madasu, V.K., M. Hafizuddin, M. Yusof, M. Hanm & K. Kubik, "Automatic extraction of signatures from bank cheques and other documents. In: *Proceedings of Digital Image Computing: Techniques and Applications*. Sun, C., H. Talbot, S. Ourselin & T. Adriaansen (Ed.), IAPR, Sydney, Australia, p. 591-600 (2003).
 18. Sankari, M., M. Benazir & R. Bremananth. Verification of bank cheque images using Hamming measures. In: *Proceedings of 11th International Conference on Control Automation Robotics & Vision*. IEEE, Singapore, p. 2531-2536, (2010).
 19. Lewis, D., G. Agam, S. Argamon, O. Frieder, D. Grossman & J. Heard. Building a Test Collection for Complex Document Information Processing. In: *Proceedings of 29th Annual International ACM SIGIR Conference on Research and development in Information Retrieval*. ACM, Washington, USA, p. 665-666 (2006).
 20. Bay, H., T. Tuytelaars & L. Gool. SURF: Speeded Up Robust Features. *Computer Vision and Image Understanding* 110(3): 346-359 (2008).
 21. Malik, M.I., S. Ahmed, F. Shafait, A.S. Mian, C. Nansen, A. Dengel & M. Liwicki. Hyper-spectral Analysis for Automatic Signature Extraction. In: *Proceedings of 17th Biennial Conference of the International Graphonomics Society*. Remi, C., L. Prevost, & E. Anquetil (Ed.). HAL, Pointe-a-Pitre, Guadeloupe, p. 1-4 (2015).
 22. Abbas, A., K. Khurshid & F. Shafait, Towards Automated Ink Mismatch Detection in Hyperspectral Document Images. In: *Proceedings of 14th IAPR International Conference on Document Analysis and Retrieval*. IAPR, Kyoto, Japan (2017).
 23. Bioucas-Dias, J., A. Plaza, N. Dobigeon, M. Parente, Q. Du, P. Gader & J. Chanussot. Hyperspectral unmixing overview: Geometrical/statistical, and sparse regression-based approaches. *IEEE Journal of Selected Topics in Applied Earth Observations and Remote Sensing* 5(2): 354-379 (2012).
 24. Craig, M.D. Minimum-volume transforms for remotely sensed data. *IEEE Transactions on Geoscience and Remote Sensing* 32(3): 542-552 (1994).
 25. Liu, X., M. Tanaka & M. Okutomi. Single-Image Noise Level Estimation for Blind Denoising. *IEEE Transactions on Image Processing* 22 (12): 5226-5237 (2013).
 26. Bioucas-Dias J.M. & J.M. P. Nascimento. Hyperspectral Subspace Identification. *IEEE Transactions on Geoscience and Remote Sensing* 46(8): 2435-2445 (2008).
 27. Khurshid, K., I. Siddiqi, C. Faure & N. Vincent. Comparison of Niblack inspired Binarization methods for ancient documents. *Document Recognition and Retrieval XVI* 7247: doi: 10.1117/12.805827 (2009).



Numerical Simulation of Fractional Order Dengue Disease with Incubation Period of Virus

Zain Ul Abadin Zafar^{*1,3}, M. Mushtaq¹, Kashif Rehan², and M. Rafiq⁴

¹Department of Mathematics, University of Engineering and Technology, Lahore, Pakistan

²Department of Mathematics, University of Engineering and Technology, KSK Campus, Lahore, Pakistan

³Faculty of Information Technology, University of Central Punjab, Lahore, Pakistan

⁴Faculty of Engineering, University of Central Punjab, Lahore, Pakistan

Abstract: Nowadays, numerical models have great importance in epidemiology. These helps us to understand the transmission dynamics of infectious diseases in a very comprehensive manner. In disease epidemiology, vector-host models are important because many diseases are spreading through vectors. Mosquitoes are vectors of dengue disease as these spread the disease in a population. The infectious vectors infect the hosts while infectious hosts infect to vectors. Two main groups of dengue patients are septic and contagious. The susceptible mosquitoes can get dengue infection from infectious humans but not from infected ones. Humans can be categorized into Susceptible, infected, infectious and recovered ones while mosquitoes are susceptible, infected and infectious. Susceptible individual can transfer dengue infection from diseased mosquitoes only. The transmission dynamics of “Fractional order dengue fever” with incubation period of virus has been analyzed in this paper. Using standard methods for analyzing a system, the stability of equilibrium points of the model has been determined. Finally, numerical simulation has been performed for the same problem for different values of discretization parameter ‘h’.

Keywords: Dengue virus, incubation period, stability, fraction order numerical modeling

1. INTRODUCTION

Recently, diseases caused by dengue virus have become a major health problem in the world [1]. Most probably these diseases are found in tropical areas and also found in some sub-tropical areas [2]. These diseases are found in the following countries America, Africa, Western Pacific, South Asia and Eastern Mediterranean. Before 1970 there were only nine countries which were affected by the dengue disease but after 1995 it increased four times. Until 2001 there were 609,000 patients affected by this disease. This number of patients is double to the figure as in 1995. Now major population of the world is at risk due to this disease. World Health Organization estimated that 49 M (Million) patients can be affected each year by this disease. The attack rate of this disease is 40-50% that can reach up to 80%-90% very soon. The dengue disease can be classified into three different types which are dengue hemorrhagic fever, dengue shock syndrome and dengue fever. These types have different symptoms. Dengue Fever symptoms are less in appearance in case of children's while these appear in case of young and grown up children. Dengue hemorrhagic fever is one of the complex diseases which can turn into fatal condition. This type of disease occurs to the patient when a patient is prone to the dengue virus more than once. Dengue shock syndrome (DSS) is a severe type of which can lead the patient to the hospitalization.

1.1 Causes

It can be caused by DEN1 – 4 virus.

1.2 Transmission

The main cause of dengue disease is *Aedes* mosquito. After biting the infected human, it becomes infected with this disease and then that disease will be transmitted to other human beings. There are two types of *Aedes* mosquitoes which cause this disease. These types are: *Aedes aegypti* and *Aedes albopictus*. When the mosquito *Aedes aegypti* recruits with a dengue infectious person, the dengue virus enters the blood and circulate in the blood (viremia) that carry on for roughly four to seven days [3, 4]. Dengue cannot be transmitted directly from one person to another person. It needs a mosquito as transmitter from one person to another. Mosquitoes are only infected by this disease by biting an infected person. Virus replicates within the mosquito during the incubation period of 8-12 days. After this, glands of mosquito become infected and then virus of this disease will be transmitted to other person after biting that person. Then virus replicates in this newly infected person during the incubation period [5].

1.3 Symptoms

Its symptoms are 4 to 7 days fever after a person has been attacked by mosquito infected with virus. Symptoms are retro-orbital pain nausea, severe headache, joint and muscle pain, rashes, vomiting & high fever. DHF includes all symptoms of dengue fever with some additional symptoms which are bleeding from the nose, gums, or under the skin. It is severe form of dengue which can lead to death.

2. MODEL FORMATION

2.1 Assumptions

- The number of human and mosquito remains same.
- DEN virus effete gets permanent protection from the particular virus but becomes sensitive for others.
- Death and birth rate of human and mosquito goes on side by side.

Variables for model are that represents some special notions are as follow:

$\bar{S}_h(t)$ represents the susceptible individuals with in time t , $\bar{X}_h(t)$ denotes the Infected individuals with in time t , $\bar{I}_h(t)$ gives the number of Infectious individuals with in time t and $\bar{R}_h(t)$ are Recovered individuals with in time t . Beside these $\bar{S}_v(t)$ are the Susceptible mosquitoes (vectors) with in time t , $\bar{X}_v(t)$ tells the Infected mosquitoes (vectors) with in time t , and $\bar{I}_v(t)$ gives the number of Infectious mosquitoes with in time t .

2.2 Mathematical Model

The transmission of dengue virus is shown by following flow chart [6].

The following equations describe transmission dynamics of Dengue infection in human and vector populations:

$$\left. \begin{aligned} \frac{d\bar{S}_h}{dt} &= \lambda N_T - \beta_h \bar{S}_h \bar{I}_v - \mu_h \bar{S}_h \\ \frac{d\bar{X}_h}{dt} &= \beta_h \bar{S}_h \bar{I}_v - \alpha_h \bar{X}_h - \mu_h \bar{X}_h \\ \frac{d\bar{I}_h}{dt} &= \alpha_h \bar{X}_h - r \bar{I}_h - \mu_h \bar{I}_h \\ \frac{d\bar{R}_h}{dt} &= r \bar{I}_h - \mu_h \bar{R}_h \\ \frac{d\bar{S}_v}{dt} &= C - \beta_v \bar{I}_h \bar{S}_v - \mu_v \bar{S}_v \\ \frac{d\bar{X}_v}{dt} &= \beta_v \bar{I}_h \bar{S}_v - \alpha_v \bar{X}_v - \mu_v \bar{X}_v \\ \frac{d\bar{I}_v}{dt} &= \alpha_v \bar{X}_v - \mu_v \bar{I}_v \end{aligned} \right\} \quad (1)$$

with $N_T = \bar{S}_h + \bar{X}_h + \bar{I}_h + \bar{R}_h$

and $N_v = \bar{S}_v + \bar{X}_v + \bar{I}_v$

where

N_T and N_v are constant. So,

$$\frac{dN_T}{dt} = 0 \text{ and } \frac{dN_v}{dt} = 0$$

which implies that $\lambda = \mu_h$

Now for vector population

$$\begin{aligned} \frac{dN_v}{dt} &= \frac{d}{dt} (\bar{S}_v + \bar{X}_v + \bar{I}_v) \\ 0 &= \frac{d}{dt} \bar{S}_v + \frac{d}{dt} \bar{X}_v + \frac{d}{dt} \bar{I}_v \\ 0 &= C - \mu_v \bar{S}_v - \mu_v \bar{X}_v - \mu_v \bar{I}_v \\ 0 &= C - \mu_v (\bar{S}_v + \bar{X}_v + \bar{I}_v) \\ 0 &= C - \mu_v N_v \Rightarrow N_v = \frac{C}{\mu_v} \end{aligned}$$

For normalization of system (1), we let

$$\begin{aligned} S &= \frac{\bar{S}_h}{N_T}, X = \frac{\bar{X}_h}{N_T}, I = \frac{\bar{I}_h}{N_T}, R = \frac{\bar{R}_h}{N_T} \\ S_v &= \frac{\bar{S}_v}{N_T}, X_v = \frac{\bar{X}_v}{N_T}, I_v = \frac{\bar{I}_v}{N_T} \end{aligned}$$

The system of differential equation for transmission dynamics of dengue fever in normalized form is

$$\left. \begin{aligned} \frac{ds}{dt} &= \mu_h - \beta_h S I_v (C/\mu_v) - \mu_h S \\ \frac{dX}{dt} &= \beta_h S I_v (C/\mu_v) - \alpha_h X - \mu_h X \\ \frac{dI}{dt} &= \alpha_h X - r I - \mu_h I \\ \frac{dX_v}{dt} &= \beta_v I N_T (1 - X_v - I_v) - \alpha_v X_v - \mu_v X_v \\ \frac{dI_v}{dt} &= \alpha_v X_v - \mu_v I_v \end{aligned} \right\} \quad (2)$$

subject to the conditions:

$$S + X + I + R = 1 \quad \text{and} \quad S_v + X_v + I_v = 1$$

The terminology used for the different parameters are given Table 1.

Table 1. Different symbols and terminology.

Symbol	Terminology
N_T	Total population of human
β_h	Infectious rate of dengue virus from mosquitoes (vector) to human population
λ	Human population's birth rate
β_v	Infectious rate of dengue virus from human to mosquito (vector) population
α_h	Rate of changing the infected human population to infectious human population
R	Human population's recovery rate
μ_h	Human population death rate
α_v	Vector (mosquito) population death rate
C	Vector (mosquito) population constant recruitment rate

3. BEGINNINGS AND CYPHERS

In this segment, some simple explanations and chattels of the fractional calculus theory and Non-standard discretization are discussed.

3.1. Fundamentals of Fractional-order

Fractional calculus represents a generalization of the ordinary differentiation and integration to non-integer and complex order [22]. The generalization of differential calculus to non-integer orders of derivatives can be traced back to Leibnitz [24]. The main reason for using integer order models was the absence of solution methods for fractional differential equations. It is an emerging field in the area of applied mathematics and mathematical physics such as chemistry, biology, economics, image and signal processing and it has many applications in many areas of science and engineering [23] for example, viscoelasticity, control theory, heat conduction, electricity, chaos and fractals etc. [22]. Various applications, like in the reaction kinetics of proteins, the anomalous electron transport in amorphous materials, the dielectrical or mechanical relation of polymers, the modeling of glass forming liquids and others are successfully performed in numerous papers [24].

The physical and geometrical meaning of the non-integer integral containing the real and complex conjugate power-law exponent has been proposed. Finding examples of real systems describes by the fractional derivative is an open issue in the area of fractional calculus [22].

Since integer order differential equations cannot precisely describe the experimental and field measurement data, as an alternative approach non-integer order differential equation models are now being widely applied [19, 20]. The advantage of fractional-order differential equation systems over ordinary differential equation systems is that they allow greater degrees of freedom and incorporate memory effect in the model. In other words, it provides an excellent tool for the description of memory and hereditary properties which were not taken into account in the classical integer order model [21].

The calculus of variations is widely applied for some disciplines like engineering, pure and applied mathematics. Moreover, the researchers have recently proved that the physical systems with dissipation can be clearly modeled more accurately by using fractional representations [23]. Recently, most of the dynamical systems based on the integer-order calculus have been modified into the fractional order domain due to the extra degrees of freedom and the flexibility which can be used to precisely fit the experimental data much better than the integer order modeling. Few of the nonlinear models are given in [28-30].

There are many definitions of fractional derivatives. Few of them are:

(1) Caputo's definition [25]

$$\mathfrak{D}_u^\phi(g(u)) = \frac{1}{\Gamma(n-\phi)} \int_0^u (u-s)^{n-\phi-1} \frac{d^n g(s)}{ds^n} ds$$

(2) Riemann-Liouville definition [25]

$$\mathfrak{D}_u^\phi(g(u)) = \frac{1}{\Gamma(n-\phi)} \frac{d^n}{du^n} \int_0^u (u-s)^{n-\phi-1} g(s) ds$$

(3) Jumarie's definition [25]

$$\mathfrak{D}_u^\phi(g(u)) = \frac{1}{\Gamma(n-\phi)} \frac{d^n}{du^n} \int_0^u (u-s)^{n-\phi-1} [g(s) - g(0)] ds$$

(4) Xiao-Jun Yang's definition [25]

$$\mathfrak{D}_u^\phi(g(u_0)) = g^\phi(u_0) = \frac{d^\phi}{du^\phi} g(u) \Big|_{u=u_0} = \lim_{u \rightarrow u_0} \frac{\Delta^\phi(g(u) - g(u_0))}{(u-u_0)^\phi}$$

where $\Delta^\phi(g(u) - g(u_0)) \cong \Gamma(1+\phi)\Delta(g(u) - g(u_0))$.

(5) Chen's fractal derivative [25]

$$\frac{dg}{du^\phi} = \lim_{s \rightarrow u} \frac{g(u) - g(s)}{u^\phi - s^\phi}$$

(6) Ji-Huan He's fractal derivative [25]

$$\frac{\mathfrak{D}g}{\mathfrak{D}u^\phi} = \Gamma(1+\phi) \lim_{\Delta u = u_1 - u_2 \rightarrow L} \frac{g(u_1) - g(u_2)}{(u_1 - u_2)^\phi}$$

where Δu does not tend to zero, it can be the thickness (L) of a porous medium. Applications of the fractal derivative to fractal media have attracted much attention, for example it can model heat transfer and water permeation in multi-scale of fabrics and wool fibers.

(7) Davidson-Essex derivative [26]

$$\mathfrak{D}_0^\phi(g(u)) = \frac{1}{\Gamma(1-\phi)} \frac{d^{n+1-k}}{du^{n+1-k}} \int_0^u (u-s)^{-\phi} \frac{d^k g(s)}{ds^k} ds$$

(8) Coimbra derivative [26]

$$\mathfrak{D}_0^{\phi(u)}(g(u)) = \frac{1}{\Gamma(1-\phi(u))} \left\{ \int_0^u (u-s)^{-\phi(s)} \frac{dg(s)}{ds} ds + g(0)u^{-\phi(u)} \right\}$$

(9) Canavati derivative [26]

$${}_a \mathfrak{D}_u^\xi(g(u)) = \frac{1}{\Gamma(1-\phi)} \frac{d}{du} \int_0^u (u-s)^\phi \frac{d^n g(s)}{ds^n} ds$$

$$n = |\xi|, \phi = n - \xi$$

(10) Osler fractional derivative [26]

$${}_a \mathfrak{D}_u^\xi(g(u)) = \frac{\Gamma(1+\phi)}{2\pi i} \int_{\mathfrak{S}(a, u^+)} \frac{g(s)}{(s-u)^{1+\phi}} ds$$

(11) k-fractional Hilfer derivative [26]

$${}_k \mathfrak{D}^{\phi, \xi}(g(u)) = I_k^{\xi(1-\phi)} \frac{d}{du} I_k^{(1-\xi)(1-\phi)} g(u)$$

where $I_k^\phi g(u)$ is the k-fractional Hilfer integral

$$I_k^\phi g(u) = \frac{1}{k \Gamma_k(\phi)} \int_0^u (u-s)^{\frac{\phi}{k}-1} g(u) du$$

(12) Caputo Fabrizio derivative [27]

Let $g \in H^1(a, b)$, $a < b$, $\phi \in [0, 1]$ then, the new Caputo fractional derivative is

$$\mathfrak{D}_u^\phi(g(u)) = \frac{M(\phi)}{1-\phi} \int_a^u g'(u) \exp\left(-\phi \frac{u-s}{1-\phi}\right) ds \quad (*)$$

where $M(\phi)$ denotes a normalization function obeying $M(0) = M(1) = 1$. However, if the function does not belong to $H^1(a, b)$ then, the derivative has the form

$$\mathfrak{D}_u^\phi(g(u)) = \frac{\phi M(\phi)}{1-\phi} \int_a^u [g(u) - g(s)] \exp\left(-\phi \frac{u-s}{1-\phi}\right) ds \quad (**)$$

If $\sigma = \frac{1-\phi}{\phi} \in [0, \infty]$, $\phi = \frac{1}{1+\sigma} \in [0, 1]$, then eq. (**) assumes the form

$$\mathfrak{D}_u^\sigma(g(u)) = \frac{N(\sigma)}{\sigma} \int_a^u g'(u) \exp\left(-\frac{u-s}{\sigma}\right) ds, \quad N(0) = N(\infty) = 1$$

(13) Atangana Baleanu Fractional Derivative in Riemann-Liouville sense [28]

Let $g \in H^1(a, b)$, $a < b$, $\phi \in [0, 1]$ and not necessary differentiable then, the definition of the new fractional derivative is given as

$${}^{ABR}_a \mathfrak{D}_u^\phi(g(u)) = \frac{B(\phi)}{1-\phi} \frac{d}{du} \int_a^u g(s) E_\phi\left(-\phi \frac{(u-s)^\phi}{1-\phi}\right) ds$$

(14) Atangana Baleanu Fractional Derivative in Riemann-Caputo sense [28]

Let $g \in H^1(a, b)$, $a < b$, $\phi \in [0, 1]$ and not necessary differentiable then, the definition of the new fractional derivative is given as

$${}^{ABC}_a \mathfrak{D}_u^\phi(g(u)) = \frac{B(\phi)}{1-\phi} \int_a^u g'(s) E_\phi\left(-\phi \frac{(u-s)^\phi}{1-\phi}\right) ds$$

3.2. Grunwald-Letnikov (GL) Method

The GL method of approximation for the 1-D fractional derivative is as follows [11].

$$D^\beta x(\tau) = g(\tau, x(\tau)), \quad x(0) = x_0, \quad \tau \in [0, \tau_f], \quad (3)$$

$$D^\beta x(\tau) = \lim_{h \rightarrow 0} h^{-\beta} \sum_{j=0}^{\lceil \frac{\tau_f}{h} \rceil} (-1)^j \binom{\beta}{j} x(\tau - ih),$$

where $0 < \beta < 1$, D^β signifies the fractional derivative, h is the step size and $\lceil \frac{\tau_f}{h} \rceil$ represents the integer part of $\frac{\tau_f}{h}$. Therefore, Eq. (3) is discretized in the next form,

$$\sum_{i=0}^n C_j^\beta x_{n-j} = f(\tau_n, x_n), \quad n = 1, 2, 3, \dots$$

where $\tau_n = nh$ and C_j^β are the GL coefficients defined as

$$C_i^\beta = \left(1 - \frac{1+\beta}{i}\right) C_{i-1}^\beta, \quad C_0^\beta = h^{-\beta}, \quad i = 1, 2, 3, \dots$$

The paper of Mickens [13] provides an all-purpose route for determining $\phi(h)$ for the ODEs. A specimen of the NSFD discretization procedure is its application to the decay equation

$$x' = -\lambda x$$

where λ is constant. The discretization scheme [13] is

$$\frac{x_{n+1} - x_n}{\phi} = -\lambda x_n, \quad \phi(h, \lambda) = \frac{1 - e^{-\lambda h}}{\lambda}$$

An alternate example is given by

$$x' = \lambda_1 x - \lambda_2 x^2$$

where the NSFD scheme is

$$\frac{x_{n+1} - x_n}{\phi} = \lambda_1 x_n - \lambda_2 x_n x_{n+1}$$

$$\phi(h, \lambda_1) = \frac{e^{\lambda_1 h} - 1}{\lambda_1}$$

It should be renowned that the NSFD schemes for both ODEs are exact in the sense that $x_n = x(t_n)$ for all applicable values of $h > 0$.

4. FRACTIONAL ORDER DENGUE MODEL

Mathematical models have been used extensively in research into the epidemiology of dengue to help improve our understanding of the major contributing factors in a given epidemic. Main claim is that fractional model can give more realistic interpretation of natural phenomena. The use of fractional derivative allows us to model memory effects, and results in a more powerful approach to epidemiology models. A few papers have been written on fractional order dengue epidemiology [16, 17, 18]. So the system (2) in fractional order form is:

$$\left. \begin{aligned} \frac{d^{\gamma_1} S}{dt^{\gamma_1}} &= \mu_h - \beta_h S I_v (C/\mu_v) - \mu_h S \\ \frac{d^{\gamma_2} X}{dt^{\gamma_2}} &= \beta_h S I_v (C/\mu_v) - \alpha_h X - \mu_h X \\ \frac{d^{\gamma_3} I}{dt^{\gamma_3}} &= \alpha_h X - rI - \mu_h I \\ \frac{d^{\gamma_4} X_v}{dt^{\gamma_4}} &= \beta_v I N_T (1 - X_v - I_v) - \alpha_v X_v - \mu_v X_v \\ \frac{d^{\gamma_5} I_v}{dt^{\gamma_5}} &= \alpha_v X_v - \mu_v I_v \end{aligned} \right\} \quad (4)$$

with the initial conditions

$$S(0) = 0.1, \quad X(0) = 0, \quad I(0) = 0, \quad X_v(0) = 0.1, \quad I_v(0) = 0.1$$

In order to analyze the model's stability, the theorem of stability on fractional order systems and fractional Ruth-Hurwitz stability conditions for fractional order differential equations are presented. The first theorem of stability has been given for fractional order systems.

4.1. Stability Analysis

Theorem 1. [14] Consider the fractional order system given below

$$D^\alpha U(t) = G(U), U(0) = U_0 \quad (5)$$

where $0 < \alpha \leq 1$ and $u \in R^n$. Equilibrium points of system (5) should be determined by cracking the $G(U) = 0$. These points will be non-globally asymptotically steady if all eigenvalues η matrix of the Jacobian $J = \frac{\partial G}{\partial U}$ evaluated at the equilibrium point mollify:

$$|\arg(\zeta)| > \frac{\alpha \pi}{2}$$

The Jacobian matrix J of system (4) with the equilibrium point $E = (s^*, x^*, i^*, x_v^*, i_v^*)$.

$$J(F^*) = \begin{bmatrix} L_1 & 0 & 0 & 0 & -L_4 \\ L_2 & L_3 & 0 & 0 & L_4 \\ 0 & \alpha_h & L_5 & 0 & 0 \\ 0 & 0 & L_6 & L_7 & L_8 \\ 0 & 0 & 0 & \alpha_v & -\mu_v \end{bmatrix} \quad (6)$$

$$L_1 = -\frac{\beta_h i_v^* C}{\mu_v} - \mu_h, L_2 = \frac{\beta_h i_v^* C}{\mu_v}, L_3 = -\mu_h - \alpha_h, L_4 = \frac{\beta_h S^* C}{\mu_v}, L_5 = -\mu_h - r, \\ L_6 = \beta_v N_T (1 - x_v^* - i_v^*), L_7 = -\alpha_v - \mu_v - \beta_v i^* N_T, L_8 = -\beta_v i^* N_T$$

4.2. Equilibrium Points

To find the equilibrium state points we set the right hand side of all equations in system (4) equated to zero. We found that the system has two possible equilibrium points i.e. the disease free equilibrium (DFE) and endemic equilibrium (EE).

Disease free equilibrium (DFE):

$$V_0 = (1, 0, 0, 0, 0)$$

Endemic equilibrium (EE):

$$V_1 = (S^*, X^*, I^*, X_v^*, I_v^*)$$

where

$$S^* = \frac{(\alpha_v + \mu_v)(WH\mu_h^2\mu_v + \alpha_h\gamma_v\mu_h)}{\alpha_h\gamma_v[\mu_h(\alpha_v + \mu_v) + \alpha_v\gamma_h]} \\ X^* = \frac{W\mu_h^2\mu_v(\alpha_v + \mu_v)(E_0 - 1)}{\alpha_h\alpha_h[\mu_h(\alpha_v + \mu_v) + \alpha_v\gamma_h]} \\ I^* = \frac{\mu_h\mu_v(\alpha_v + \mu_v)(E_0 - 1)}{\alpha_h[\mu_h(\alpha_v + \mu_v) + \alpha_v\gamma_h]} \\ X_v^* = \frac{\mu_v(WH\mu_h^3\mu_v)(E_0 - 1)}{\gamma_h\alpha_v(\alpha_h\gamma_v\mu_h + WH\mu_h^2\mu_v)} \\ I_v^* = \frac{WH\mu_h^3\mu_v}{\gamma_h(\alpha_h\gamma_v\mu_h + WH\mu_h^2\mu_v)}(E_0 - 1)$$

where

$$E_0 = \frac{\alpha_h\alpha_v\gamma_h\gamma_v}{\mu_v(r + \mu_h)(\alpha_h + \mu_h)(\alpha_v + \mu_v)} \\ \gamma_h = \frac{c\beta_h}{\mu_v}, \gamma_v = N_T\beta_v, W = \frac{r + \mu_h}{\mu_h}, H = \frac{\alpha_h + \mu_h}{\mu_h}$$

To see the non-global stability for each equilibrium phase can be determined by the insignia of all eigenvalues. If all eigenvalues have negative real part, then that equilibrium phase is non-global stability. We locate the eigenvalues for each equilibrium phase by setting

$$\det(J - \zeta I) = 0 \quad (7)$$

where J is the Jacobian matrix of the right hand side of (4) determined at the equilibrium phase.

For the equilibrium phase

$$V_0 = (1, 0, 0, 0, 0)$$

Equation (6) reduces to

$$J(F^*) = \begin{bmatrix} -\mu_h & 0 & 0 & 0 & -\frac{\beta_h C}{\mu_v} \\ 0 & -\mu_h - \alpha_h & 0 & 0 & \frac{\beta_h C}{\mu_v} \\ 0 & \alpha_h & -\mu_h - r & 0 & 0 \\ 0 & 0 & \beta_v N_T & -\alpha_v - \mu_v & 0 \\ 0 & 0 & 0 & \alpha_v & -\mu_v \end{bmatrix} \quad (8)$$

The characteristic equation is obtained by solving

$$\det(J - \zeta I) = 0$$

$$(\zeta + \mu_h)(\zeta^4 + b_3\zeta^3 + b_2\zeta^2 + b_1\zeta + b_0) = 0 \quad (9)$$

with

$$b_3 = \alpha_v + (W + H)\mu_h + 2\mu_v$$

$$b_2 = W H \mu_h^2 \alpha_v + 2(W + H)\mu_h \mu_v + \mu_v^2 + \alpha_v(W + H)\mu_h + \mu_v$$

$$b_1 = \mu_h(\alpha_v(W H \mu_h + (W + H)\mu_v) + \mu_v(2W H \mu_h + (W + H)\mu_v))$$

$$b_0 = W H \mu_h^2 \mu_v(1 - E_0)(\alpha_v + \mu_v)$$

So we have five eigenvalues corresponding to (9). We represent these eigenvalues by $\zeta_1, \zeta_2, \zeta_3, \zeta_4$ and ζ_5 . Clearly $\zeta_1 = -\mu_h$ has negative real part. The other four eigenvalues can be obtained by solving

$$\zeta^4 + b_3\zeta^3 + b_2\zeta^2 + b_1\zeta + b_0 = 0.$$

These four eigenvalues have negative real part if they satisfy the Ruth-Hurwitz criteria [6,7], with $b_3 > 0, b_1 > 0, b_0 > 0$, and $b_1 b_2 b_3 > b_1^2 + b_3^2 b_0$.

It can be seen that coefficients b_0, b_1, b_3 are greater than zero, when $E_0 < 1$. Evaluating

$$\begin{aligned} b_1 b_2 b_3 - (b_1^2 + b_3^2 b_0) &= (\alpha_v + (W + H)\mu_h + 2\mu_v)(W H \mu_h^2 \alpha_v + 2(W + H)\mu_h \mu_v + \mu_v^2 + \alpha_v(W + H)\mu_h \\ &\quad + \mu_v)(\mu_h(\alpha_v(W H \mu_h + (W + H)\mu_v) + \mu_v(2W H \mu_h + (W + H)\mu_v))) \\ &\quad - ((\mu_h(\alpha_v(W H \mu_h + (W + H)\mu_v) + \mu_v(2W H \mu_h + (W + H)\mu_v)))^2 \\ &\quad + (\alpha_v + (W + H)\mu_h + 2\mu_v)^2(W H \mu_h^2 \mu_v(1 - E_0)(\alpha_v + \mu_v))) \\ &= \mu_h(W + H)(W\mu_h + \mu_v)(W\mu_h + \mu_v + \alpha_v)(H\mu_h + \mu_v)(H\mu_h + \mu_v + \alpha_v)(2\mu_v + \alpha_v) + \\ &\quad \alpha_v \alpha_h \gamma_h \gamma_v (\alpha_v + (W + H)\mu_h + 2\mu_v)^2 \end{aligned}$$

which tells us $b_1 b_2 b_3 > b_1^2 + b_3^2 b_0$ or $b_1 b_2 b_3 - (b_1^2 + b_3^2 b_0)$ is every time positive. So the disease-free equilibrium phase is non-global stability for $E_0 < 1$.

For the endemic equilibrium phase V_1 , the equation of characteristic is

$$\zeta^5 + a_4\zeta^4 + a_3\zeta^3 + a_2\zeta^2 + a_1\zeta + a_0 = 0 \quad (10)$$

$$a_4 = \alpha_v + (1 + W + H)\mu_h + 2\mu_v + \frac{\mu_h \mu_v (E_0 - 1)(\mu_v + \alpha_v)}{\alpha_v(\gamma_h + \mu_h) + \mu_h \mu_v} + \frac{(E_0 - 1)W H \mu_h^3 \mu_v}{\alpha_h \gamma_v \mu_h + W H \mu_h^2 \mu_v}$$

$$\begin{aligned}
a_3 = & \mu_v^2 + \mu_h \mu_v \left\{ 2(1 + W + H) + \frac{\mu_v(E_0 - 1)(\mu_v + \alpha_v)}{\alpha_v(\gamma_h + \mu_h) + \mu_h \mu_v} \right\} \\
& + \mu_h^2 \left\{ W + H + WH + \frac{\mu_v(1 + W + H)(E_0 - 1)(\mu_v + \alpha_v)}{\alpha_v(\gamma_h + \mu_h) + \mu_h \mu_v} \right\} \\
& + \frac{(E_0 - 1)WH\mu_h^3\mu_v\{(W + H)\mu_h + 2\mu_v\}}{\alpha_h\gamma_v\mu_h + WH\mu_h^2\mu_v} \\
& + \frac{\mu_h\mu_v(E_0 - 1)(\mu_v + \alpha_v)}{(\alpha_h\gamma_v\mu_h + WH\mu_h^2\mu_v)(\alpha_v(\gamma_h + \mu_h) + \mu_h\mu_v)} \\
& + \left\{ (1 + W + H)\mu_h + \mu_v + \frac{\mu_h\mu_v(E_0 - 1)(\mu_v + \alpha_v)}{\alpha_v(\gamma_h + \mu_h) + \mu_h\mu_v} + \frac{(E_0 - 1)WH\mu_h^3\mu_v}{\alpha_h\gamma_v\mu_h + WH\mu_h^2\mu_v} \right\} \alpha_v \\
\\
a_2 = & \mu_h \left\{ WH\mu_h^2 + 2(WH + W + H)\mu_h\mu_v + (1 + W + H)\mu_v^2 \right. \\
& + \frac{\mu_h\mu_v(E_0 - 1)(\mu_v + \alpha_v)((W + H + WH)\mu_h + (1 + W + H)\mu_v)}{\alpha_v(\gamma_h + \mu_h) + \mu_h\mu_v} \\
& + \frac{WH\mu_h^2\mu_v(E_0 - 1)\{WH\mu_h^2 + 2(W + H)\mu_h\mu_v + \mu_v^2\}}{\alpha_h\gamma_v\mu_h + WH\mu_h^2\mu_v} \\
& + \frac{WH\mu_h^2\mu_v(E_0 - 1)\left\{\frac{\mu_h\mu_v(E_0 - 1)(\mu_v + \alpha_v)((W + H)\mu_h + \mu_v)}{\alpha_v(\gamma_h + \mu_h) + \mu_h\mu_v}\right\}}{\alpha_h\gamma_v\mu_h + WH\mu_h^2\mu_v} \\
& + \alpha_v \left\{ (WH + W + H)\mu_h + (1 + W + H)\mu_v \right. \\
& + \frac{\mu_v\mu_h(1 + W + H)(E_0 - 1)(\mu_v + \alpha_v)}{\alpha_v(\gamma_h + \mu_h) + \mu_h\mu_v} \\
& \left. \left. + \frac{WH\mu_h^2\mu_v(E_0 - 1)\left\{(W + H)\mu_h + \mu_v + \frac{\mu_h\mu_v(E_0 - 1)(\mu_v + \alpha_v)}{\alpha_v(\gamma_h + \mu_h) + \mu_h\mu_v}\right\}}{\alpha_h\gamma_v\mu_h + WH\mu_h^2\mu_v} \right\} \right\}
\end{aligned}$$

$$\begin{aligned}
 a_1 = \mu_h^2 & \left\{ \frac{\mu_h^2 \mu_v WH (E_0 - 1) (\mu_v + \alpha_v) \left(1 + \frac{H(E_0 - 1) \mu_h^2 \mu_v}{\alpha_h \gamma_v \mu_h + H \mu_h^2 \mu_v} \right)}{\alpha_v (\gamma_h + \mu_h) + \mu_h \mu_v} \right. \\
 & + \mu_v^2 \left(W + H + WH + \frac{H(W + H)(E_0 - 1) \mu_h^2 \mu_v}{\alpha_h \gamma_v \mu_h + H \mu_h^2 \mu_v} \right) \\
 & + \mu_v \mu_h \left(2WH + \frac{\mu_v (WH + W + H)(E_0 - 1) (\mu_v + \alpha_v)}{\alpha_v (\gamma_h + \mu_h) + \mu_h \mu_v} \right. \\
 & \left. \left. + \frac{H \mu_h^2 \mu_v (E_0 - 1) \left\{ 2WH + \frac{\mu_v (E_0 - 1)(W + H)(\mu_v + \alpha_v)}{\alpha_v (\gamma_h + \mu_h) + \mu_h \mu_v} \right\}}{\alpha_h \gamma_v \mu_h + H \mu_h^2 \mu_v} \right) \right. \\
 & + \alpha_v \left(WH \mu_h + (W + H + WH) \mu_v + \frac{\mu_h \mu_v (E_0 - 1)(W + H + WH)(\mu_v + \alpha_v)}{\alpha_v (\gamma_h + \mu_h) + \mu_h \mu_v} \right. \\
 & \left. \left. + \frac{H \mu_h^2 \mu_v (E_0 - 1) \left\{ WH \mu_h + (W + H) \mu_v + \frac{\mu_h \mu_v (E_0 - 1)(W + H)(\mu_v + \alpha_v)}{\alpha_v (\gamma_h + \mu_h) + \mu_h \mu_v} \right\}}{\alpha_h \gamma_v \mu_h + H \mu_h^2 \mu_v} \right) \right\} \\
 a_0 = (\mu_v + \alpha_v) \mu_h \mu_v & \left(WH \mu_h^2 \left(1 + \frac{H(E_0 - 1) \mu_h^2 \mu_v}{\alpha_h \gamma_v \mu_h + H \mu_h^2 \mu_v} \right) \left(1 + \frac{\mu_h (E_0 - 1) (\mu_v + \alpha_v)}{\alpha_v (\gamma_h + \mu_h) + \mu_h \mu_v} \right) \right)
 \end{aligned}$$

Equation (10) corresponds five eigenvalues. We represent these five eigenvalues by $\zeta_1, \zeta_2, \zeta_3, \zeta_4$ and ζ_5 . These five eigenvalues have negative real parts if they satisfy the Routh-Hurwitz criteria [6, 7], that is,

$$a_i > 0, \quad \text{for } i = 0, 1, 2, 3, 4$$

$$a_2 a_3 a_4 > a_2^2 + a_4^2 a_1$$

$$(a_1 a_4 - a_0)(a_4 a_3 a_2 - a_2^2 - a_4^2 a_1) > a_0(a_4 a_3 - a_2)^2 + a_4 a_0^2$$

If all these conditions satisfy and will satisfy (already checked) for $E_0 > 1$. Thus, the endemic equilibrium phase is non-global stability for $E_0 > 1$.

5. NSFD DISCRETIZATION FOR FRACTIONAL-ORDER DENGUE MODEL

In this section we shall construct Non Standard Finite Difference Scheme proposed by Mickens [2, 13], for the system (4) and swapping the step size h by a function $\psi(h)$ and using GL discretization technique, it can be seen that

$$\sum_{j=0}^{n+1} C_j^{\gamma_1} S^{n+1-j} = \mu_h - \beta_h S^{n+1} I_v^n \left(\frac{C}{\mu_v} \right) - \mu_h S^{n+1} \quad (11)$$

$$\sum_{j=0}^{n+1} C_j^{\gamma_2} X^{n+1-j} = \beta_h S^{n+1} I_v^n \left(\frac{C}{\mu_v} \right) - \alpha_h X^{n+1} - \mu_h X^{n+1} \quad (12)$$

$$\sum_{j=0}^{n+1} C_j^{\gamma_3} I^{n+1-j} = \alpha_h X^{n+1} - r I^{n+1} - \mu_h I^{n+1} \quad (13)$$

$$\sum_{j=0}^{n+1} C_j^{\gamma_4} X_v^{n+1-j} = \beta_v I^{n+1} N_T (1 - X_v^{n+1} - I_v^n) - \alpha_v X_v^{n+1} - \mu_v X_v^{n+1} \quad (14)$$

$$\sum_{j=0}^{n+1} C_j^{\gamma_5} I_v^{n+1-j} = \alpha_v X_v^{n+1} - \mu_v I_v^{n+1} \quad (15)$$

$$(11) \Rightarrow S^{n+1} = \frac{\mu_h - \sum_{j=1}^{n+1} C_j^{\gamma_1} S^{n+1-j}}{(C_0^{\gamma_1} + \beta_h I_v^n \left(\frac{C}{\mu_v} \right) + \mu_h)} \quad (16)$$

$$(12) \Rightarrow X^{n+1} = \frac{\beta_h S^{n+1} I_v^n \left(\frac{C}{\mu_v} \right) - \sum_{j=1}^{n+1} C_j^{\gamma_2} X^{n+1-j}}{C_0^{\gamma_2} + \alpha_h + \mu_h} \quad (17)$$

$$(13) \Rightarrow I^{n+1} = \frac{\alpha_h X^{n+1} - \sum_{j=1}^{n+1} C_j^{\gamma_3} I^{n+1-j}}{C_0^{\gamma_3} + r + \mu_h} \quad (18)$$

$$(14) \Rightarrow X_v^{n+1} = \frac{\beta_v I^{n+1} N_T - \beta_v I^{n+1} N_T I_v^n - \sum_{j=1}^{n+1} C_j^{\gamma_4} X_v^{n+1-j}}{C_0^{\gamma_4} + \beta_v I^{n+1} N_T + \alpha_v + \mu_v} \quad (19)$$

$$(15) \Rightarrow I_v^{n+1} = \frac{\alpha_v X_v^{n+1} - \sum_{j=1}^{n+1} C_j^{\gamma_5} I_v^{n+1-j}}{C_0^{\gamma_5} + \mu_v} \quad (20)$$

$$\text{with } C_0^{n_1} = \left(\frac{e^{\mu_h h} - 1}{\mu_h} \right)^{-\gamma_1}, \quad C_0^{n_2} = \left(\frac{e^{(\alpha_h + \mu_h)h} - 1}{(\alpha_h + \mu_h)} \right)^{-\gamma_2}, \quad C_0^{n_3} = \left(\frac{e^{(r + \mu_h)h} - 1}{r + \mu_h} \right)^{-\gamma_3},$$

$$C_0^{n_4} = \left(\frac{e^{(\alpha_h + \mu_h)h} - 1}{(\alpha_h + \mu_h)} \right)^{-\gamma_4} \text{ and } C_0^{n_5} = \left(\frac{e^{\mu_v h} - 1}{\mu_v} \right)^{-\gamma_5}$$

5.1 Numerical Experiments

Analytical studies permanently remain unfinished without numerical authentication of the outcomes. In this unit, we present numerical simulation to exemplify the outcomes attained in previous sections. Now we solve the fractional-order dengue model in two cases with step size $h = 1.1$ and $h = 2.4$. The guestimate elucidations are revealed in Fig. 2-19, for various values of $0 < n_i \leq 1$, $i = 1, \dots, 5$. Numerical experiments are performed using values of parameters given in Table 2.

Table 2. Different parameters & values.

Parameter	Value (day ⁻¹)
N_T	5,000
α_h	1/5
β_h	0.00005
μ_h	0.0000391
α_v	1/10
β_v	0.00008
μ_v	1/14
r	1/14
$C(\text{DFE})$	3.00
$C(\text{EE})$	300

6. RESULTS AND DISCUSSION

The numerical modeling of transmission dynamics of Fractional Order dengue disease with incubation period of virus has been analysed in this paper. The model has two equilibrium points, i.e. disease free equilibrium (DFE) and endemic equilibrium (EE). An unconditionally convergent non-standard finite difference numerical model with GL coefficients has been constructed and numerical experiments are performed for different values of discretization parameter h . Fig. (2-10) shows the graphs of disease free equilibrium with step size $h = 1.1$ and Fig. (11-19) with step size $h = 2.4$. Numerical Simulations reveals that all values approaches to equilibrium point. In order to observe the effects that the parameter γ has on the dynamics of the fractional-order model (4), we conclude several numerical simulations varying the value of parameter. These simulations reveal that a change of the value γ affects the dynamics of the epidemic. For example, Fig. 2, 11 shows that for lower values of γ , the epidemic peak is wider and lower from the true equilibrium points, Fig. 4, 6, 8, 10, 13, 15, 17, and 19 show that for lower values of γ , the epidemic peak is wider and higher for true equilibria. This feature is important from an epidemiological point of view since its interpretation shows a longer period in which infected & infectious individuals can affect the health system. Fig. 2-19 show that the model presented here gradually approaches the steady state for different values of γ but the dynamics of the model is governed by the distinct paths.

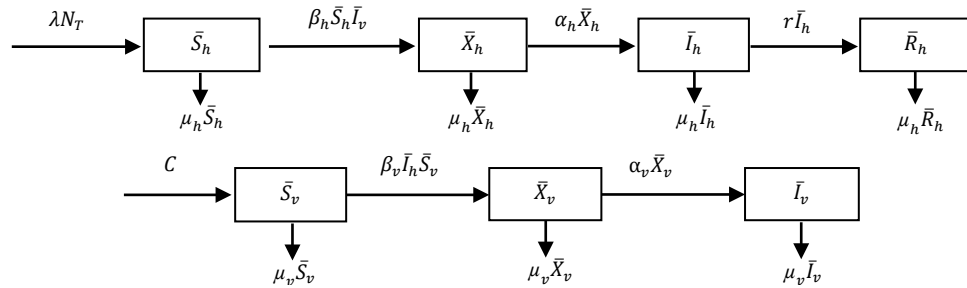


Fig.1. Flow diagram.

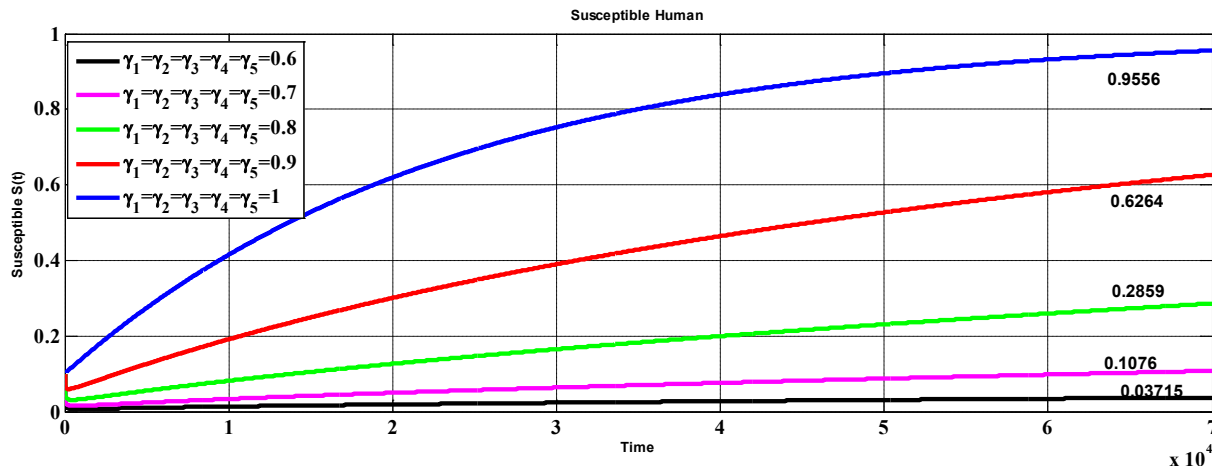


Fig. 2. The susceptible humans for different values of γ 's with $h = 1.1$.

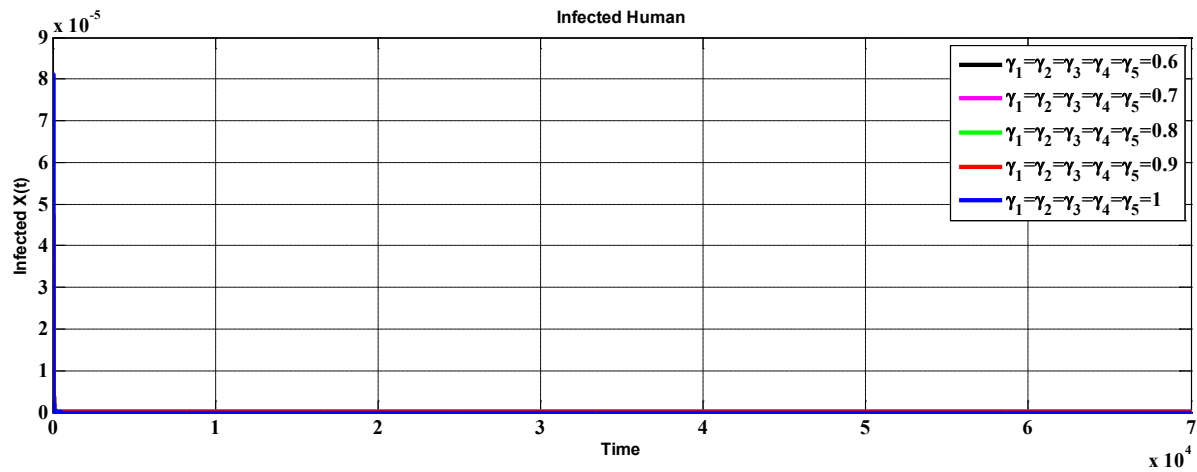


Fig. 3. The infected humans for different values of γ 's with $h = 1.1$.

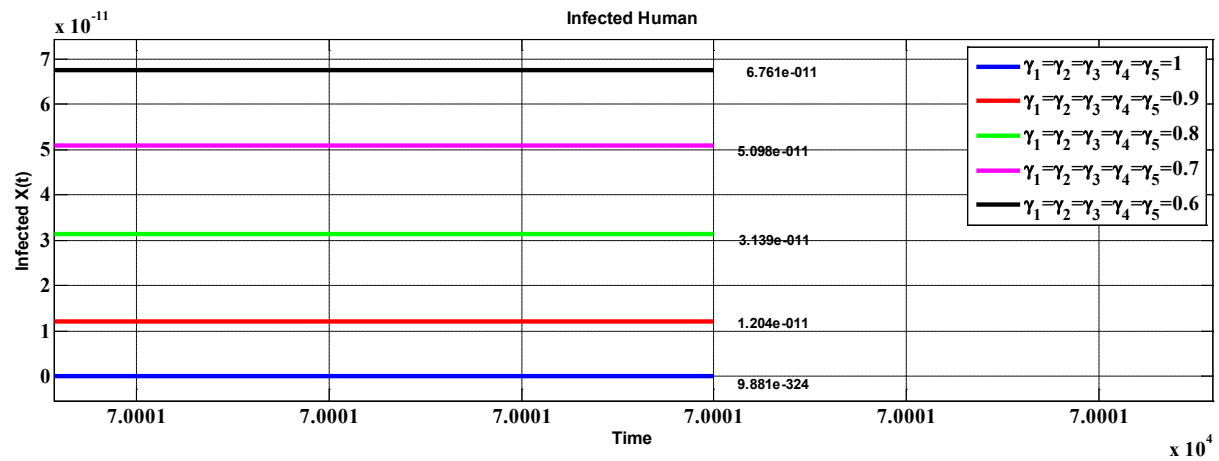


Fig. 4. The infected humans, in zoom.

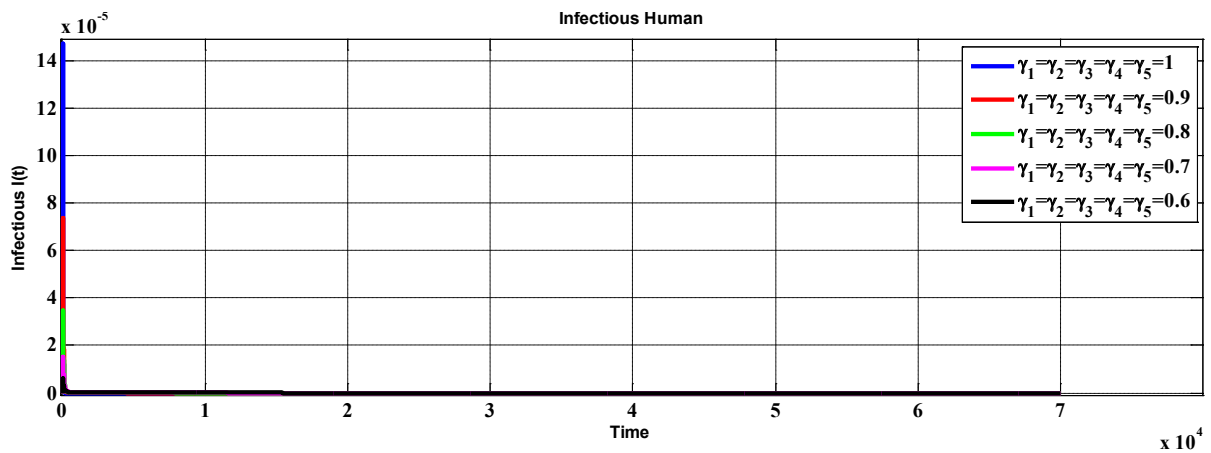


Fig. 5. The infectious humans for different values of γ 's with $h = 1.1$.

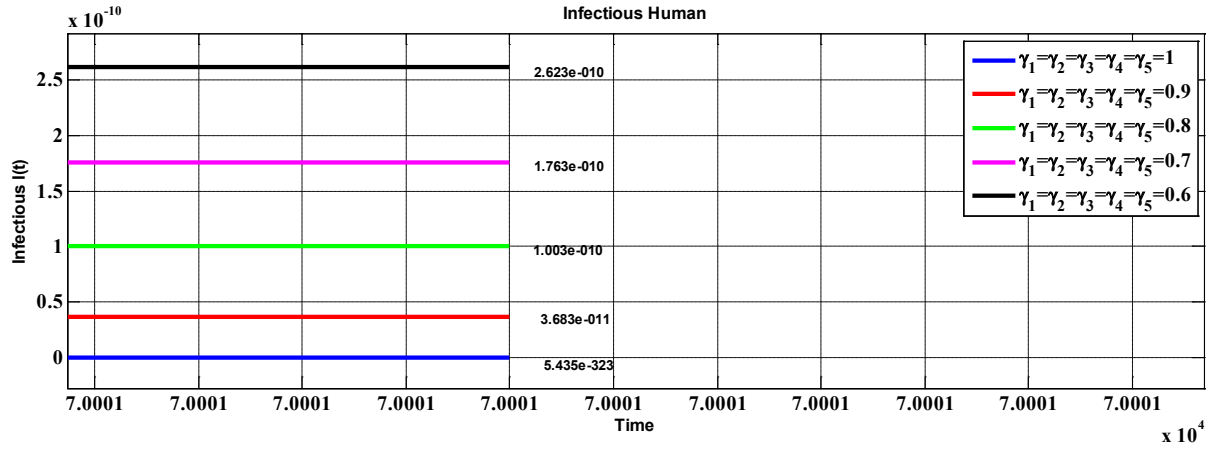


Fig. 6. The infectious humans, in zoom.

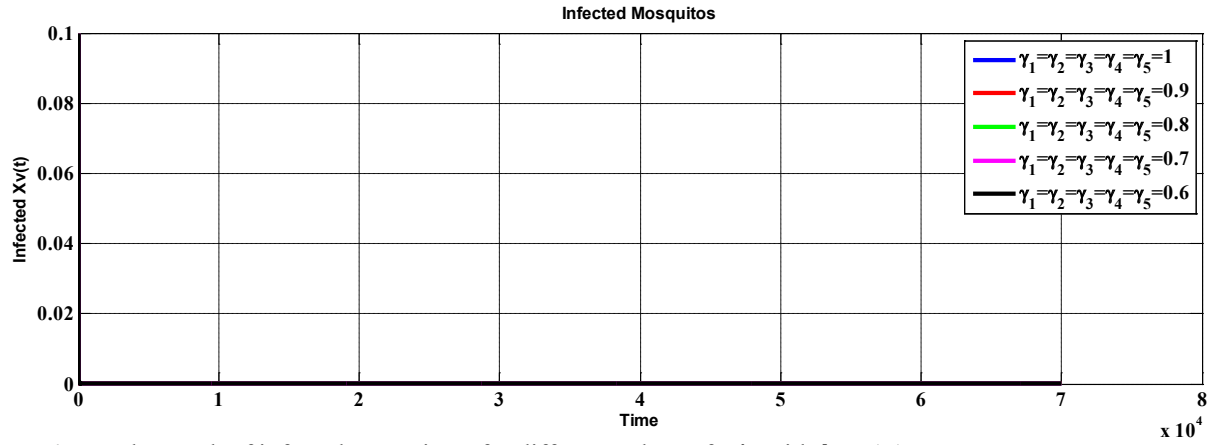


Fig. 7. The graph of infected mosquitoes for different values of γ 's with $h = 1.1$.

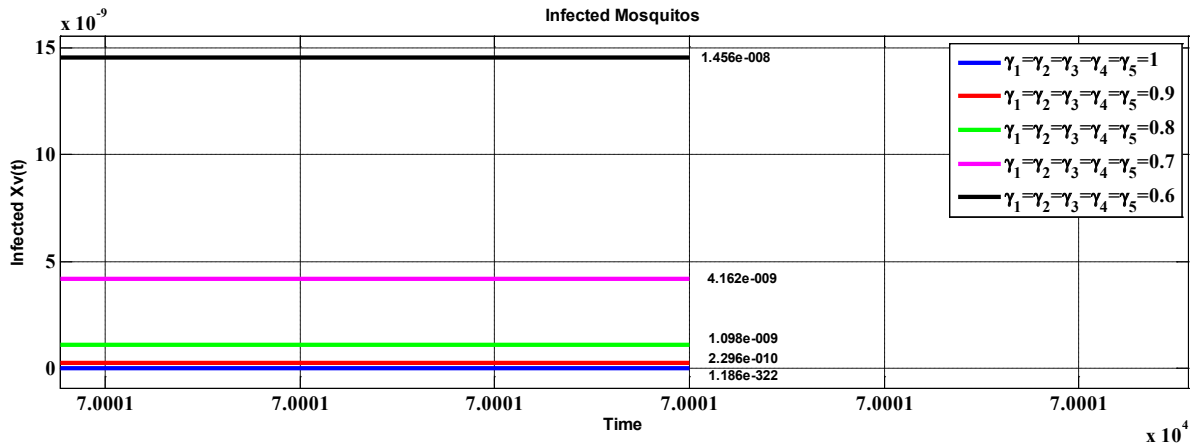


Fig. 8. The infected mosquitoes, in zoom.

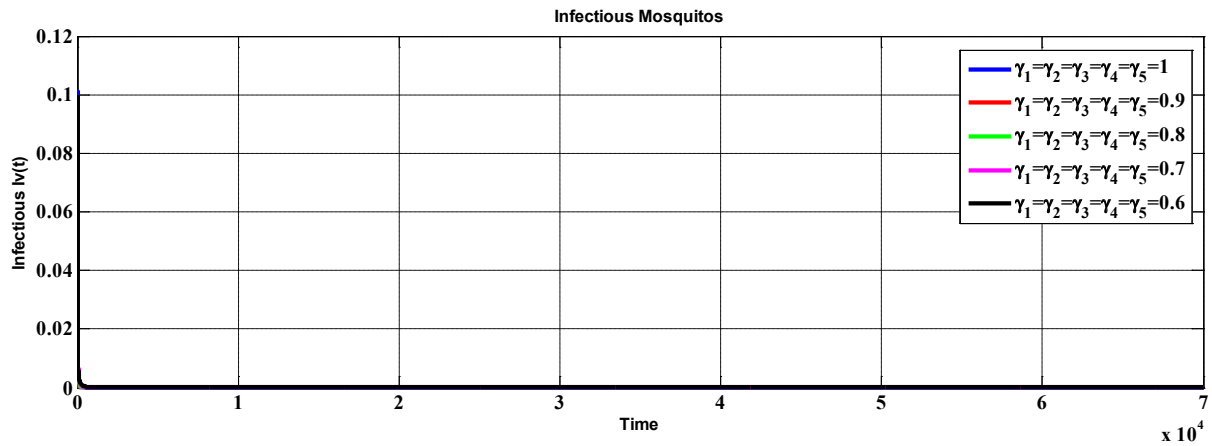


Fig. 9. The infectious mosquitoes for different values of γ 's with $h = 1.1$.

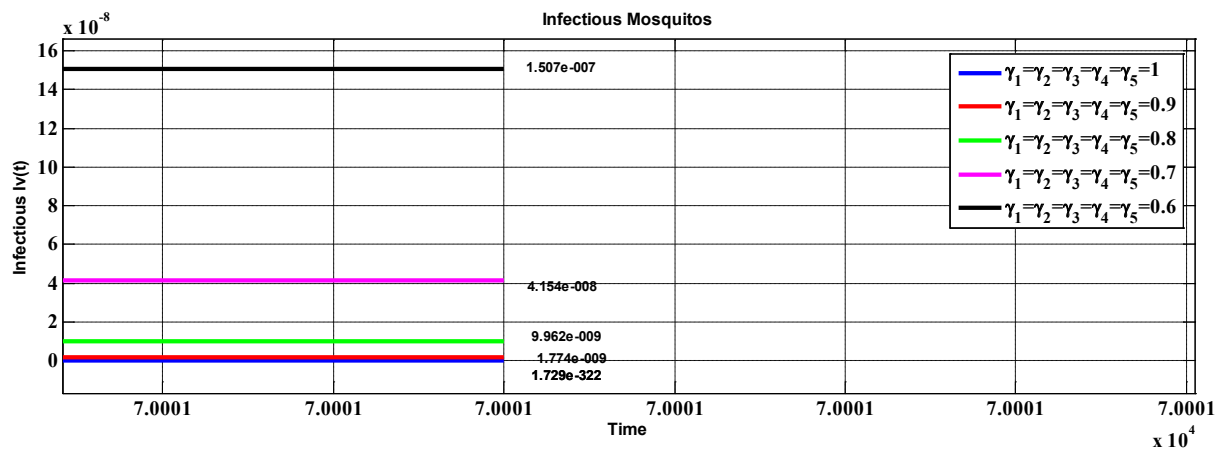


Fig. 10. The infectious mosquitoes in zoom.

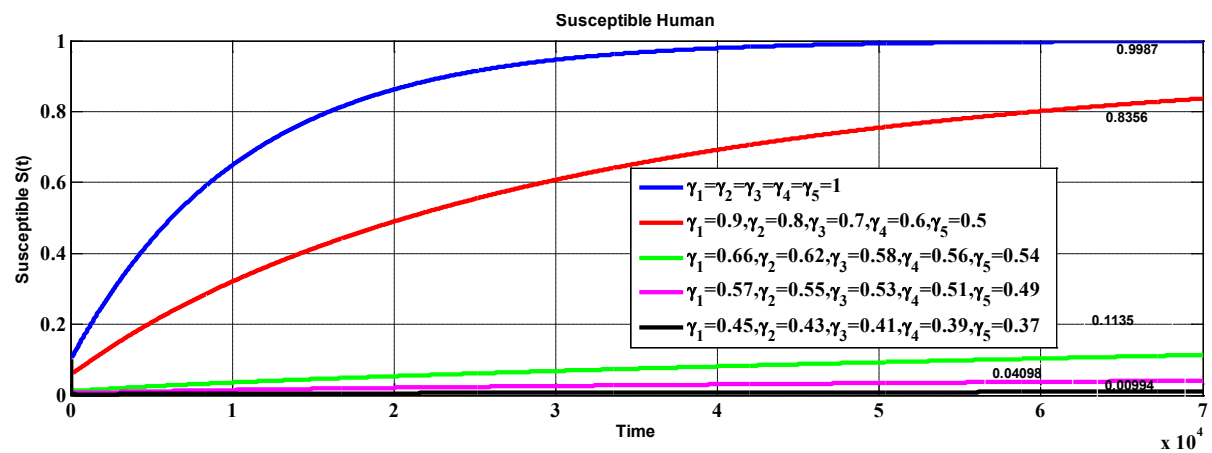


Fig. 11. The susceptible humans for different values of γ 's with $h = 2.4$.

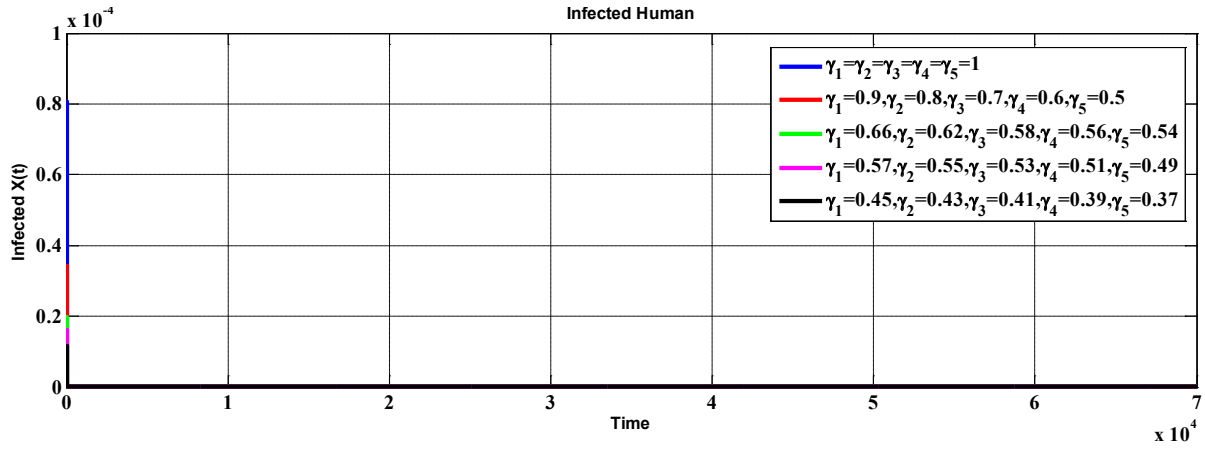


Fig. 12. The infected humans for different values of γ 's with $h = 2.4$.

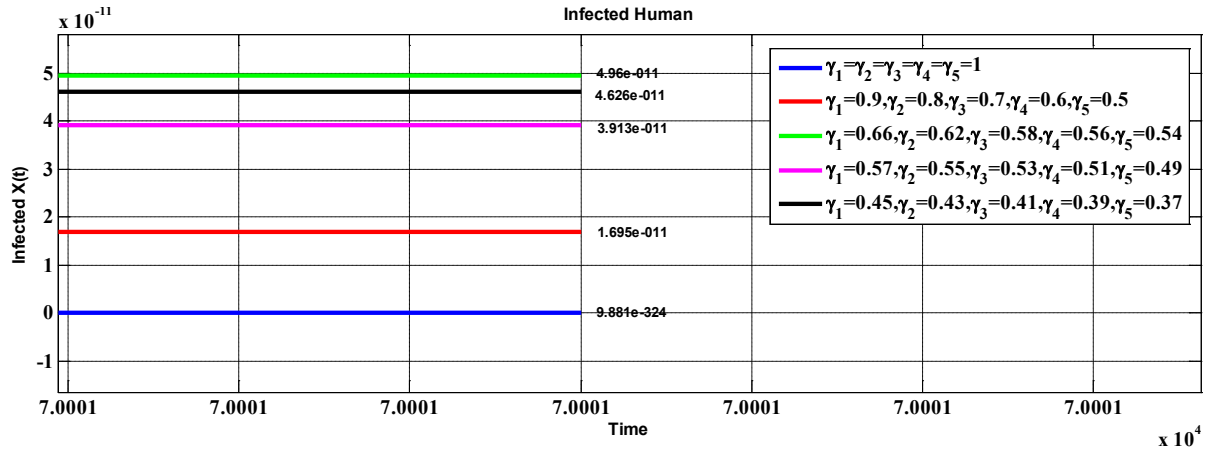


Fig. 13. The infected humans, in zoom.

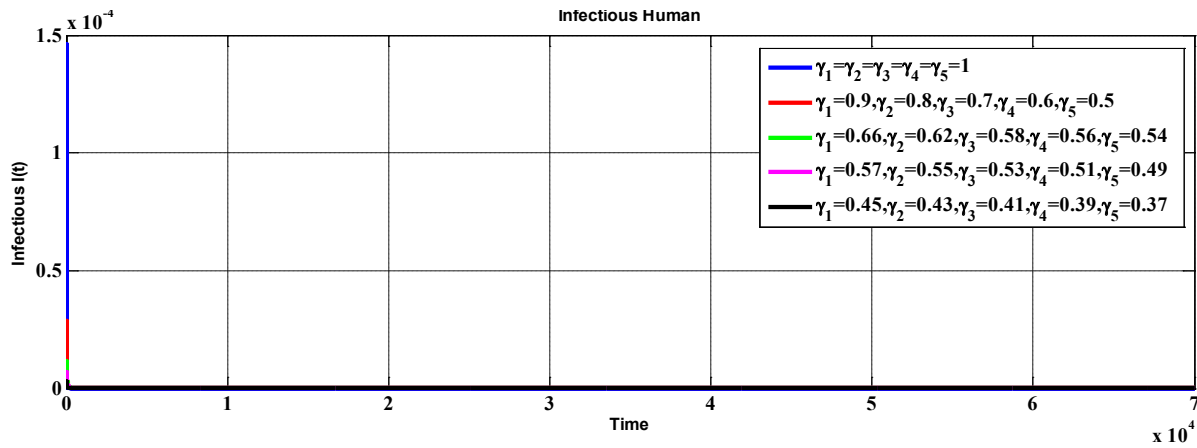


Fig. 14. The infectious humans for different values of γ 's with $h = 2.4$.

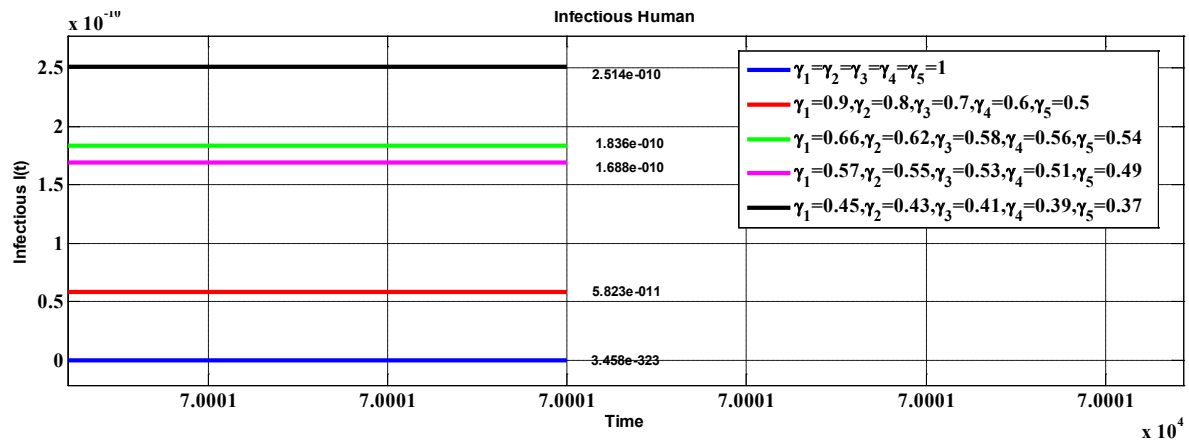


Fig. 15. The infectious humans, in zoom.

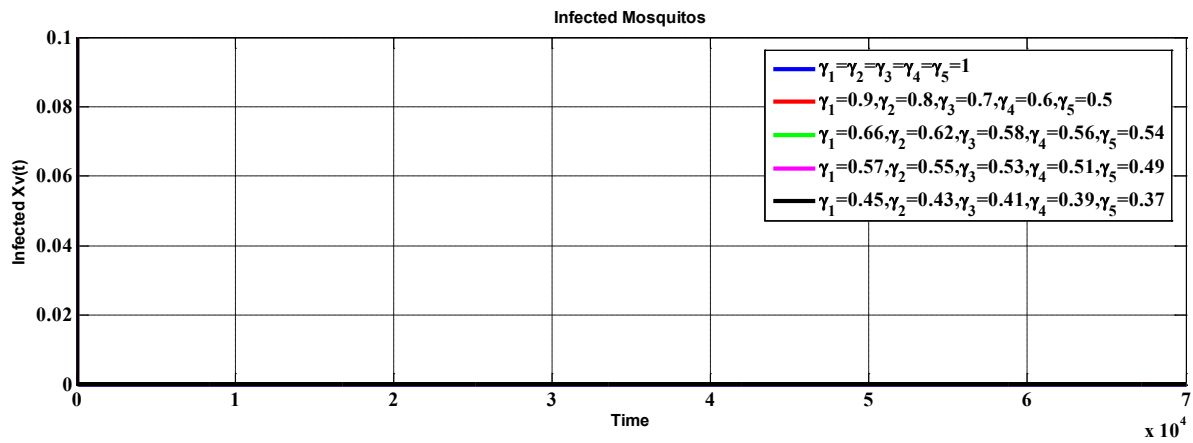
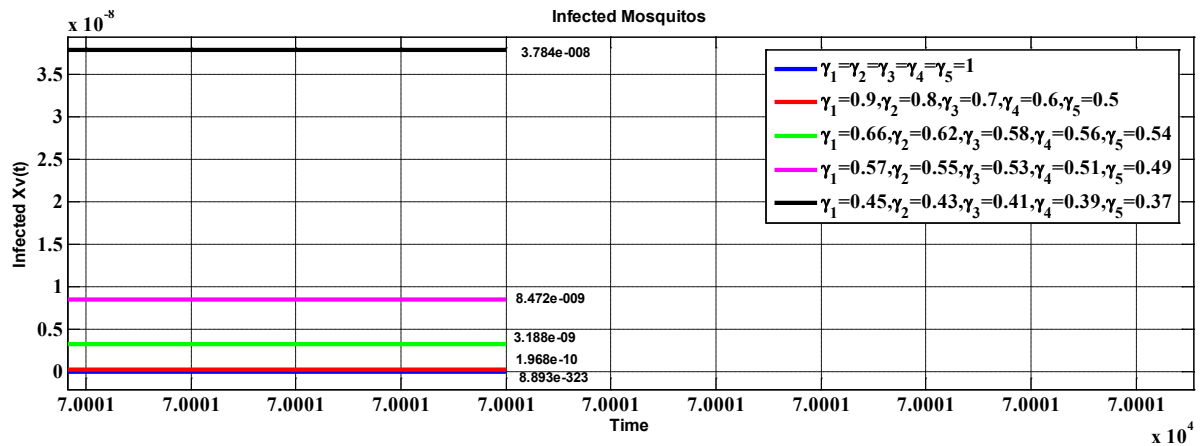
Fig. 16. The infected mosquitoes for different values of γ 's with $h = 2.4$.

Fig. 17. The infected mosquitoes, in zoom.

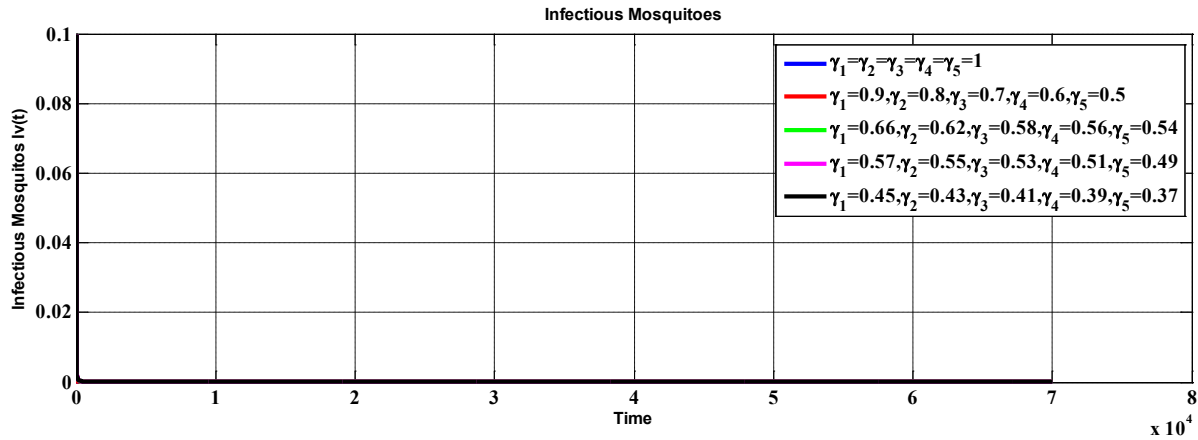


Fig. 18. The infectious mosquitoes for different values of γ 's with $h = 2.4$.

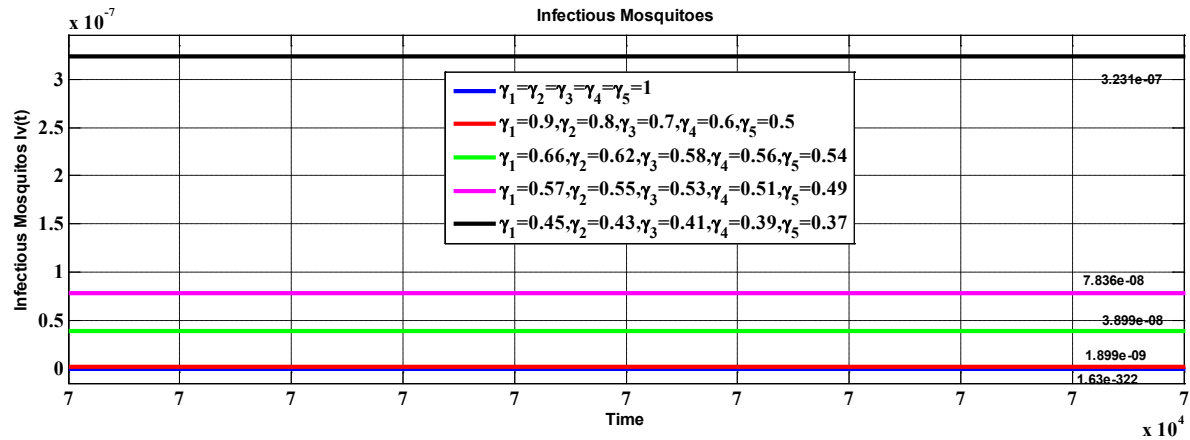


Fig. 19. The infectious mosquitoes, in zoom.

6. CONCLUSIONS

Describing the reality through a mathematical model, usually a system of differential equations, is hard task that has an inherent compromise between simplicity and accuracy. In this article we studied the fractional-order dengue model. It turns out that, in general, this classical model does not provide enough good results. In order to get better results, that fit the reality, fractional order system is needed. It allows us to model memory effects, and result in a more powerful approach to epidemiological models. Our investigation show that even a simple fractional model may give surprisingly good results. From the obtained results from the presented figures, it turns out that the results are non-negative because susceptible, infected and recovered can never be less than zero. Then the local stability analysis of the model in fractional order is presented. The results obtained are in agreement with the numerical simulations attained from the graph.

7. REFERENCES

1. Yıldırım, A. & Y. Cherruault. Analytical approximate solution of a SIR epidemic model with constant vaccination strategy by homotopy perturbation method. *Kybernetes* 38(9): 1566-1575 (2009).
2. Makinde, O.D. Adomian decomposition approach to a SIR epidemic model with constant vaccination strategy. *Applied Mathematics & Computation* 184(2): 842-848 (2007).
3. Arafa, A.A.M., S.Z. Rida & M. Khalil. Fractional modeling dynamics of HIV and 4 T-cells during primary Infection. *Nonlinear Biomedical Physics* 6: 1-7 (2012).

4. Hethcote, H.W. The mathematics for infectious diseases, *Siam Review* 42(4): 599-653 (2000).
5. Biazar, J. Solution of the epidemic model by adomian decomposition method. *Applied Mathematics & Computation* 173(2):1101–1106 (2006).
6. Busenberg, S. & P. Driessche. Analysis of a disease transmission model in a population with varying size. *Journal of Mathematical Biology* 28:257- 270 (1990).
7. El-Sayed, A.M.A, S.Z. Rida & A.A.M. Arafa. On the solutions of time-fractional bacterial chemotaxis in a diffusion gradient chamber. *International Journal of Nonlinear Science* 7: 485-492 (2009).
8. Hassan, H.N. & M.A. El-Tawil. A new technique of using homotopy analysis method for solving high-order non-linear differential equations. *Mathematical Methods in Applied Science* 34:728–742(2011).
9. Liao, S.J. A kind of approximate solution technique which does not depend upon small parameters: a special Example. *International Journal of Non-Linear Mechanics* 30:371–380 (1995).
10. Liao, S.J. *Beyond Perturbation: Introduction to the Homotopy Analysis Method*. Chapman & Hall/CRC Press, Boca Raton (2003).
11. Zibaei, S. & M. Namjoo. A nonstandard finite difference scheme for solving fractional-order Model of HIV-1 infection of CD4+ T-cells. *Iranian Journal of Mathematical Chemistry* 6(2): 169-184(2015).
12. Ahmad, E., A.M. Atial, El-Sayed & H.A.A. El-Saka. On some Routh-Hurwitz conditions for fractional order differential equations and their applications in Lorenz, Rossler, Chua and Chen systems. *Physics Letters A* 358(1): 1-4 (2006).
13. Mickens, R.E. Calculation of denominator functions for nonstandard finite difference schemes for differential equations satisfying a positivity condition. *Numerical Methods of partial Differential Equations* 23(3): 672-691 (2007).
14. Matignon, D. Stability result on fractional differential equations with applications to control processing to control processing, In: *Computational Engineering in Systems Applications(Conference)*, p. 963–968 (1996).
15. Zafar, Z., K. Rehan, M. Mushtaq & M. Rafiq. Numerical modelling for nonlinear biochemical reaction networks. *Iranian Journal of Mathematical Chemistry* (Accepted for publication).
16. Pooseh, S., H.S. Rodrigues, & D.F.M. Torres. Fractional derivatives in dengue epidemics. doi: 10.1063/1.3636838 (2011).
17. Jan, R., & A. Jan. MSGDTM for solution of fractional order dengue disease model. *International Journal of Science and Research* 6(3): 1140-1144 (2017).
18. Al-Sulami, H., M. El-Shahed, J.J. Nieto, & W. Shammakh. On fractional order dengue epidemic model. *Mathematical Problems in Engineering*, <http://dx.doi.org/10.1155/2014/456537> (2014).
19. Metzler, R., & J. Klafter. The random walk's guide to anomalous diffusion: a fractional dynamics approach, *Physics Reports* 339:1-77 (2000).
20. West, B.J., P. Grigolini, & R. Metzler. Nonnenmacher, TF: Fractional diffusion and Le'vy stable processes. *Physics Review E*. 55(1): 99-106 (1997).
21. Golmankhaneh, A.K., R. Arefi, & D. Baleanu. Synchronization in a nonidentical fractional order of a proposed modified system. *Journal of Vibration and Control*, 21(6): 1154-1161 (2015).
22. Baleanu, D., A.K. Golmankhaneh, A.K. Golmankhaneh, & R.R. Nigmatullin. Newtonian Law with memory. *Nonlinear Dynamics* 60: 81-86 (2010).
23. Agila, A., D. Baleanu, R. Eid, & B. Irfanoglu. Applications of the extended fractional euler- lagrange equations model to freely oscillating dynamical systems. *Romanian Journal of Physics* 61(3-4): 350-359 (2016).
24. Baleanu, D & O.G. Mustafa. On the global existence of solutions to a class of fractional differential equations. *Computers & Mathematics with Applications* 59: 1835-1841 (2010).
25. He, J, Li, Z, Wang, Q: A new fractional derivative and its application to explanation of polar bear basis. *Journal of King Saud University-Science* 28:190-192 (2016).
26. Oliveira, E.C., & J.A.T. Machado. A review of definitions for fractional derivatives and Integral. *Mathematical Problems in Engineering* (2014). <http://dx.doi.org/10.1155/2014/238459>.
27. Caputo, M, & M. Fabrizio. A new definition of fractional derivative without singular kernel. *Progress in Fractional Differentiations and Applications* 1(2):73-85 (2015).
28. Atangana, A., & D. Baleanu. New fractional derivatives with non-local and non-singular kernel. *Thermal Science* 20(2):763-769 (2016).
29. Zafar, Z., K. Rehan, & M. Mushtaq. Fractional-order scheme for bovine babesiosis disease and tick populations. *advances in difference equations*. p. 86 (2017). <http://dx.doi.org/10.1186/s13662-017-1133-2>.
30. Zafar, Z., K. Rehan, M. Mushtaq, & M. Rafiq. Numerical Treatment for nonlinear Brusselator Chemical Model. *Journal of Difference Equations and Applications* 23(3): 521-538 (2017).
31. Zafar, Z., K. Rehan, & M. Mushtaq. HIV/AIDS epidemic fractional-order model. *Journal of Difference Equations and Applications* 23(7): 1298-1315 (2017).



Fractional Numerical Treatment for Biochemical Reaction Networks

Zain Ul Abadin Zafar^{*1,2}, Kashif Rehan³, M. Mushtaq¹, and M. Rafiq⁴

¹Department of Mathematics, University of Engineering and Technology, Lahore, Pakistan

²Department of Mathematics, University of Engineering and Technology, KSK Campus, Lahore, Pakistan

³Faculty of Information Technology, University of Central Punjab, Lahore, Pakistan

⁴Faculty of Engineering, University of Central Punjab, Lahore, Pakistan

Abstract: Nowadays, numerical models have great importance in every field of science, especially for solving the nonlinear differential equations, partial differential equations, biochemical reactions, etc. In this article, we familiarize fractional-order into a model of Michaelis-Menten. We learned the influence of the changing of different values of fractional order. We display that the model familiarize in this article has nonnegative elucidations. We have checked the stability of the system. Numerical replications are also offered to confirm the attained results.

Keywords: Michaelis-Menten model, NSFD method, fractional order differential equation

1. INTRODUCTION

The enzyme kinetics model is a chemical model which includes a nonlinear reaction. The model consists of the binding/unbinding of enzyme and substrate, and production of the product. The model mechanism is described as follows:



where E , S , ES and P denote enzyme, substrate, enzyme-substrate complex and product, respectively, and k_1 , k_{-1} and k_2 denote the rates of reactions. If we denote the concentrations of E , S , ES , P by y_1 , y_2 , y_3 , y_4 , respectively, and $\mathbf{y} = (y_1, y_2, y_3, y_4)^T$, we write the governing equation as

$$\frac{d\mathbf{y}}{dt} = \begin{bmatrix} -1 & 1 & 1 \\ -1 & 1 & 0 \\ 1 & -1 & -1 \\ 0 & 0 & 1 \end{bmatrix} \begin{bmatrix} k_1 y_1 y_2 \\ k_{-1} y_3 \\ k_2 y_3 \end{bmatrix} = \begin{bmatrix} -k_1 y_1 y_2 + k_{-1} y_3 + k_2 y_3 \\ -k_1 y_1 y_2 + k_{-1} y_3 \\ k_1 y_1 y_2 - k_{-1} y_3 - k_2 y_3 \\ k_2 y_3 \end{bmatrix}, \quad (2)$$

We assume a typical initial condition $(y_1, y_2, y_3, y_4) = (e_0, s_0, 0, 0)$. Since the substrate is exhausted and it produces the product P at the equilibrium, the equilibrium of the model can be founded easily as $(y_1, y_2, y_3, y_4) = (e_0, 0, 0, s_0)$. Since the conserved quantities for the model are $y_1 + y_3 + y_4 = s_0$ and $y_2 + y_3 = e_0$, one can reduce the above system (2) into

$$\begin{aligned} \frac{dy_1}{dt} &= -k_1 e_0 y_1 + k_1 y_1 y_3 + k_{-1} y_3 \\ \frac{dy_3}{dt} &= k_1 e_0 y_1 - k_1 y_1 y_3 - (k_{-1} + k_2) y_3 \end{aligned} \quad (3)$$

with the initial condition $(y_1, y_3) = (s_0, 0)$.

As in [1], to obtain the system of the non-dimensional variables from the above system (3) we define the following variables.

$$u(\tau) = \frac{y_1(t)}{s_0}, v(\tau) = \frac{(s_0 + K_m)y_3(t)}{s_0 e_0}, \tau = k_1(s_0 + K_m)t, \\ K_m = \frac{(k_{-1} + k_2)}{k_1}, \rho = \frac{k_{-1}}{k_2}, \epsilon = \frac{e_0}{s_0 + K_m}, \sigma = \frac{s_0}{K_m} \quad (4)$$

And

$$T = \epsilon(1 + \rho)k_2t = \frac{\epsilon(1 + \rho)k_2}{k_1(s_0 + K_m)}\tau$$

Then the system of (3) can be represented in dimensionless form as follows:

$$\frac{du}{dt} = -(1 + \sigma)u + \sigma uv + \frac{\rho}{1 + \rho}v \\ \epsilon \frac{dv}{dt} = (1 + \sigma)u - \sigma uv - v \quad (5)$$

subject to the initial condition $u(0) = 1$ and $v(0) = 0$ determined by (4).

2. OPENINGS AND CYPHERS

In this section, some elementary descriptions and things of the fractional calculus theory and nonstandard discretization are discussed.

2.1 Essentials of Fractional-order

Fractional differential equations (FDEs) have gained the considerable prominence owing to their submissions in various sciences, like mechanics, physics, engineering and chemistry [13]. In current years, the dynamic comportments of fractional-order differential systems have established increasing consideration. Although the concept of the fractional calculus was discussed in the same time interval of integer-order calculus, the complexity and the lack of applications postponed its progress till a few decades ago. Recently most of the dynamical systems based on the integer-order calculus have been modified into the fractional order domain due to the extra degrees of freedom and the flexibility which can be used to precisely fit the experimental data much better than the integer order modeling.

2.2 Grunwald-Letnikov (GL) Technique

The GL technique of guesstimate for the 1-D fractional derivative is as follows [13].

$$D^\beta x(t) = f(t, x(\tau)), \quad x(0) = x_0, \quad \tau \in [0, \tau_f], \quad (6)$$

$$D^\beta x(t) = \lim_{h \rightarrow 0} h^{-\beta} \sum_{j=0}^{\left[\frac{\tau_f}{h}\right]} (-1)^j \binom{\beta}{j} x(\tau - ih),$$

where $0 < \beta < 1$, D^β denotes the fractional derivative, h is the step size and $\left[\frac{\tau_f}{h}\right]$ represents the integer part of $\frac{\tau_f}{h}$. Therefore, Eq. (4) is discretized in the next form,

$$\sum_{i=0}^n C_j^\beta x_{n-j} = f(\tau_n, x_n), \quad n = 1, 2, 3, \dots$$

where $\tau_n = n h$ and C_j^β are the GL coefficients demarcated as

$$C_i^\beta = \left(1 - \frac{1+\beta}{i}\right) C_{i-1}^\beta, \quad C_0^\beta = h^{-\beta}, \quad i = 1, 2, 3, \dots$$

The Micken's paper [15] provides a common route for determining $\psi(h)$ for the ODEs.

A case of the NSFD discretization procedure is its submission to the decay equation

$$X' = -\xi X$$

where ξ is constant. The discretization scheme [15] is

$$\frac{X_{n+1}-X_n}{\psi} = -\xi X_n, \quad \psi(h, \xi) = \frac{1-e^{-\xi h}}{\xi}$$

Let us take another application given by

$$X' = \lambda_1 X - \lambda_2 X^2$$

where the NSFD scheme is

$$\begin{aligned} \frac{X_{n+1}-X_n}{\psi} &= \xi_1 X_n - \xi_2 X_n X_{n+1} \\ \psi(h, \xi_1) &= \frac{e^{\xi_1 h} - 1}{\xi_1} \end{aligned}$$

It ought to be noted that the NSFD schemes for both ODEs are exact in the logic that $X_n = X(\tau_n)$ for every pertinent values of $h > 0$.

3. FRACTIONAL ORDER CHEMICAL MODEL

The fractional order above said chemical model can be written as

$$\frac{d^{\gamma_1} X}{dt^{\gamma_1}} = -(1 + \sigma)X + \left(\frac{\rho}{1+\rho}\right)Y + \sigma XY, \quad (7)$$

$$\frac{d^{\gamma_2} Y}{dt^{\gamma_2}} = \frac{1}{\epsilon}((1 + \sigma)X - Y - \sigma XY), \quad (8)$$

with initial conditions

$$X(0) = 1, Y(0) = 0 \text{ and } 0 < \gamma_i \leq 1, i=1,2.$$

Theorem 1. [14] Consider the fractional order system given below:

$$D^\beta U(t) = F(U), \quad U(0) = U_0 \quad (9)$$

where $0 < \beta \leq 1$ and $u \in R^n$. Equilibrium points of system (9) should be determined by cracking the equation $F(U) = 0$. These points will be locally asymptotically steady if all eigenvalues η matrix of the jacobian $J = \frac{\partial F}{\partial U}$ evaluated at the equilibrium point satisfy:

$$|\arg(\eta)| > \frac{\beta \pi}{2}.$$

The jacobian matrix J system Equations (7) and (8) of the equilibrium point $E = (X^*, Y^*)$

$$J(F^*) = \begin{bmatrix} -1 - \sigma + \sigma Y^* & \frac{\rho}{1+\rho} + \sigma X^* \\ \frac{1}{\epsilon}(1 + \sigma + \sigma Y^*) & \frac{\sigma X^* - 1}{\epsilon} \end{bmatrix}$$

The existence and local stability conditions of this equilibrium point E is as follows. Suppose that $H(P)$ denotes the discriminant of a polynomial P

$$P(\eta) = \eta^2 + b_1 \eta + b_2 = 0$$

where $b_1 = -\text{trace}(J)$, $b_2 = \det(J)$.

$$H(P) = b_1^2 - 4b_2 < 0 \quad \text{or} \quad b_1^2 < 4b_2$$

and $\left| \tan^{-1}(\sqrt{-b_1^2 + 4b_2})/b_1 \right| > \frac{\beta \pi}{2}$

In simple words, stability holds if and only if $b_1 > 0$ and $b_2 > 0$.

Now we evaluate the equilibrium points of the system (7) and (8).

3.1 Equilibrium Point

Equate (7) and (8) equal to zero i.e.

$$-(1 + \sigma)X + \left(\frac{\rho}{1+\rho}\right)Y + \sigma XY = 0 \quad (10)$$

$$\frac{1}{\epsilon}((1 + \sigma)X - Y - \sigma XY) = 0 \quad (11)$$

we obtain $(X^*, Y^*) = (0, 0)$, that is the equilibrium point.

The Jacobian matrix J of system (7) and (8) at the equilibrium point $E(X^*, Y^*) = (0, 0)$ we have

$$J = \begin{bmatrix} -1 - \sigma & \frac{\rho}{1 + \rho} \\ \frac{1}{\epsilon}(1 + \sigma) & -\frac{1}{\epsilon} \end{bmatrix}$$

$$b_1 = -\text{trace}(J) = -(-1 - \sigma - \frac{1}{\epsilon}) > 0, \quad b_2 = \det(J) = \left(\frac{1 + \sigma}{\epsilon(1 + \rho)}\right) > 0.$$

Since $b_1 > 0$ and $b_2 > 0$, so stability holds.

3.2 Numerical Experiments

Numerical experiments are performed using values of parameters given in Table 1.

Table 1. Different parameters & values.

Parameters	Value
ϵ	1
ρ	0.1
σ	0.1

4. NSFD DISCRETIZATION

In this section we shall construct Non Standard Finite Difference Scheme proposed by Mickens [6, 7], for the equations (7) and (8) and swapping the step size h by a function $\psi(h)$ and using GL discretization technique, it can be seen that

$$\sum_{j=0}^{n+1} C_j^{\gamma_1} X^{n+1-j} = \sigma X^n Y^n + \left(\frac{\rho}{1+\rho}\right) Y^n - (1 + \sigma) X^{n+1} \quad (12)$$

$$\sum_{j=0}^{n+1} C_j^{\gamma_2} Y^{n+1-j} = \frac{1}{\epsilon}((1 + \sigma)X^n - Y^{n+1} - \sigma X^{n+1} Y^{n+1}) \quad (13)$$

$$(12) \Rightarrow X^{n+1} = \frac{\sigma X^n Y^n + \left(\frac{\rho}{1+\rho}\right) Y^n - \sum_{j=1}^{n+1} C_j^{\gamma_1} X^{n+1-j}}{(C_0^{\gamma_1} + 1 + \sigma)} \quad (14)$$

$$(13) \Rightarrow Y^{n+1} = \frac{\frac{(1+\sigma)}{\epsilon} X^{n+1} - \sum_{j=1}^{n+1} C_j^{\gamma_2} Y^{n+1-j}}{C_0^{\gamma_2} + \frac{1}{\epsilon}(1 + \sigma X^{n+1})} \quad (15)$$

$$\text{with } C_0^{\gamma_1} = \left(\frac{e^{(1+\sigma)h}-1}{(1+\sigma)}\right)^{-\gamma_1}, \quad C_0^{\gamma_2} = \left(\frac{e^{\frac{1}{\epsilon}h}-1}{\frac{1}{\epsilon}}\right)^{-\gamma_2}$$

4.1 Numerical Experiments

Analytical studies permanently remain unfinished without numerical authentication of the outcomes. In this unit, we present numerical simulation to exemplify the outcomes attained in previous sections. Now we solve the fractional-order Michaelis-Menten biochemical reaction model in two cases. The guestimate elucidations are revealed in Fig. 1-4, for various values of $0 < \gamma_i \leq 1, i = 1, 2$.

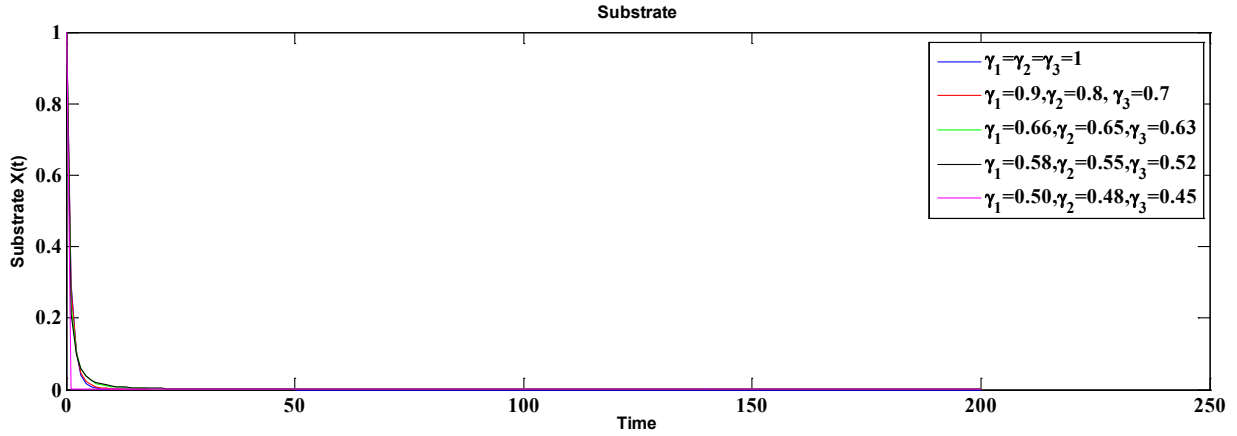


Fig 1. The concentration of Substrate at $N = 200$ with step size $h = 1.1$.

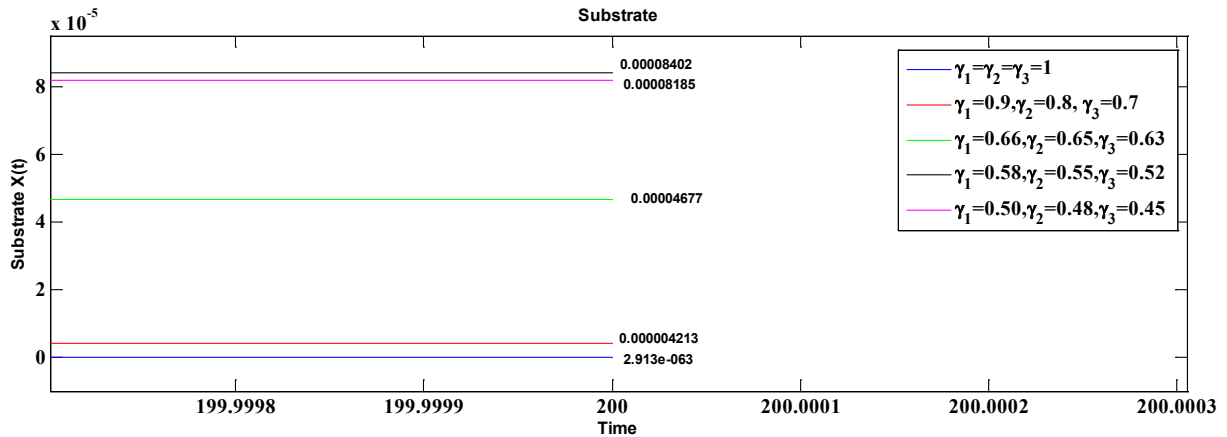


Fig. 1. In zoom.

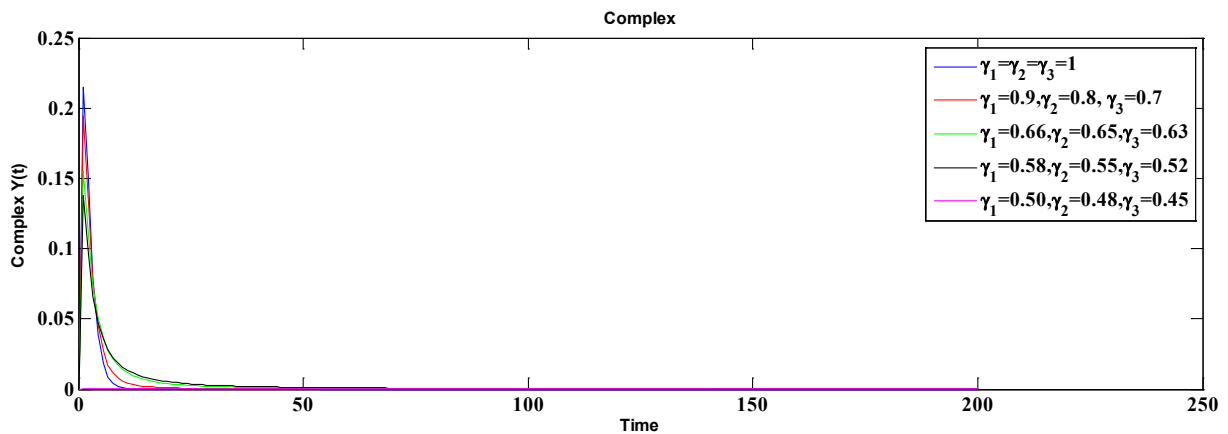


Fig. 2. The concentration of Complex at $N = 200$ with step size $h = 1.1$.

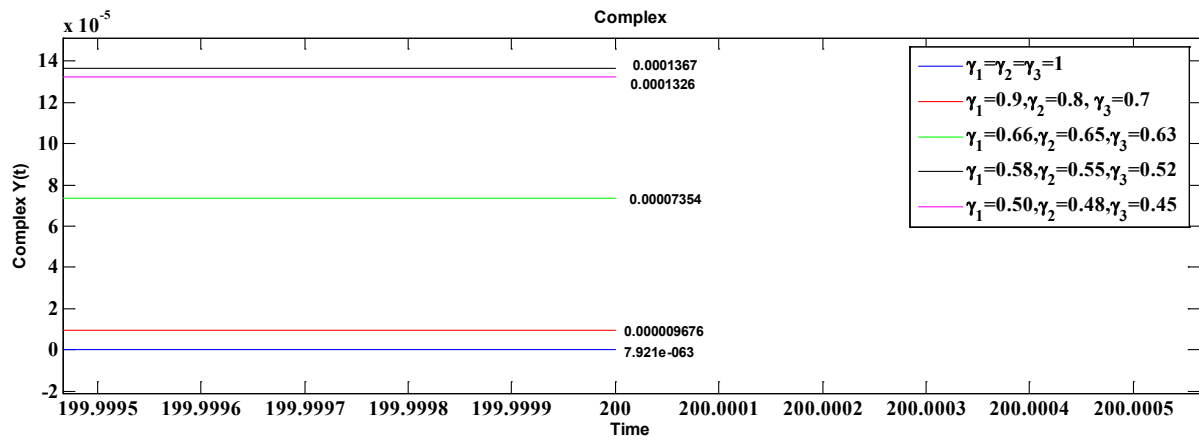


Fig. 2. In Zoom.

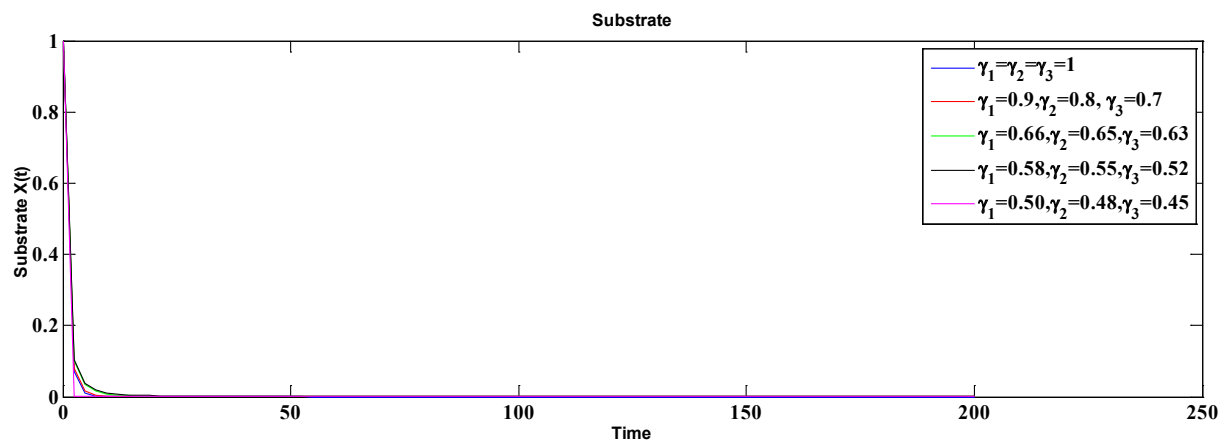
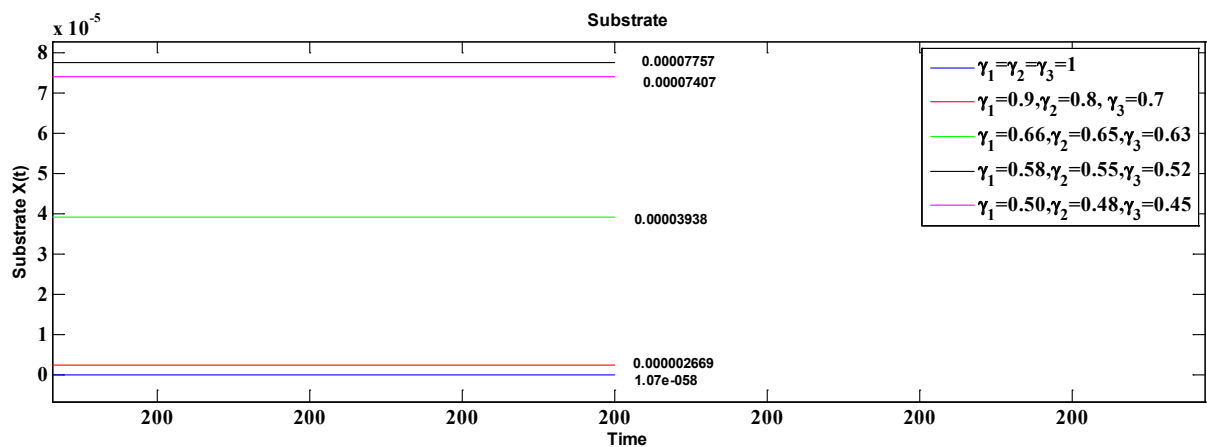
Fig. 3. The concentration of Substrate at $N = 200$ with step size $h = 2.4$.

Fig. 3. In Zoom

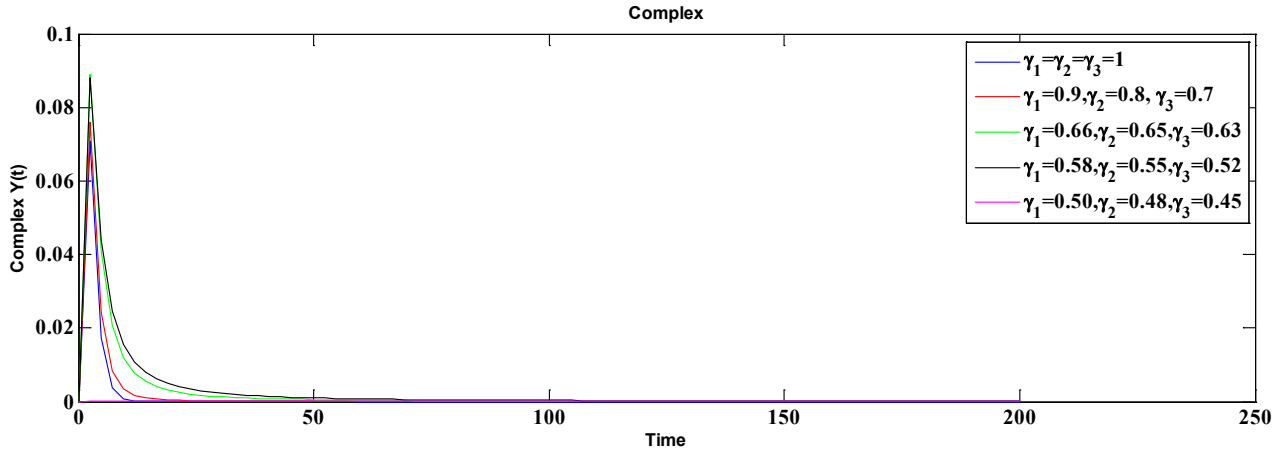


Fig. 4. The concentration of Complex at $N = 200$ with step size $h = 2.4$.

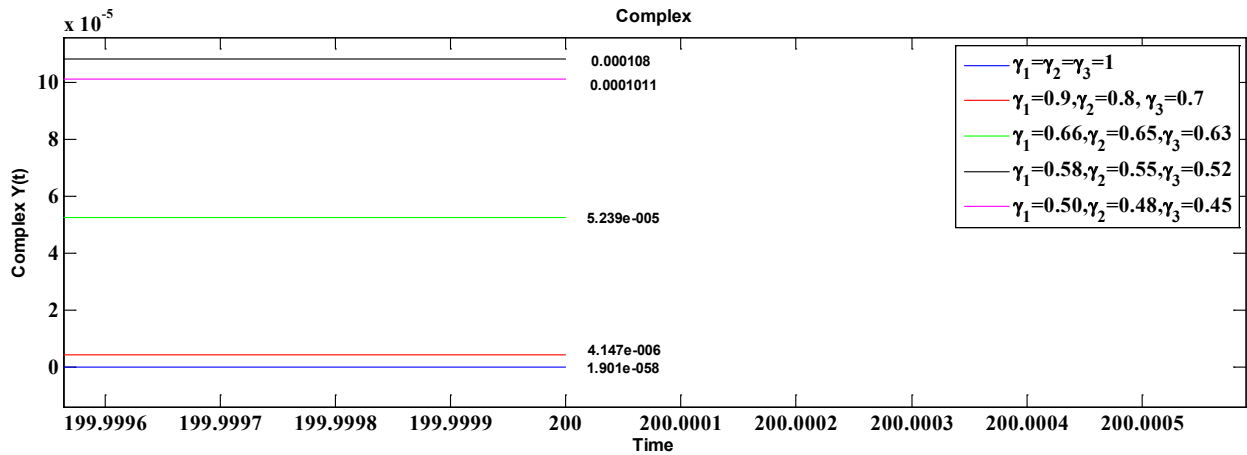


Fig. 4. In Zoom.

5. RESULTS AND DISCUSSION

The Fractional order modelling of well-known Michaelis-Menten non-linear reaction system has been analysed in this paper. An unconditionally convergent non-standard finite difference numerical model with inserting the GL Method, has been constructed for fractional order Michaelis-Menten model. Numerical experiments are performed for different values of fractions.

6. CONCLUSIONS

The present analysis revealed the applicability of the non-standard finite difference technique to crack systems of DEs of fractional order. The work accentuated our faith that the technique is a steadfast method to handle linear and nonlinear fractional order DEs. The goal for considering a fractional order system instead of its integer order counterpart is that fractional order DEs are generalization of integer order differential equations. Also, using fractional order DEs can help us to condense the errors arising from the neglecting parameters in modeling real life phenomenon. The proposed scheme is easy to implement and numerically stable.

7. REFERENCES

1. Maheswari, M.U. & L. Rajendran, Analytical solution of non-linear enzyme reaction equations arising in Mathematical chemistry, *Journal of Mathematical Chemistry* 49: 1713–1726 (2011).
2. Sen, A.K. An application of the Adomian decomposition method to the transient behavior of a model biochemical reaction. *Journal of Mathematical Analysis and Applications* 131(1): 232–245 (1988).
3. Pongsumpun, P. Mathematical model of Dengue disease with incubation period of virus, *World Academy of Science, Engineering and Technology* 44: 328-332 (2008).
4. Rafiq, M., M.O. Ahmed, S. Ahmed, R. Siddique & A. Pervaiz. Some finite difference methods for one dimensional Burgers' Equation for irrotational incompressible flow problem. *Pakistan Journal of Engineering and Applied Sciences* 9: 13-16 (2011).
5. Zafar, Zain Ul Abadin, M.O. Ahmad, Anjum Pervaiz & M. Rafiq. Fourth Order Compact Method for One Dimensional Inhomogeneous Telegraph Equation with $O(h^4, k^3)$. *Pakistan Journal of Engineering and Applied Sciences* 14: 96-101 (2014).
6. Mickens, R.E. Numerical Integration of population models satisfying conservation laws: NSFD methods. *Biological Dynamics* 1(4): 1751-1766 (2007)
7. Mickens, R.E. Dynamical consistency: a fundamental principle for constructing Non-standard finite difference schemes for differential equations. *Journal of Difference Equations and Applications* 13(4): 645-653 (2005).
8. Arafat, A.A.M., S.Z. Rida & H. Mohamed. An Application of the homotopy analysis method to the transient behavior of a biochemical reaction model. *Information Sciences Letters*. 3(1): 29-33 (2014).
9. Edeki, S.O., E.A.Owoloko, A.S. Osheku, A.A. Opanuga, H.I. Okagbue & G.O. Akinlabi. Numerical Solutions of Nonlinear Biochemical model using a Hybrid Analytic Technique. *International Journal of Mathematical Analysis* 9(8): 403-416 (2015).
10. Brauer, F. & C.C. Chavez. *Mathematical Models in Population Biology and Epidemiology*. Springer-Verlag (2001).
11. Hashim, I., M.S.H. Chowdhury & S. Mawa. On multistage homotopy perturbation method applied to non-linear biochemical reaction model. *Chaos Soltion and Fractals* 16:823-827 (2008).
12. Podlubny, I. *Fractional Differential Equations*. Academic Press, New York (1999).
13. Zibaei, S., & M. Namjoo. A nonstandard finite difference scheme for solving Fractional-Order Model of HIV-1 infection of CD4+ T-cells. *Iranian Journal of Mathematical Chemistry* 6(2):169-184 (2015).
14. Ahmad, E., A.M. Atial. El-Sayed & H.A.A. El-Saka, On some Routh-Hurwitz conditions for fractional order differential equations and their applications in Lorenz, Rossler, Chua and Chen systems, *Physics Letters A* 358(1): 1-4(2006).
15. Mickens, R.E., Calculation of denominator functions for nonstandard finite difference schemes for differential equations satisfying a positivity condition. *Numerical Methods of Partial Differential Equations* 23(3): 672-691 (2007).
16. Zafar, Zain Ul Abadin K. Rehan & M. Mushtaq. Fractional-order scheme for bovine baesiosis disease and tickPopulations. *Advances in Difference Equations* 2017:86.
17. Zafar, Zain Ul Abadin K. Rehan, M. Mushtaq & M. Rafiq. Numerical treatment for nonlinear Brusselator chemical model. *Journal of Difference Equations and Applications* 23(3): 521-538 (2017).
18. Zafar, Zain Ul Abadin K. Rehan & M. Mushtaq, HIV/AIDS epidemic fractional-order model, *Journal of Difference Equations and applications* 23(7): 1298-1315 (2017).
19. Zafar, Zain Ul Abadin K. Rehan, M. Mushtaq & M. Rafiq. Numerical modelling for nonlinear biochemical reaction networks. *Iranian Journal of Mathematical Chemistry* (Accepted for publication).



Radiolysis-induced Dosimetric Characterization of Aqueous Solutions of a Synthetic Dye for Gamma Dosimetry

Muhammad Khawar Hayat^{1*}, Ramiza¹, Taqmeem Hussain², Nasim Akhtar³,
Rabia Khaliq¹, and Abdul Hanan Saeed¹

¹Department of Physics, University of Agriculture, Faisalabad 38040, Pakistan

²Department of Physics, Government College University, Faisalabad 38000, Pakistan

³Nuclear Institute of Agriculture and Biology (NIAB), Faisalabad, Pakistan

Abstract: In this study, radiolysis-induced dosimetric response of the alkaline aqueous solutions of Sandalfix Orange C2RL (SO) dye was studied spectrophotometrically. Absorption peak (λ_{\max}) was determined by using a UV/VIS spectrophotometer. Absorbance (A) of the irradiated and un-irradiated sample solutions was measured at this λ_{\max} . Cs^{137} gamma radiation source was utilized for the irradiation of the sample solutions within 0.1-1 kGy and 10-100 kGy dose ranges, i.e., low and high dosimetry, respectively. The absorbance (A) of the sample solutions followed linearly and logarithmically decreasing functions with respect to absorbed dose (D) for low and high dosimetry, respectively. The % discoloration of the sample solutions was found to be increased exponentially with respect to absorbed dose (D) within low dosimetry; while logarithmic increase in %D was observed for high dosimetry.

Keywords: Gamma radiation, dosimetry, color, reactive range 122, absorbance

1. INTRODUCTION

Now-a-days the chances of exposure to ionizing radiation have been increased; Ionizing Radiations (IRs) are capable to produce ions in the subjected substance(s) and cause structural changes into the exposed material(s). The process of calculating the quantity of absorbed dose of IRs is called Radiation Dosimetry (RD). Radiation processing is being controlled by RD; and therefore, is an active search area for scientists. There are many types of dosimeters i.e., thermo-luminescent detectors (TLDs), ionizing chamber dosimeter (IC), fricke dosimeter, film dosimeter and dye dosimeter etc. Chemical dosimeters respond linearly, logarithmically or exponentially etc. upon irradiation (*working principal*) under appropriate conditions [1]. The absorbance (A) of acidic aqueous solutions of Sandalfix Orange C2RL (SO) followed a linearly decreasing function with respect to absorbed dose (D) within low dosimetry range; while logarithmic decrease in absorbance (A) of sample solutions was observed for high dosimetry range [1-2]. Synthetic dyes contain chemicals and have also been used for dosimetric purposes in many forms like aqueous solutions [3-5] and polyvinyl alcoholic films [6-8] etc. In the aqueous solution, irradiation can cause the production of hydrated electron, H_2O_2 , H_2 , OH^- , H^+ and $\bullet\text{OH}$ radical; this formation depends upon the linear energy transfer value of radiation [9]. Researchers have used different colors, i.e., direct yellow 12 [9], alizarin yellow GG [10], 2, 6 dinitro phenol [11] and methyl violet 6B [12], etc. The γ -ray interaction with the dye solutions caused the enhancement of number of H^+ ions in the solutions; resulting an increase in acidity of the sample solutions [5]. Selected dye is relatively cheap and easily available in market. The objective of this study is to check the radiolysis-induced dosimetric response of alkaline aqueous solutions of Sandalfix Orange C2RL (SO) dye within the selected gamma dose range, respectively.

2. MATERIALS AND METHODS

2.1. Pre-irradiation Treatments

SO (Molecular Formula: $C_{31}H_{20}ClN_7Na_4O_{16}S_5$) dye was collected from *Sandal Dyestuff Industries Pvt. Ltd. Faisalabad, Pakistan*; and was used without further purification. 0.5 gram (weighed by Mettler H35AR (USA) balance) of SO dye was dissolved in one liter of deionized water (electrical conductivity less than 1 μ Siemens/cm) collected from *Pakistan Scientific Traders, Faisalabad, Pakistan*, to prepare the aqueous solutions of the dye. The pH of sample solutions was measured by pH meter (Hanna HI 83141); and controlled by using one molar solution of NaOH and HCl, respectively [13]. Sample solutions having pH 8, 9 and 10 were prepared. The prepared solutions were kept in *black box* to avoid the unwanted absorbance of light. A UV-VIS spectrophotometer (Lambda 25 1.27, Perkin Elmer, USA) was utilized for the measurement of absorption peak (λ_{max}) and absorbance (A) of all sample solutions was calculated at this λ_{max} [10]. Cuvettes (path length of 10 mm) were used to keep the solutions in the object beam.

2.2. Post-irradiation Treatments

Gamma radiation source (Cs^{137} with dose rate of 660 Gy/h) available at *Nuclear Institute of Agriculture and Biology (NIAB), Faisalabad, Pakistan*, was utilized for irradiation of the sample solutions. Glass ampoules (internal diameter = 1.03 cm and thickness = 0.18 cm) with fit in ground stopper were used to keep the solutions in gamma radiation source for predetermined interval of time. The irradiation process was categorized in two different phases, i.e., 0.1-1 kGy (low dosimetry) and 10-100 kGy (high dosimetry), respectively. Figure 1 illustrates the molecular structure of SO dye.

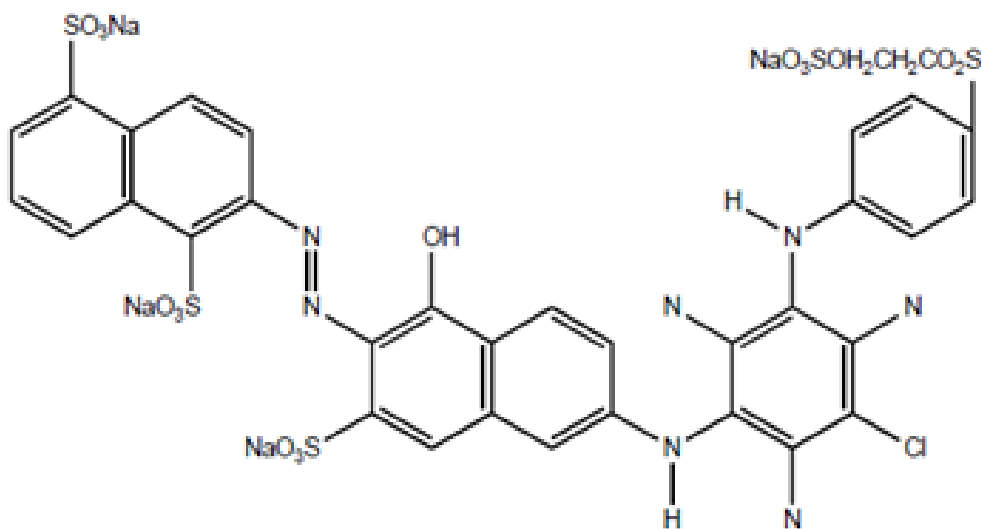


Fig. 1. Molecular structure of SO dye.

3. RESULTS AND DISCUSSION

The response curves were plotted for absorbance (A) versus absorbed dose (D) and % discoloration against absorbed dose (D) for the sample solutions of SO dye.

$$A_8 = -0.0008 \times D + 2.8232 \quad R^2 = 0.4 \quad (1)$$

$$A_9 = -0.0006 \times D + 2.7407 \quad R^2 = 0.4 \quad (2)$$

$$A_{10} = -0.0006 \times D + 2.8295 \quad R^2 = 0.3 \quad (3)$$

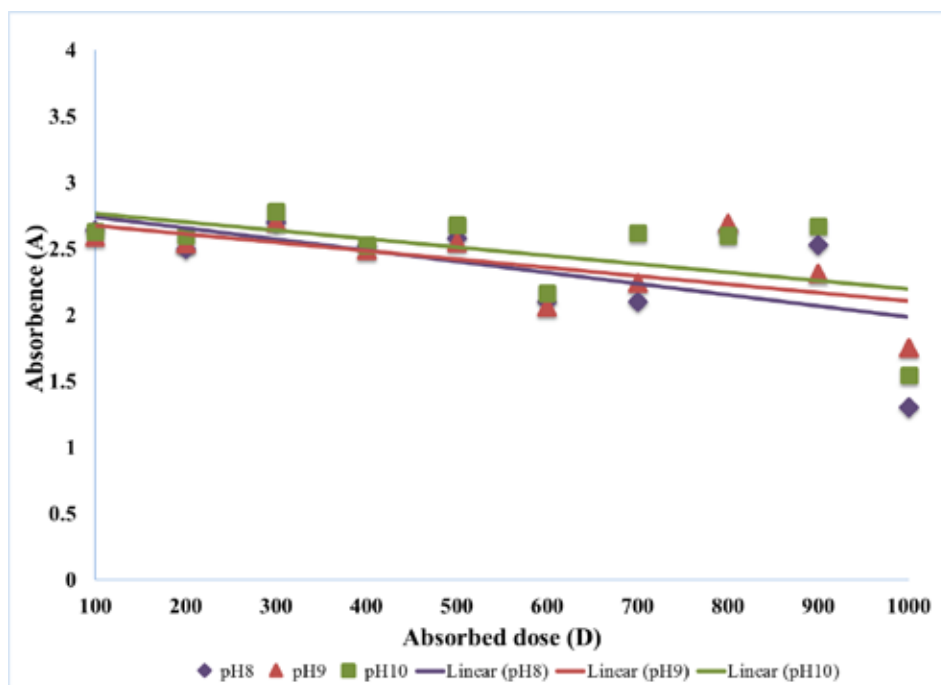


Fig. 2. Absorbance of SO dye dose for low dosimetry.

Where, A_8 , A_9 and A_{10} represent the absorbance (A) of the sample solutions having pH 8, 9 and 10, respectively. Equations 1-3 show the regression models along with correlation coefficients (R^2) for the absorbance (A) versus absorbed dose (D) within low dosimetry range. The absorbance (A) of sample solutions follows a linearly decreasing function with respect to absorbed dose (D) within low dosimetry.

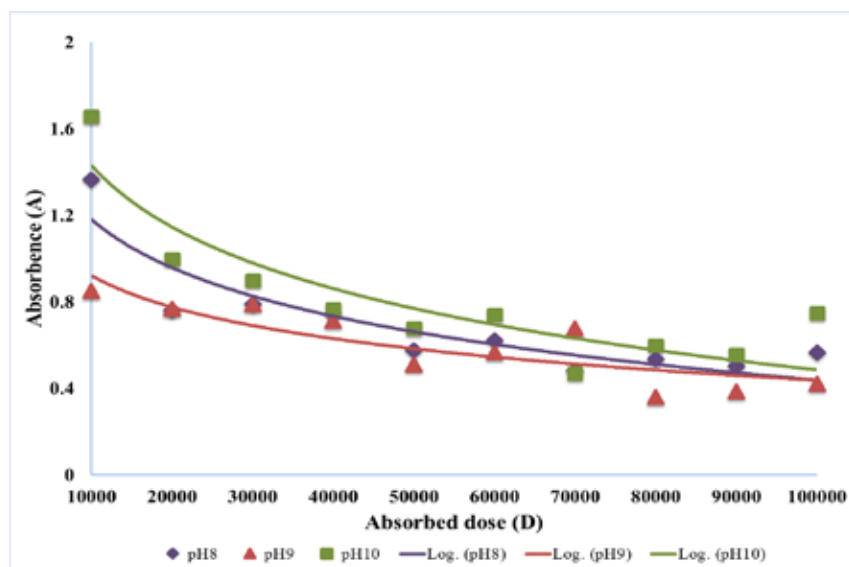


Fig. 3. Absorbance of SO dye versus absorbed dose for high dosimetry.

$$A_8 = -0.323 \times \ln(D) + 4.1547 \quad R^2 = 0.8 \quad (4)$$

$$A_9 = -0.21 \times \ln(D) + 2.8577 \quad R^2 = 0.7 \quad (5)$$

$$A_{10} = -0.411 \times \ln(D) + 5.2124 \quad R^2 = 0.8 \quad (6)$$

Where, A_8 , A_9 and A_{10} show the absorbance (A) of the sample solutions having pH 8, 9 & 10, respectively. Equations 4-6 show the regression models along with R^2 . The absorbance (A) of the sample solutions of SO dye decreases logarithmically with respect to absorbed dose (D) within high dosimetry range.

The % discoloration of the aqueous solutions of SO dye can be calculated in terms of absorbance (A) of the sample solutions at pre and post irradiations stages as given in equation 7 [3,10].

$$\%D = [(A_o - A_i) / A_o] \times 100 \quad (7)$$

Where, A_o is the absorbance of the pre-irradiated sample solutions and " A_i " is the absorbance of the post-irradiated sample solutions.

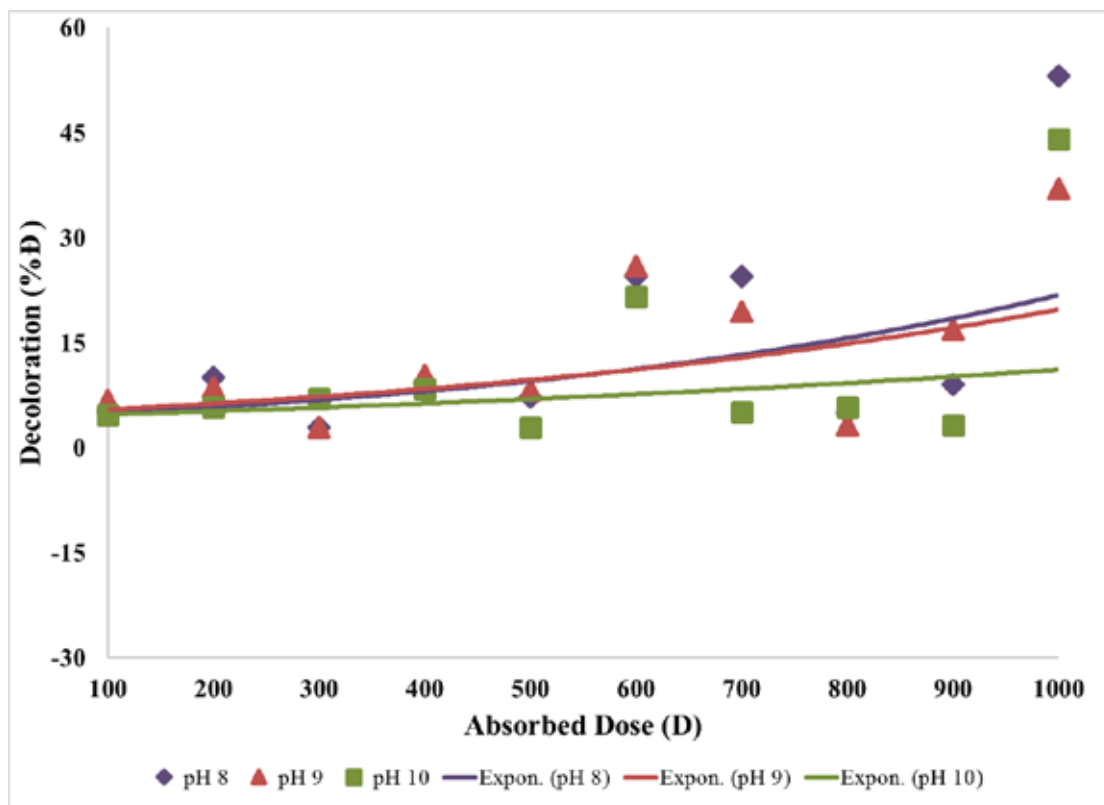


Fig. 4. Discoloration of SO dye versus absorbed dose for low dosimetry.

$$\%D_8 = 4.1652 \times e^{0.0017 \times D} \quad (8)$$

$$\%D_9 = 4.7543 \times e^{0.0014 \times D} \quad (9)$$

$$\%D_{10} = 4.3313 \times e^{0.0009 \times D} \quad (10)$$

Where, $\%D_8$, $\%D_9$ and $\%D_{10}$ represent the % discoloration (%D) of the samples having pH 8, 9 and 10, respectively. Equations 8-10 show the regression models for low dosimetry. The %D is found to increase exponentially with respect to absorbed dose (D) within low dosimetry.

$$\%D_8 = 11.612 \times \ln(D) - 49.449 \quad R^2 = 0.8 \quad (11)$$

$$\%D_9 = 7.5617 \times \ln(D) - 2.7936 \quad R^2 = 0.7 \quad (12)$$

$$\%D_{10} = 14.877 \times \ln(D) - 88.855 \quad R^2 = 0.8 \quad (13)$$

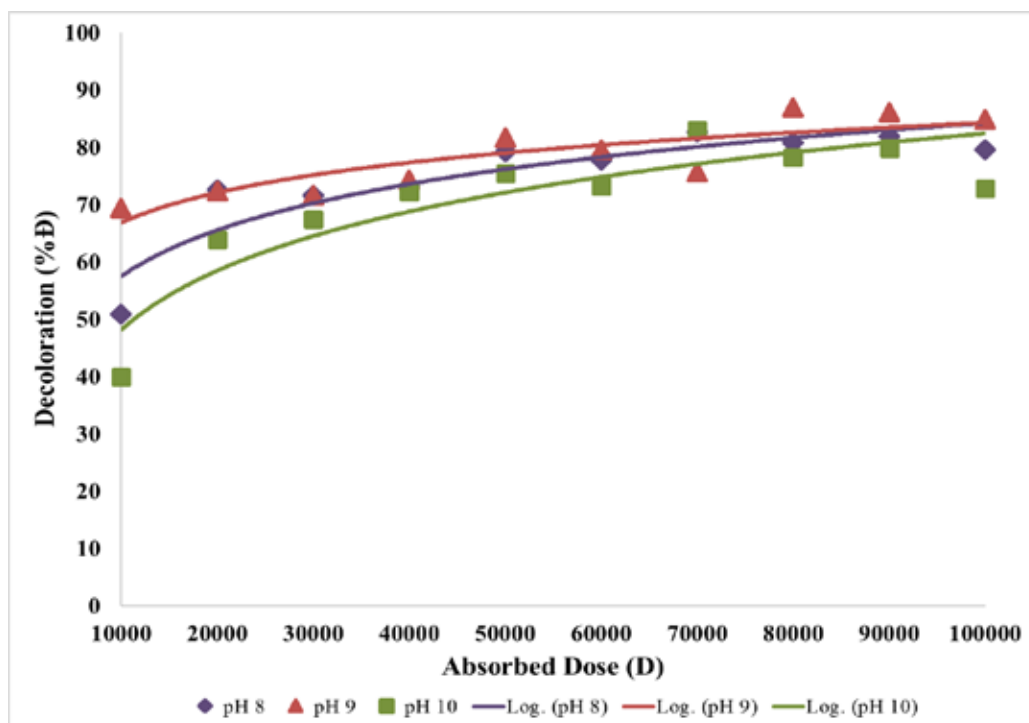


Fig. 5. Decoloration of SO dye versus absorbed dose for high dosimetry.

The % decoloration of the sample solutions having pH 8, 9 and 10 is indicated by $\%D_8$, $\%D_9$ and $\%D_{10}$, respectively. Equations 11-13 show the regression models along with R^2 values and explain the logarithmic increase in $\%D$ with respect to absorbed dose (D) within high dosimetry.

4. CONCOLUSIONS

The absorbance (A) of the alkaline aqueous solutions of *Sandalfix Orange C2RL* (SO) dye follows a linearly decreasing function against absorbed dose (D) for low dosimetry while logarithmic decrease in absorbance (A) of the sample solutions is observed within high dosimetry range. The % decoloration of the sample solutions was increased exponentially and logarithmically with respect to absorbed dose (D) for low and high dosimetry, respectively. The alkaline sample solutions of SO dye exhibited a good dosimetric response upon irradiation within the selected dose ranges. However, additional studies are warranted to check the response of SO dye within intermediate dosimetry, i.e., 1-10 kGy.

5. ACKNOWLEDGEMENTS

Special thanks to the Director of Nuclear Institute for Agriculture and Biology (NIAB), Faisalabad, Pakistan, for providing the irradiation facility.

6. REFERENCES

- Hayat, M.K., Ramiza, T. Hussain, A.H. Saeed, I. Haq & N. Akhtar. Preliminary studies for dosimetric response of a synthetic dye for gamma dosimetry. *Journal of Basic and Applied Sciences* 12: 406-410 (2016).
- Hayat, M.K., Ramiza, T. Hussain, A.H. Saeed, I. Haq & N. Akhtar. Effect of gamma radiation on the mean absorbance of a synthetic dye in aqueous solutions and its possible use in gamma dosimetry. *Journal of Chemical, Biological and Physical Sciences* 7(1): 56-61 (2017).

3. Hayat, M.K., Ramiza, T. Hussain, R. Khaliq, H. Farooq, I. Haq & N. Akhtar. A study of percentage discoloration of aqueous solutions of a synthetic dye for gamma dosimetry. *International Journal of Scientific and Engineering Research* 8(1): 1437-1439 (2017).
4. Hussain, T., M.Y. Hussain, M. Shahbaz, Inam-ul-Haq, H. Farooq & S. Ali. Radiolysis of commercial dyes in aqueous solutions to produce dosimeters for gamma dosimetry. *Journal of Basic and Applied Sciences* 8: 315-318 (2012).
5. Hussain, T., F. Akhtar, Inam-ul-Haq, I. Toqeer & H. Farooq. Usability of aqueous solutions of commercial reactive dye for gamma dosimetry. *Academic Research International* 5(1): 32-36 (2014).
6. Akhtar, S., T. Hussain, A. Shahzad, Qamar-ul-Islam, M.Y. Hussain & N. Akhtar. Radiation induced discoloration of reactive dye in PVA films for film dosimetry. *Journal of Basic and Applied Sciences* 9: 416-419 (2013).
7. Antar, E.M. Effect of γ -ray on optical characteristics of dyed PVA films. *Journal of Radiation Research and Applied Sciences* 7: 129-134 (2014).
8. Eid, S., S. Ebraheem & N.M. Abdel-Kader. Study the effect of gamma radiation on the optical energy gap of poly (vinyl alcohol) based ferrotitanium alloy film: Its possible use in radiation dosimetry. *Open Journal of Polymer Chemistry* 4: 21-30 (2014).
9. Batool, J., S.A. Shahid, Ramiza, N. Akhtar, A. Naz, M. Yaseen, I. Ullah, M. Nadeem & I. Shakir. A study on dosimetric characterization of direct yellow 12 dye at high radiation γ -dose. *Bulletin of the Korean Chemical Society* 33(7): 2265-2268 (2012).
10. Sun, W., L. Chen, J. Tian, J. Wang & S. He. 2013. Degradation of a monoazo dye alizarin yellow GG in aqueous solutions by gamma irradiation: Decolorization and biodegradability enhancement. *Radiation Physics and Chemistry* 83: 86-89 (2013).
11. Gafar, S.M. & M.A. El-Ahdal. Dosimetric characteristics of 2, 6 di-nitro phenol for high dose dosimetry. *Dyes and Pigments* 109: 67-71 (2014).
12. Bhaisare, K.D. & D.V. Parwate. A comparative study on gamma radiolytic and oxidative degradation of aqueous solution of methyl violet 6B. *International Journal of Innovative Research in Science, Engineering and Technology* 3(1): 8287-8294 (2014).
13. Hussain, T., M. A. K. Shahid, M. Shahbaz, Inam-ul-Haq & H. Farooq. Gamma radiation effect on commercial reactive dye in the range 0-100 kGy using the idea of discoloration factor and extinction coefficient. *Journal of Basic and Applied Sciences* 8: 581-584 (2012).



Magnetotelluric Data Analysis using Swift Skew, Bahr Skew, Polar Diagram, and Phase Tensor: a Case Study in Yellowstone, US

Erick Pranata^{1*}, Selvi Misnia Irawati¹, and Sintia Windhi Niasari²

¹Geophysics Study Program, Universitas Gadjah Mada, Sekip Utara BLS 21,
Yogyakarta 55281, Indonesia

²Geophysics Laboratory, Universitas Gadjah Mada, Sekip Utara BLS 21,
Yogyakarta 55281, Indonesia

Abstract: Magnetotelluric (MT) method is a passive electromagnetic (EM) technique for measuring fluctuations of the nature electric (E) and magnetic (B) fields at the Earth surface, which correspond to apparent resistivity. Prior to MT data modeling, to convert apparent resistivity to true resistivity, analyzing the dimensionality of MT data is needed. In this study, the MT data were taken from US Array in Cascadia Subduction Zone, particularly around the Yellowstone National Park, US. The MT data analysis used four parameters, *i.e.*, Swift skew, Bahr skew, polar diagram, and phase tensor. Additionally, 1D modeling for XY and YX components was performed. Thus, correlations between the model and the dimensionality data in the study areas were revealed. Data analysis from Swift skew parameter indicated the 3D character of MT data (*i.e.*, Swift skew value more than 0.3). The majority of the polar diagrams were peanut shaped, and a lot of phase tensors had an ellipse shape with large β value, indicating 3D character. Although 3D inversion modeling for these data was more proper (because the data exhibited 3D character) than 1D inversion, the 3D inversion algorithm was computationally expensive. Thus, in this study, we performed 1D inversion MT modeling which revealed that in some cases, 1D and 3D inversion results exhibited similarities.

Keywords: Bahr skew, dimensionality, magnetotellurics, phase tensor, polar diagram, swift skew

1. INTRODUCTION

Activity in MT method divided onto five stages, *i.e.*, data acquisition, data processing, data analysis, modeling, and interpretation. In this study, stage three was emphasized because data analysis affects the modeling result. The model of MT can be ambiguous if the dimensionality data are different from the dimensionality model. Thus, MT data analysis can reduce the ambiguity model. In this study, 11 MT data sites at Yellowstone area were used. These are located in Idaho State and Wyoming State, North America. In the west of North America, there is a subducting plate named Juan de Fuca, which is a part of Pacific microplate and is considered as one of the smallest plates on earth. It moves toward North America plate and subducts below that plate. In their research, Xue and Allen [1] mapped the Juan de Fuca plate with seismic. It shows that Juan de Fuca plate disappears at 400 km to the east from the western coast. The plate discontinues when it reaches Yellowstone area.

The four components in 1D modeling have a different result when it begins to model the 3D data area. If they have the same trend of response, these components are valid and can be interpreted. But if each of them has different trend of responses, only some of them are valid and can be interpreted or none of them is valid.

From the 3D model [2], YX components is the most similar response from three other components at (12 to 14) km and (31 to 37) km depth. However, YX component does not have as much similarity to other components than XY components. YX component is used as a reference due to the similarity with 3D modeling.

2. METHODS

Eleven MT data sites at Yellowstone area were used. These are located in Idaho State and Wyoming State, North America (Fig.1). MT data have impedance parameter [3] consisting of several components that represent the dimensionality. In this study, Swift skew, Bahr skew, and polar diagram were used to determine the dimensionality of MT data. Moreover, we use phase tensor to determine the geoelectrical strike.

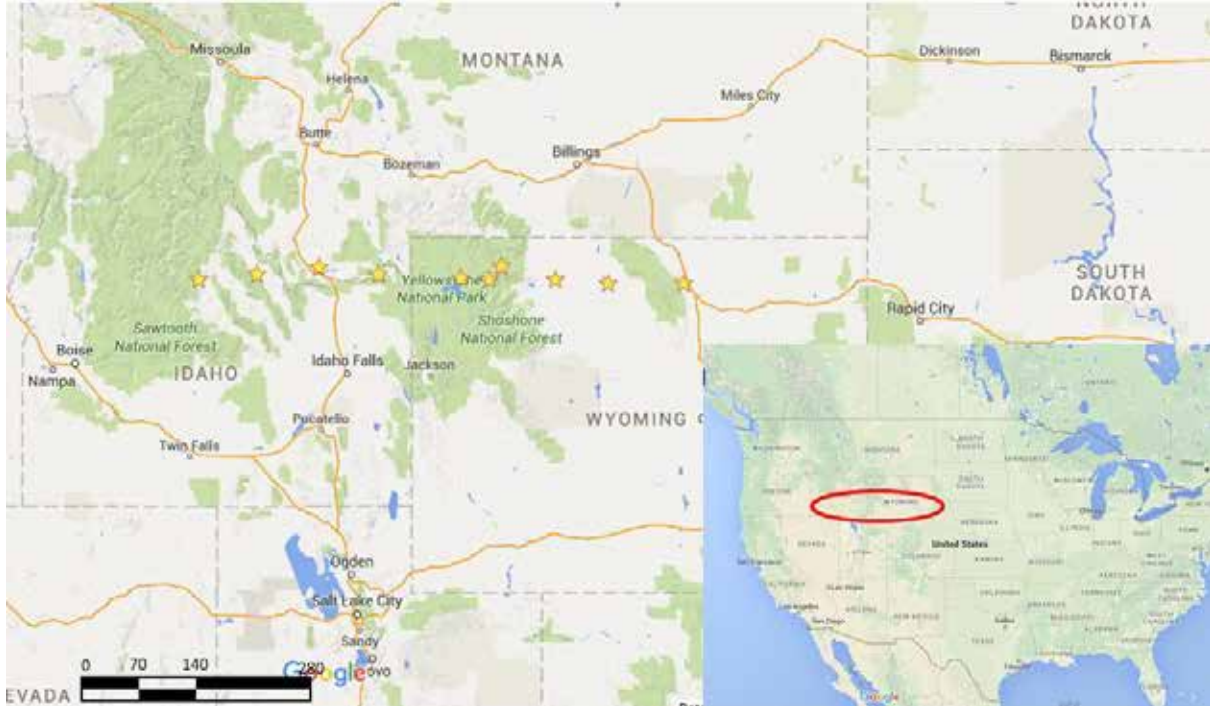


Fig. 1. Yellow stars denote MT sites. Four MT sites are located in Idaho state and six others are in Wyoming state. The space between locations is about 70 km. Inset: The study area location is marked by red ellipse.

Skew is one of dimensionality data MT analysis [4]. Swift skew is a ratio of diagonal components (Z_{xx} and Z_{yy}) to the off-diagonal components (Z_{xy} and Z_{yx}) [5]. If the value of $Skew_{Swift} > 0.3$, it has 3D character. If $Skew_{Swift} < 0.3$, the data has 1D or 2D character [6].

$$Skew_{Swift} = \left| \frac{Z_{xx} + Z_{yy}}{Z_{xy} - Z_{yx}} \right| \quad (1)$$

Bahr skew is known as phase-sensitive or regional skew [7]. If $Skew_{Bahr} < 0.1$, it indicates 1D or 2D character. If $0.1 > Skew_{Bahr} > 0.3$, indicates 2D or 3D character of MT data. If $Skew_{Bahr} > 0.3$, it indicates 3D character of MT data.

$$Skew_{Bahr} = \frac{\sqrt{|Im(Z_{xy}Z_{yy}^* + Z_{xx}Z_{yx}^*)|}}{|Z_{xy} - Z_{yx}|} \quad (2)$$

Polar diagram is one of dimensionality data MT analysis that has not structural or frequency limitations [7]. If polar diagram drawn as a circle, it shows 1D character. The polar diagram ellipse-shape indicates 2D character while the peanut-shape represent a 3D character.

$$|Z_{xy}(\gamma)| = \left| Z_{yx} \left(\gamma + \frac{\pi}{2} \right) \right| = |Z_1 + Z_3 \cos 2\gamma - Z_4 \sin 2\gamma| \quad (3)$$

Phase tensor is a ratio of real and imaginary part of impedance tensor [8]. If the phase tensor is acircle and small β , the conductivity structure is 1D [9]. If phase tensor is drawn as an ellipse with small β , it has 2D character. If the phase tensor is drawn as an ellipse with large β value, it belongs to the 3D characteristic of MT data.

$$\phi = X^{-1}Y \quad \text{and} \quad \beta = \frac{1}{2} \tan^{-1} \left(\frac{\phi_{xy} - \phi_{yx}}{\phi_{xx} + \phi_{yy}} \right) \quad (4)$$

The 3D data in straight line in North America are processed with 1D software. The 1D Software uses the Bostick algorithm which in turn uses resistivity in a period function to get resistivity in depth function [10]. Ten magnetotellurics location is used for this research. The locations were in North America in Idaho state and Wyoming state. The distance between one data location to another was about 70 km. There are only six from the east are inside the Yellowstone area.

The data chosen visualize the geology of Yellowstone in resistivity. With four data outside the Yellowstone area and six inside, it will visualize the area that is affected by Yellowstone. The purpose of using ip2win is because everyone does not have the 3D processing software. From each magnetotelluric component, a resistivity model will be obtained. Not all components are reliable because it is in 1D. By using the 1D software, this paper reveals the advantages and disadvantages of using 1D software for 3D data.

The modeling process with ip2win is to make the model as close as possible to the data. The quality control is the RMS value. To decide how many layers, depends on how many gradients the data have. If only one gradient then the layer should be two (1 gradient +1). If two gradient then there must be three layers.

3. RESULTS AND DISCUSSION

Based on MT data analysis using four parameters, i.e. Swift skew, Bahr skew, polar diagram, and phase tensor, we can determine the dimensionality of the data. In this discussion, we explain the dimensionality of MT data for each parameter.

Swift skew is simply calculation from impedance tensor. Due to the calculation, most of the data have Swift skew value more than 0.3 (blue dots on Fig. 2) which indicates 3D character of MT data.

Bahr skew is modern skew calculation using impedance tensor. From the calculation, MT data dominated with the Bahr skew value 0.1 to 0.3 (orange dots on Fig. 2). That value indicates 2D or 3D character of MT data.

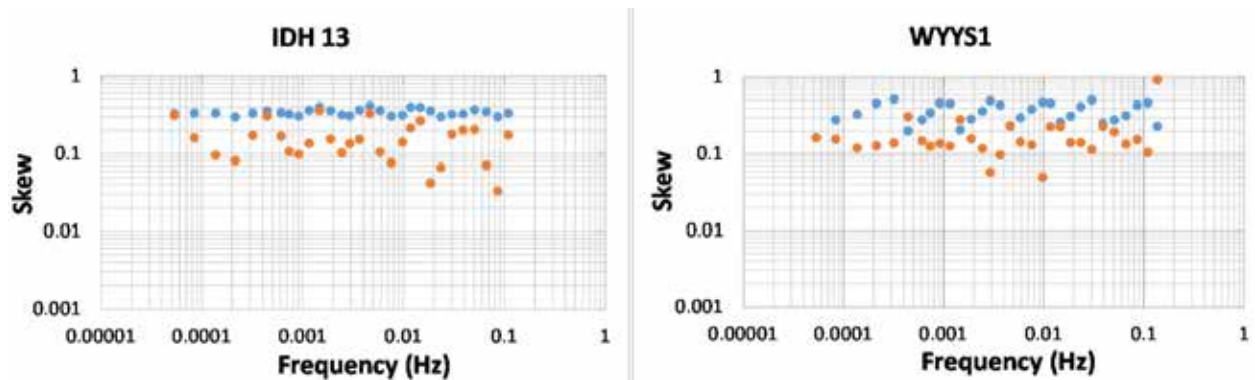


Fig. 2. Swift skew (denoted by blue dots) and Bahr skew (denoted by orange dots). a) IDH13 b) WYYS1 Swift skew dominated with value > 0.3 that indicated 3D data MT. Bahr skew had values 0.1 to 0.3, indicating 2D or 3D data.

Due to skew analysis (Swift and Bahr), this MT data has two possible dimensionality, 2D or 3D. Therefore, further data analysis using polar diagram and phase tensor parameters is needed to obtain more accurate dimensionality of MT data.

Polar diagram can determine the dimensionality of MT data. For resistive materials, major axis of the polar diagram is perpendicular to the strike direction. Meanwhile, on conductive medium, major axis of the polar diagram is parallel to the strike [7].

Polar diagram was drawn in Fig 3. Polar diagram dominated by peanut shape. That shape indicates 3D MT data. However, at sites IDH13, WYH19, and WYH20 have ellipse polar diagram which indicates 2D MT data. It happens at high frequency (> 0.0664 Hz).

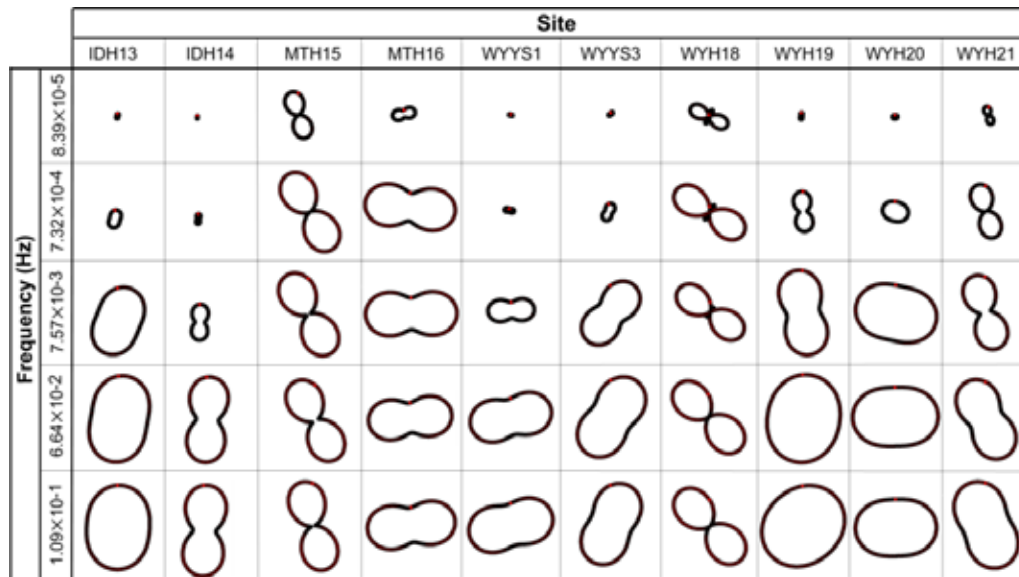


Fig. 3. Polar diagram of MT data. It was dominated by peanut shape which indicated 3D MT data. Therefore, 3D modeling inversion were proper to these data.

Based on geological condition, these sites are in different lithology margin. Thus, it affects the dimensionality of MT data. Therefore, polar diagram shape from high frequency and low frequency of these sites had different dimensionalities.

Phase tensor is one of data analysis parameter [7]. Phase tensor can be illustrated as circle or ellipse [8]. Major axis of phase tensor represents the geoelectrical strike [11]. Phase tensor shape for certain periods described the lateral conductivity structure changes. This changes showed different ellipticity phase tensor for each period (Fig 4).

In this data, phase tensor is dominated by the ellipse shape. Furthermore, β values of the phase tensor are high ($\beta > 3^\circ$ and $\beta < -3^\circ$). This indicates 3D MT data.

From the data analysis using four parameters (Swift skew, Bahr skew, polar diagram, and phase tensor), MT data in Yellowstone area reveal 3D character. Thus, if the data are 3D then 1D modeling is improper. Furthermore, MT data are important to get lower ambiguity model due to incorrect data characterization.

From this 3D layer model (Fig. 5), the majority of the data have high resistivity. In a deeper zone (284 – 341) km, the data has lower resistivity than the higher. The 3D data represent all four components merging together. The deeper zone can be interpreted as earth mantle that has lower resistivity than earth crust.

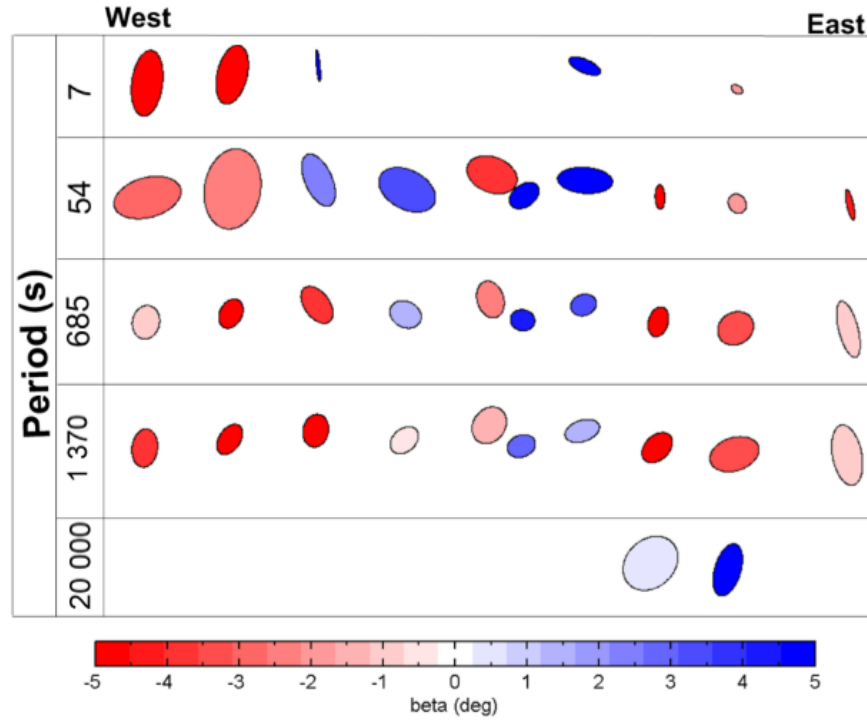
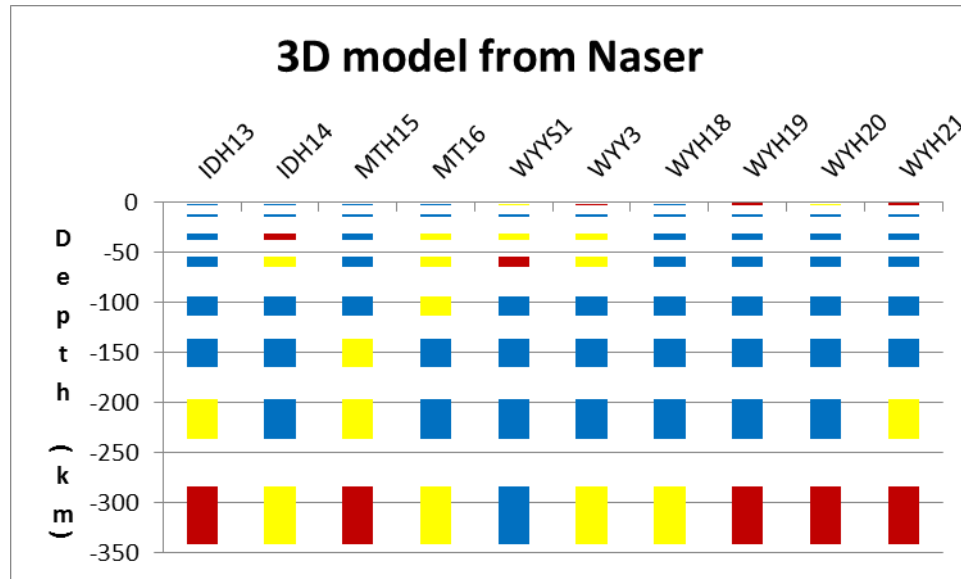


Fig. 4. Phase tensor for each period. It was drawn as an ellipse and has high β value, *i.e.*, $> 3^\circ$ and $< -3^\circ$. That indicated the 3D MT data. Therefore, 3D modeling was proper to these data.



Color scale in Ωm

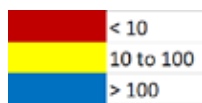
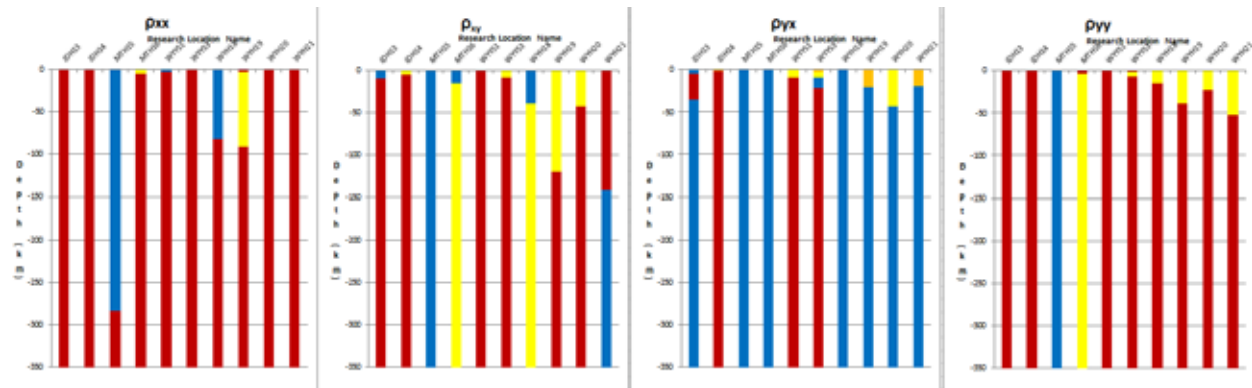


Fig. 5. Reconstruction of 3D model, reconstructed from Meqbel et al. layered model [2]. Depth 1.1 to 1.5 km, 12 to 14 km, 31 to 37 km, 54 to 65 km, 94 to 113 km, 136 to 164 km, 197 to 236 km, and 284 to 341 km. Majority of the data had high resistivity value.



Color scale in Ωm

Fig. 6. 1D ρ apparent modeling at research location; from west to east, depth in km. From left to right: IDH13, IDH14, MTH15, MTH16, WYS1, WYYS3, WYH18, WYH19, WYH20, and WYH21. a) ρ_{xx} ; b) ρ_{xy} ; c) ρ_{yx} d) ρ_{yy} each component has 350 km depth. YX component was used as reference to resemble other components.

From Fig. 6, YX component had the most resemblance with 3D model than three other components; the resemblance was 38 out of 80 (about 47.5 %). The RMS error from XX component is 10.577 %, XY component is 6.072 %, YX component is 5.176 %, and YY component is 10.158 %. From the RMS error, YX model is the most similar to its data. From both RMS and manual resemblance, the most relevant model synchronizing with 3D model is the YX component. In this area, YX component has the most similarity with the 3D data. It can be used as a standard to model 3D data with 1D software in Yellowstone.

With YX as a reference, it has 29.52 % of resemblance with another component. The similarity result is obtained by matching the resistivity from each component subjectively. The total similarity is 62 out of 210 (about 29.52 %). In this area, YX component is used as a reference although XY component has more similarity with other component is because YX component is most similar to the 3D model.

4. CONCLUSIONS

In the Yellowstone area of USA which has majority 3D data proved with the skew, polar diagrams and phase tensor can be modeled with 1D software. The 1D component that is the most representable is YX component; however, the similarity between 1D inversion of YX component and 3D inversion is 47.5 %. The YX component has 29.52 % similarity with other three components but the XY component has 37.61 % similarity. The YX is picked due to the most relevance with the 3D model.

5. ACKNOWLEDGEMENTS

Special thanks to A. Schultz, G.D. Egbert, A., T. Peery, V. Clote, B. Fry, S. Erofeeva and staff of the National Geoelectromagnetic Facility. The authors thank Universitas Gadjah Mada for funding this research. The authors also thank Atria, Rakhmat, Adytya, Halim, Afta, Rachmat, and Dina for their help and support by way of reviews, suggestions and comments.

6. REFERENCES

1. Xue, M. & R.M. Allen. The fate of the Juan de Fuca plate: Implications for a Yellowstone plume head. *Earth and Planetary Science Letters* 264: 266–276 (2007).
2. Meqbel, N.M., G.D. Egbert, P.E. Wannamaker, A. Kelbert & A. Schultz. Deep electrical resistivity structure of the northwestern U.S. derived from 3-D inversion of US Array magnetotelluric data. *Earth and Planetary Science Letters* 402: 290–304 (2014).
3. Jiracek, G.R. *The Magnetotelluric Method*. San Diego State University, San Diego, CA, USA, p. 11–12 (2004).

4. Vozoff, K. Magnetotellurics: Principles and practice. *Earth and Planet Science* 99: 441–471 (1990).
5. Swift, C.M.A. *Magnetotelluric Investigation of an Electrical Conductivity Anomaly in the Southwestern United States*. [PhD thesis, Massachusetts Institute of Technology, MA, USA (1967).
6. Hoffmann-Rothe, A., O. Ritter & C. Janssen. Correlation of electrical conductivity and structural damage at a major strike-slip fault in Northern Chile, *Journal of Geophysical Research* 109: B10101 (2004).
7. Berdichevsky, M.N. & V.I. Dmitriev. *Models and Methods of Magnetotellurics*. Springer, Berlin, Germany, p. 31–33 (2008).
8. Caldwell, T.G., H.M. Bibby & C. Brown. The magnetotelluric phase tensor. *Geophysical Journal International* 158: 457–469 (2004).
9. Booker, J.R. *The Magnetotelluric Phase Tensor: A Critical Review*. Springer, Berlin, p. 7–40 (2013).
10. Rodi, W. & R.L. Mackie, Nonlinear conjugate gradients algorithm for 2D magnetotelluric inversion. *Geophysics* 66: 174–187 (2001).
11. Hill, G.J. Distribution of melt beneath mount St Helens and mount Adams inferred from magnetotelluric data. *Nature Geoscience Letters* 2: 785–790 (2009).



Characterization of CO₂ Laser Photoacoustic Spectrometer Intracavity Configuration and Its Application in Measuring Acetone Gas in Human Breath

Mitrayana^{1*}, Nurul Muyasaroh¹, Mohammad Ali Joko Wasono¹,
and Mohammad Robikhul Ikhsan²

¹Physics Department, Faculty of Mathematics and Natural Science, Universitas Gadjah Mada, Sekip Utara, Bulaksumur, Yogyakarta 55281, Indonesia

²Internal Medicine Ward, RSUP Dr. Sardjito, Faculty of Medicine, Universitas Gadjah Mada, Jalan Kesehatan, Kabupaten Sleman, Yogyakarta 55281, Indonesia

Abstract: Photoacoustic spectrometer is a very effective instrument for detecting low concentration gasses. In this research, a CO₂ laser photoacoustic spectrometer intracavity configuration was characterized and applied for measuring acetone gas concentration in human exhaled breath during exercise on a treadmill. The characterization included laser power optimization, scanning laser spectrum, making resonant curve and quality factor, measuring noise and background signal, determining lowest detection and linearity curve. Acetone gas concentration was determined by analyzing normalized photoacoustic signal using multicomponent matrix. The optimum power was obtained at 32.4 ± 0.5 W and CO₂ laser spectrum consisted of four line groups. The highest laser absorption line of standard acetone gas was determined at 10P20. Quality factor was obtained at 14.6 ± 0.6 , noise at 1.7 ± 0.2 $\mu\text{V}/\text{Hz}^{1/2}$, background signal at 10P20 0.001 to 0.004 mV, lowest detection limit of acetone gas at 110 ± 14 ppbV, and acetone gas linearity gradient on 10P20 was at $k_{22} = 0.0140 \pm 0.0007$. Acetone gas concentration in human exhaled breath after exercising on treadmill decreased from 43 % to 79 % than before.

Keywords: Acetone gas concentration, exercise, intracavity configuration CO₂ laser photoacoustic spectrometer, treadmill

1. INTRODUCTION

Photoacoustic spectrometer (PAS) is a very effective instrument for detecting trace gasses at low concentrations. For the detection of sample gas, PAS is based on energy resonance between radiation source and excitation energy of gaseous molecule. Photoacoustic spectrometer had been applied in all research fields [1–4]. Schramm et al. [1] succeeded in detection of the NO₂, N₂O, and SO₂ gases from diesel machines exhaust by using PAS. Schilt et al. [2] also used PAS to monitor the ammonia amount in the semiconductor industrial area. Huber et al. [3] succeeded in developing the CO₂-Sensor for Automotive Applications by following the photoacoustic principle. Popa and Petrus [4] used CO₂ laser PAS to investigate the effect of heavy metals on plants by detecting the emitted ethylene and ammonia gas.

A sample is placed at photoacoustic cell, radiated by laser radiation of which the intensity is modulated on photoacoustic cell resonance frequency. The gaseous molecule absorbs laser radiation energy and it is excited to a higher state. The excited state loses its energy by collisions. The collisions between molecules cause the increasing kinetic energy, and then it causes the increase in temperature. And the increase in temperature causes the increase in pressure. Because the intensity of laser radiation is

modulated, the pressure fluctuates. The fluctuation of pressure causes the acoustics which can be detected using microphone [5].

In this research, a CO₂ laser photoacoustic spectrometer intracavity configuration had been characterized and applied for measuring acetone gas concentration of human exhaled breath during exercise on treadmill. CO₂ laser is radiation source which radiates infrared beam at the wavelength area of 9.2 μm to 10.8 μm where there is more than 250 molecular gasses of environmental concern with atmospheric, medical and scientific spheres exhibiting strong absorption bands [6].

Acetone gas is a diabetes mellitus biomarker [7, 8]. Patients' pancreas with diabetes mellitus can not produce quite insulin to absorb glucose produced by food, whereas high blood glucose level causes the formation of acetone gas [9]. Diabetes mellitus can be diminished by exercises such as walking on the treadmill [10].

2. MATERIALS AND METHODS

The photoacoustic spectrometer characterizations include laser power optimization, scanning laser spectrum, making resonant curve and quality factor, measuring noise and background signal, determining lowest detection and linearity curve (Fig. 1).

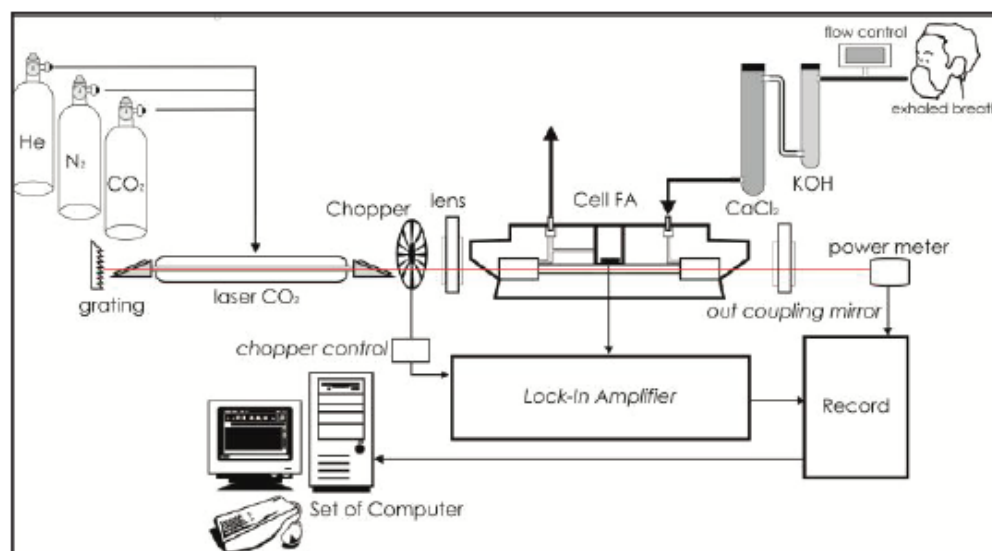


Fig. 1. The CO₂ laser photoacoustic spectrometer intracavity configuration scheme.

Measuring of acetone gas concentration of human exhaled breath during exercise on treadmill began by taking the volunteer breath and saving it in a sample bag through KOH and CaCl₂ scrubber. A scrubber was used as the CO₂ and H₂O absorber. Volunteer breath was taken five times, before exercise (decision to- 1), after warming up (decision to- 2), after conditioning (decision to- 3), after cooling down (decision to- 4) and 5 min after exercise (decision to- 5) (see Fig. 8 and Fig. 9).

- Warming up: walking on the treadmill 1.2 km h⁻¹ for 5 min.
- Conditioning: walking on the treadmill 2.4 km h⁻¹ for 20 min.
- Cooling down: walking on the treadmill 1.2 km h⁻¹ for 5 min.

Volunteer breath was flowed into a photoacoustic spectrometer for detecting and producing photoacoustic signal. Since the photoacoustic signal is proportional to laser power, it must be normalized.

The normalized photoacoustic signal is a fluctuating time function needed to choose the constant average region. Acetone gas concentration was determined by analyzing normalized photoacoustic signal using a multicomponent matrix as shown in Equation (1).

$$(S_n)_i = \sum_{j=1}^3 k_{ij} C_j, (i = 1, 2, 3) \quad (1)$$

where C_j is gas concentration, $(S_n)_i$ is normalized photoacoustic signal at highest absorption laser line, k_{ij} is a calibration factor.

Acetone gas concentration after (C_i) and before (C_o) exercising on the treadmill was compared using Equation (2).

$$\Delta C = \frac{C_o - C_i}{C_o} \times 100 \% \quad (2)$$

where ΔC is the acetone gas concentration difference. The acetone gas concentration of human breath with and without exercises on the treadmill was compared.

3. RESULTS AND DISCUSSION

3.1. The Characterization of CO₂ Laser Photoacoustic Spectrometer Intracavity Configuration

In this research, CO₂ laser was operated at 8.32 kV to 9.04 kV and 11.93 mA to 12.84 mA, because at this voltage and this current, laser can produce lasing easily. The optimum power was obtained at (32.4 ± 0.5) W and CO₂ laser spectrum consisted of four line groups, as shown in Fig. 2.

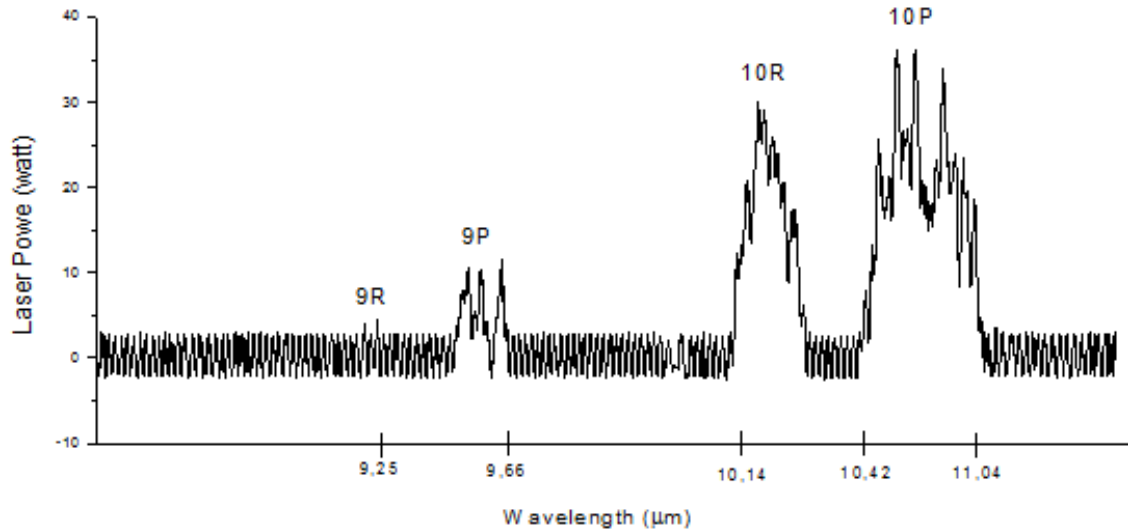


Fig. 2. CO₂ laser spectrum.

The optimum power can be obtained by optics aligning. Grating, laser tube, chopper, photoacoustic cell and outcoupling mirror was aligned. He, N₂ and CO₂ flow scale were arranged at 30, 70 and 50. Optic component must be cleaned to obtain the optimum power because the dust on optic component surface can interfere laser propagation.

Photoacoustic cell was designed as resonator to amplify the photoacoustic signal. Resonance curve of acetone gas is shown in Fig. 3. The resonance frequency was obtained at $f_{\text{res}} = (1650 \pm 5)$ Hz and the bandwidth, at $f_{\text{res}} = (113 \pm 5)$ Hz. Chopper was arranged at this frequency, so that laser radiation can be

resonated with the sample in photoacoustic cell. Quality factor (Q) can be obtained using Equation (3). Quality factor was obtained at 14.6 ± 0.6 .

$$Q = \frac{f_{res}}{\Delta f} \quad (3)$$

where Δf is resonance curve bandwidth when the signal is the $1/\sqrt{2}$ x maximum signal.

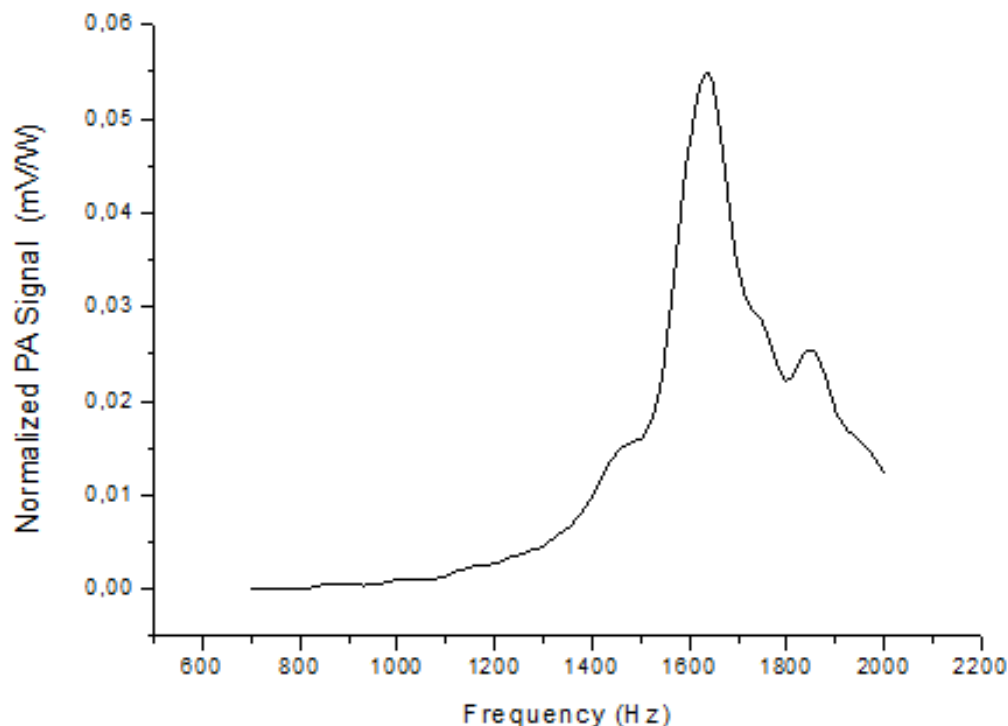


Fig. 3. Resonance curve of acetone gas.

The highest laser absorption line of standard acetone gas, standard ethylene gas, standard ammonia gas were known using the absorption spectrum of each gas. Every gas absorbs a laser line or more and resonants at a specific laser line. Absorption spectrum of acetone gas is shown in Fig. 4. The highest laser absorption line of the standard acetone gas was determined at 10P20.

Signals which interferes photoacoustic signal are noise and background signals. The noise is caused by acoustical and electrical vibrations. The noise was obtained at $1.7 \pm 0.2 \mu\text{V}/\text{Hz}^{1/2}$. It is used to determine the lowest detection limit. The noise of photoacoustic spectrometer is shown in Fig. 5.

The background signal was measured before measuring the photoacoustic signal. The example of the background signal measured at the laser line 10P20 is shown in Fig. 6. The background signal at 10P20 was 0.001 mV to 0.004 mV.

System sensitiveness of photoacoustic spectroscopy is determined by the lowest detection limit given by:

$$BDT = \frac{C}{(S_n / N)} \quad (4)$$

where C is acetone gas concentration, S_n is normalized photoacoustic signal, and N is noise. The lowest detection limit of acetone gas was 110 ± 14 ppbV.

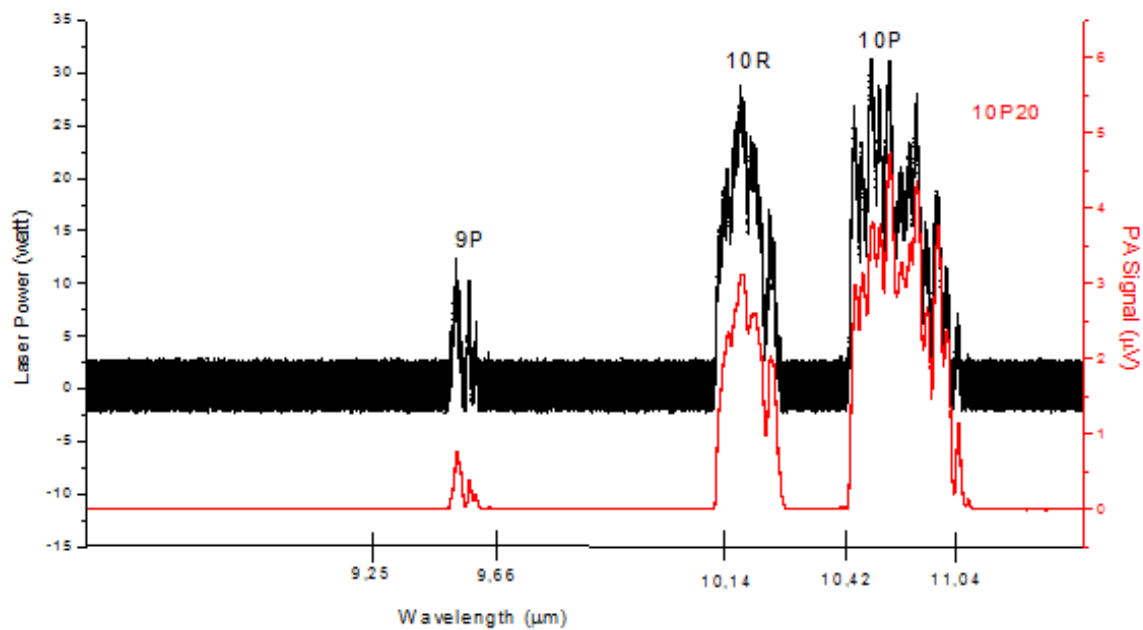


Fig. 4. Absorption spectrum of acetone gas.

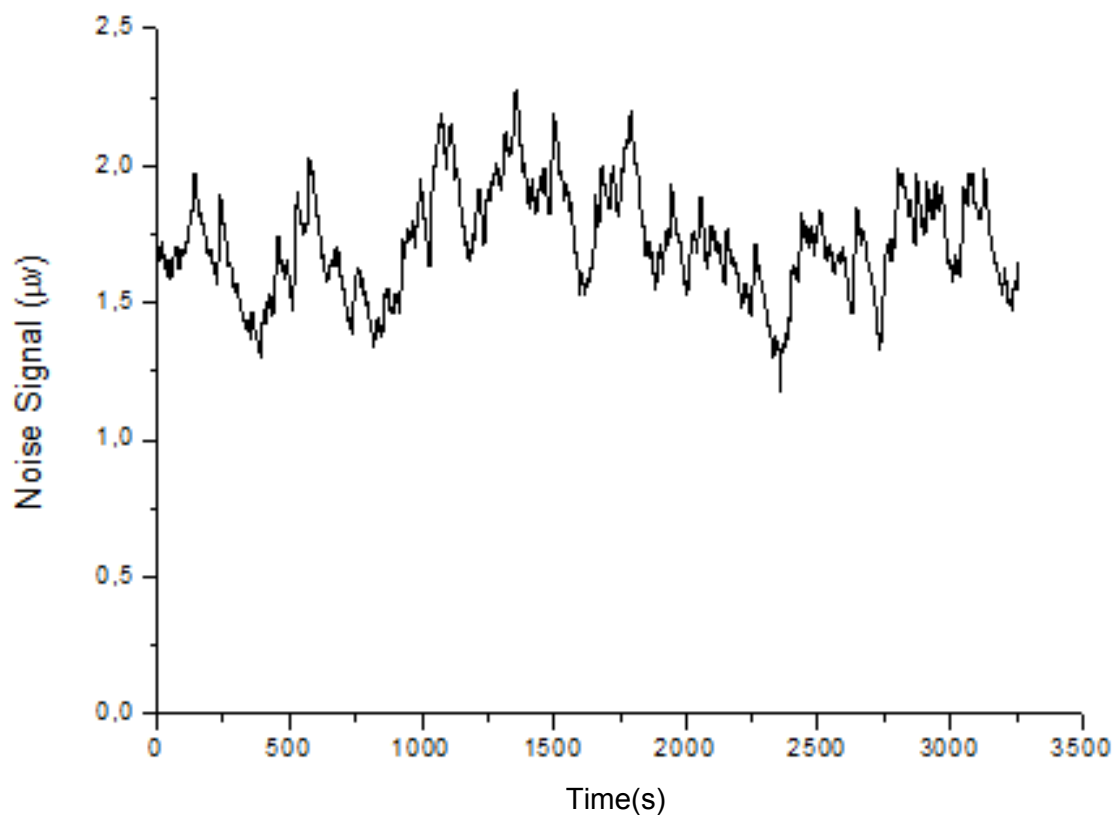


Fig. 5. Noise of photoacoustic spectrometer.

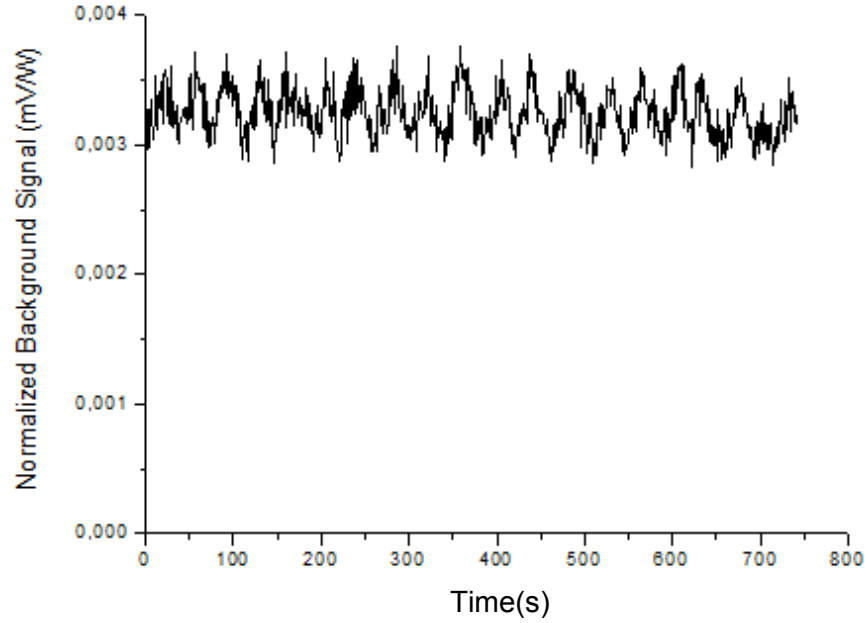


Fig. 6. Background signal.

The correlation between gas concentration and photoacoustic signal is determined by the calibration factor using multicomponent analysis, an analysis of sample that consists of more than one gases. Gases used in this research are ethylene, acetone and ammonia. Analysis was done by measuring the photoacoustic signal of each gas at each laser line where the highest absorption occurred. It is shown in gas absorption spectrum that the highest absorption line of acetone gas was determined at 10P20, ethylene gas at 10P14, and ammonia gas at 10R14. Every gas was broken up into some concentrations. The correlation between the gas concentration and the photoacoustic signal was drawn as a linearity curve.

Linearity curve of acetone gas at laser line 10P20 is shown in Fig. 7. The acetone gas linearity gradient was $k_{22} = 0.0140 \pm 0.0007$. The correlation factor of this linearity was $R^2 = 0.98807$. Gradient is a calibration factor, the correlation between gas concentration and photoacoustic signal. The gradient of each linearity curve is used as a matrix component of the multicomponent analysis as shown in Equation (5).

$$\begin{pmatrix} (S_n)_1 \\ (S_n)_2 \\ (S_n)_3 \end{pmatrix} = \begin{pmatrix} 0.029 & 0.00115 & 0.00110 \\ 0.012 & 0.0140 & 0.0120 \\ 0.00051 & 0.00019 & 0.025 \end{pmatrix} \begin{pmatrix} C_1 \\ C_2 \\ C_3 \end{pmatrix} \quad (5)$$

Gas concentration was determined by matrix inverse given by:

$$\begin{pmatrix} C_1 \\ C_2 \\ C_3 \end{pmatrix} = \begin{pmatrix} 35.010339 & -2.7477681 & -0.2130922 \\ -29.351669 & 74.235621 & -35.059278 \\ -0.4710460 & -0.5454753 & 40.774024 \end{pmatrix} \begin{pmatrix} (S_n)_1 \\ (S_n)_2 \\ (S_n)_3 \end{pmatrix} \quad (6)$$

Hence, ethylene, acetone and ammonia gas concentration become:

$$\begin{aligned} C_1 &= 35.010339(S_n)_1 - 2.7477681(S_n)_2 - 0.2130922(S_n)_3 \\ C_2 &= -29.351669(S_n)_1 + 74.235621(S_n)_2 - 35.059278(S_n)_3 \\ C_3 &= -0.4710460(S_n)_1 - 0.5454753(S_n)_2 + 40.774024(S_n)_3 \end{aligned} \quad (7)$$

where C_1 , C_2 dan C_3 respectively are ethylene, acetone and ammonia gas concentrations. $(S_n)_1$, $(S_n)_2$ and $(S_n)_3$ respectively are normalized photoacoustic signals at laser lines 10P14, 10P20 and 10R14.

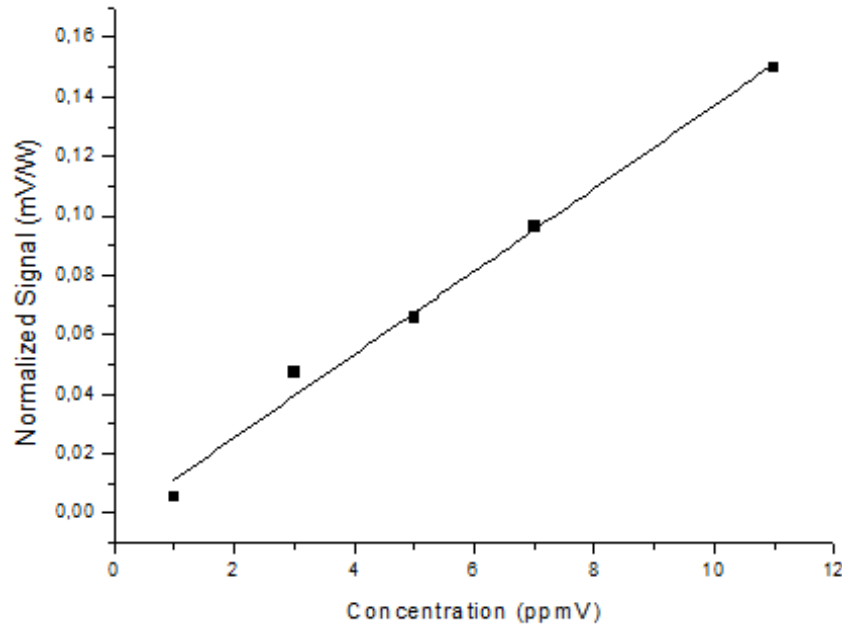


Fig. 7. Linearity curve of acetone gas at laser line 10P20.

3.2. Measuring Acetone Gas Concentration of Human Breath During Exercise on a Treadmill

An acetone gas concentration graph of human exhaled breath during exercise on treadmill is shown in Fig. 8.

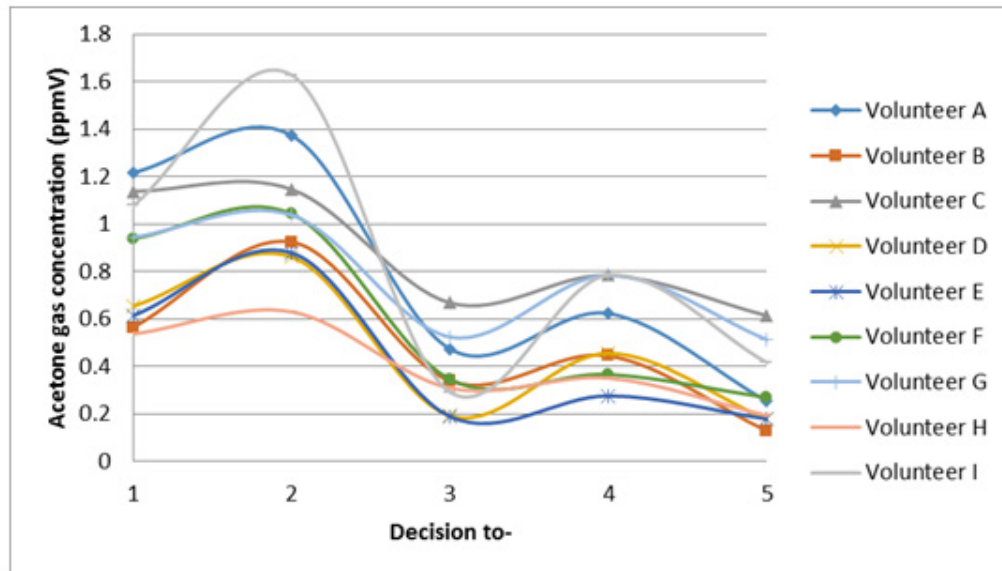


Fig. 8. Acetone gas concentration graph of human exhaled breath during exercise on a treadmill.

The acetone gas concentration graph of human exhaled breath during exercise on treadmill is compared with the acetone gas concentration graph of human exhaled breath without any activity as shown in Fig. 9.

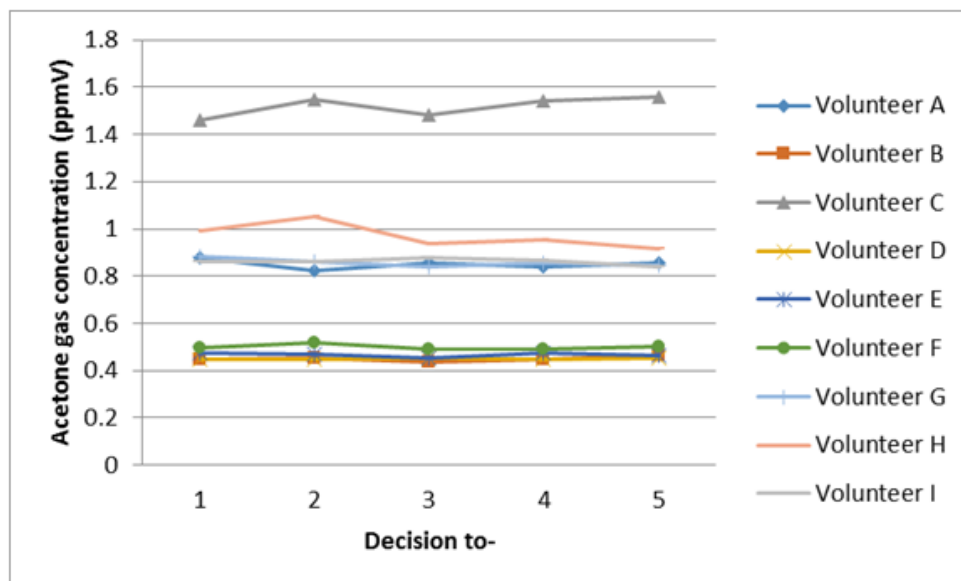


Fig. 9. Acetone gas concentration in exhaled breath of humans doing no activity.

Acetone gas concentration of human exhaled breath during exercise on treadmill is more fluctuative than that without any activity because the acetone gas concentration is interfered by the blood glucose level. The blood glucose level can be interfered by exercises. As shown in Fig. 8, after warming up, the acetone gas concentration is higher than before exercises. Warming up was done 5 min, exercising less than 20 min causes the liver to release the blood glucose that is saved as fuel. The increase in the acetone gas concentration is supposed to be caused by the blood glucose released, so it indicates a high signal when being detected. After conditioning, the acetone gas concentration drastically decreases, it is lower than the concentration before exercises. Conditioning was done for 20 min, exercising 20 min, or if it is more than 20 min it may cause the muscles to take the blood glucose for fuel and it decreases the blood glucose totality [5]. After cooling down, the acetone gas concentration increases again, causing the liver to release the blood glucose again. Amount 5 min after exercises, the acetone gas concentration is lower than that before exercises. The acetone gas concentration of human exhaled breath after exercising on treadmill decreased at 43 % to 79 % than before. It is in line with the hypothesis that acetone gas concentration of human exhaled breath after exercising on treadmill decreases than before because exercises can reduce the blood glucose level.

4. CONCLUSIONS

The lowest detection limit for acetone gas from the built photoacoustic spectrometer was 110 ± 14 ppbV. The system detected acetone gas from the volunteer breath during exercise on a treadmill using laser CO₂ photoacoustic spectrometer. The acetone gas concentration in human exhaled breath after exercising on a treadmill decreased from 43 % to 79 % compared with concentration in the prior to exercise breath.

5. REFERENCES

- Schramm D.U., M.S. Stel, M.G. Silva, L.O. Carneiro, A.J.S.A. Junior & H.Vargas. Application of laser photoacoustic spectroscopy for the analysis of gas samples emitted by diesel engines. *Infrared Physics and Technology* 44:263–269 (2002).
- Schilt, S., L. Thévenaz, M. Niklès, L. Emmenegger & C. Hügli. Ammonia monitoring at trace level using photoacoustic spectroscopy in industrial and environmental applications. *Spectrochimica Acta. Part A* 60:3259–3268 (2003).

3. Huber, J., C. Weber, A. Eberhardt & J. Wöllenstein. Photoacoustic CO₂-sensor for automotive applications. In: *Proceedings of the 30th Anniversary Eurosensors Conference – Eurosensors 2016*. Bársony, I., Z. Zsolt & B. Gábor (Ed.). *Procedia Engineering* 168: 3–6 (2016).
4. Popa, C. & P. Mioara. Heavy metals impact at plants using photoacoustic spectroscopy technology with tunable CO₂ laser in the quantification of gaseous molecules. *Microchemical Journal* 134: 390–399 (2017).
5. Harren, F.J.M., G. Cotti, J. Oomens & S.L. Hekkert. Photoacoustic spectroscopy in trace gas monitoring. In: *Encyclopedia of Analytical Chemistry*. Meyer, R.A. (Ed.), John Wiley and Sons, Chichester, p. 2203–2226 (2000).
6. Ivascu, I.R., C.E. Matei, M. Patachia, A.M. Bratu & D.C. Dumitras. CO₂ laser photoacoustic measurements of ethanol absorption coefficients within infrared region of 9.2–10.8 μm . *Spectrochimica Acta. Part A: Molecular and Biomolecular Spectroscopy* 163: 115–119 (2016).
7. Wang, C. & P. Sahay. Breath analysis using laser spectroscopic techniques: Breath biomarkers, spectral fingerprints, and detection limits. *Sensors* 9(10): 8230–8262 (2009).
8. Miekisch, W. & J.K. Schubert. From highly sophisticated analytical techniques to life-saving diagnostics: Technical developments in breath analysis. *Trends in Analytical Chemistry* 25(7): 665–673 (2006).
9. Nayak, S. Influence of aerobic treadmill exercise on blood glucose homeostasis in noninsulin dependent diabetes mellitus patients. *Indian Journal of Clinical Biochemistry* 20(1): 47–51 (2005).
10. Goldoni, M., M. Corradi, P. Mozzoni, G. Folesani, R. Alinovi, S. Pinelli, et al. Concentration of exhaled breath condensate biomarkers after fractionated collection based on exhaled CO₂ signal. *Journal of Breath Research* 7(1): 017101 (2013).



Efficiency Enhancement of Banana Peel for Waste Water Treatment through Chemical Adsorption

Atif Khan^{1*}, Hassan Jived Naqvi², Shabana Afzal³, Shaista Jabeen¹,
Misbah Iqbal¹, and Iram Riaz¹

¹Department of Chemical and Polymer Engineering, University of Engineering and Technology
Lahore (Faisalabad Campus), Pakistan

² Department of Chemical Engineering, University of Engineering and Technology,
Lahore, Pakistan

³ Department of Chemical Engineering, MNS University of Engineering and Technology,
Multan, Pakistan

Abstract: Many types of agricultural wastes are now being studied for waste water treatment because of their adsorbing properties. For instance, banana peels are capable of adsorbing various metals and other pollutants present in industrial waste waters, provided the peels are pretreated with proper surface-active agents. This manuscript reports an investigation regarding activation of banana peels for this purpose. Banana peels were treated with dilute solutions of oxalic acid, sulfuric acid and sodium hydroxide at room temperature for 24 hours followed by drying at 90°C. The adsorbing properties of banana peels were studied by using Fourier's transform infrared spectroscopy (FT-IR). It was observed that FT-IR is a quick and simple technique to verify the surface activation of banana peels.

Keywords: Banana peels, surface activation, chemical adsorption, concentration, Fourier transform infrared spectroscopy (FT-IR)

1. INTRODUCTION

Treatment of contaminated water from various sources is a challenge for engineers and scientists [1, 2]. Different technologies were introduced for waste water treatment like membrane separation, chemical and physical treatment but further research is required to overcome the problem of waste water treatment for proper disposal [3, 4]. Among various methodologies of treating waste water the sorption is the quite effective technique. Reasons of gaining attention towards this technique are its availability, low cost and versatility [5]. Researches have shown that various adsorbents can be used for the waste water treatment but the banana peels are the most popular adsorbent because of its availability and simple processing and satisfactory results [6]. Banana peels can remove wide variety

of contaminants from waste water like oil spills, biological waste, carcinogenic elements, heavy metals and various dyes in water from textile and other sources [7].

The adsorption involves a surface adhesion phenomenon. In adsorption process if some biological material is used as an adsorbent then process is known as bio-sorption. This process involves solid and liquid phase interaction [8]. Due to this interaction of sorbent and sorbate exchange the ions and remove unwanted dissolved species. Higher affinity of sorbent to sorbate species, unwanted ions in sorbate are attracted to sorbent ions. Solid and liquid phase distribution in sorption process is very important for determining the effectiveness of the process and degree of sorbent affinity plays a key role in this aspect [9, 10]. The

sorption process is preferred over conventional treatment methods because of its low cost, easy sorbent availability and regeneration and minimum biological sludge production. Many researchers have reported the use of different adsorbents for waste water treatment, waste oil treatment, etc. [11, 12] investigated the sorbent properties of walnut shell and Naqvi et al. [13, 14] investigated the sorption properties of bentonite clay for waste lube oil treatment.

In this study banana peels were studied by analyzing its sorbent properties through simple testing technique. Chemical treatment enhanced properties of banana peels. The main objective in this research is to activate the surface of banana peels for enhancing the sorption properties by various chemicals like sodium hydroxide, sulfuric acid and oxalic acid [15, 16]. These chemicals modified the properties of banana peel in such a way that its sorption properties were increased and can be used in sorbent applications. Testing technique for sorption properties of banana peels were analyzed by Fourier's transform infrared spectroscopy (FT-IR) [17, 18].

2. MATERIALS AND METHODS

Banana peels samples were collected from kitchen waste. These peels were first washed with distilled water and then were dried at room temperature for 24 hours. Preparation of bio-sorbent is a critical step for enhancing the properties of banana peels. To this end, the banana peels were dried in a dryer for 24 hours at 90 °C. After drying, the banana peels were ground to average 200 mesh size in a coffee grinder. After grinding, banana peels' powder was once again dried in a tray dryer for 24 hours to ensure the removal of moisture [19, 20]. After drying, samples of banana peel were treated with sodium hydroxide, sulfuric acid and oxalic acid separately. The main parameters taken into consideration for sorbent preparation were concentration and residence time. According to the literature, the concentration varies from 0.5 *N* to 2 *N* solution of sodium hydroxide, 1 *N* to 3 *N* solution of sulfuric acid and 0.5 *N* to 1.5 *N* for solution of oxalic acid [21]. In this work, 1 *N* solution for each chemical was prepared for experimentation for comparison. Approximately

100 g of banana peels were dipped in these three solutions separately for 24 hours. According to the literature, the suggested soaking time for banana peels varies from 6 to 72 hours [16, 19]. After this experimentation, the sorbents were filtered and washed three times with distilled water and filtered by ordinary filter paper. The samples of banana peels powder were dried again in a tray drier for 24 hours at 90 °C to remove the moisture contents and finally were stored in air tight bags. These sorbents are known as activated sorbents, and can be applied to sorbent applications [22].

Method of Characterization: Characterization technique used for analyzing adsorbent properties before and after activation was Fourier Transform Infrared Spectroscopy (FT-IR). This is a proven technique for investigating various functional groups and structural variations in biomass [23]. In this research, this technique is used and given preference over other techniques because it can detect a wide variety of functional groups which are present in banana peels structure though long range of wavelengths [24]. These wavelength variations provide accurate and many information about porous structure of banana peel and helps in concluding the adsorption properties of the adsorbent. Each wavelength in a structure associated to specific functional group which can be found through catalogue of FT-IR equipment or by using the library of functional group already present in some machines. Maximum range of electromagnetic waves in FT-IR is 500 cm⁻¹ to 5000 cm⁻¹ [25]. FT-IR analysis involves study of a sorbent with respect to specific functional group frequency which helps in developing the criteria for removal of impurities when applied to any material. These functional groups are linked with group frequency which in turn linked with fundamental modes of vibration. At the end the spectral data obtained is used to determine the development of simple or complex structure produced in sorbent [26].

3. RESULTS AND DISCUSSION

FT-IR spectra show better identifications of functional group and the surface changes of the banana peels. The modified porous surface of banana peels and reformed chemical bonding within the

structure, addition and removal of any functional group were identified by FT-IR technique.

3.1 Banana Peel Structure before Treatment

The spectrum of raw banana peels shown in Fig. 1 generated by FT-IR. Starting right hand side from 500 cm^{-1} , the weak peaks are formed initially with very small gaps indicating inside structure. As wave number increases and reaches around 1000 cm^{-1} , the declining in the spectrum become high but peaks strength remains the same. If analyzed further the spectrum become narrow and near wave number 1500 cm^{-1} the peaks become sharper and the number of peaks within this range become high. This increase in number of peaks in spectrum continues up to 2200 cm^{-1} . After this the peaks strength again start getting weaker and number of peaks start decreasing and the spectrum start

declining up to 3300 cm^{-1} . As wavenumber further approaches to 3400 cm^{-1} and onwards spectrum pattern shows ascending behavior. Number of peaks becomes sharper and increased in numbers near the end of spectrum.

In Fig. 1 ascending and descending pattern of spectrum and number of peaks and their sharpness shows the adsorption properties of the sample under consideration. The portion of the spectrum where number of peaks are less sharp and decrease in number shows that the rays couldn't get enough space to penetrate inside the surface and reflect and finally the fewer peaks are formed. While sharper portion of the peaks are greater in number shows the penetration behavior of ray inside the surface. Penetration of rays inside the structure shows porous surface and hence greater the penetration of peaks more will be the porosity factor. In untreated

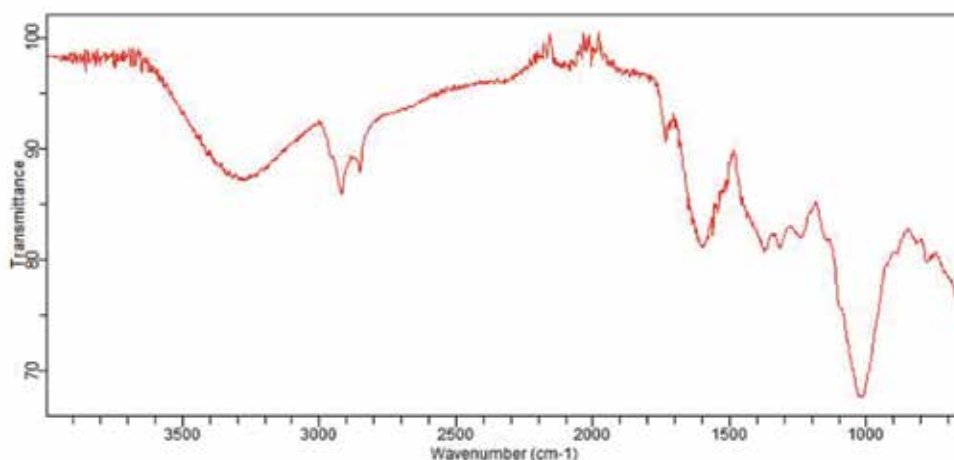


Fig. 1. Raw banana peel's spectrum.

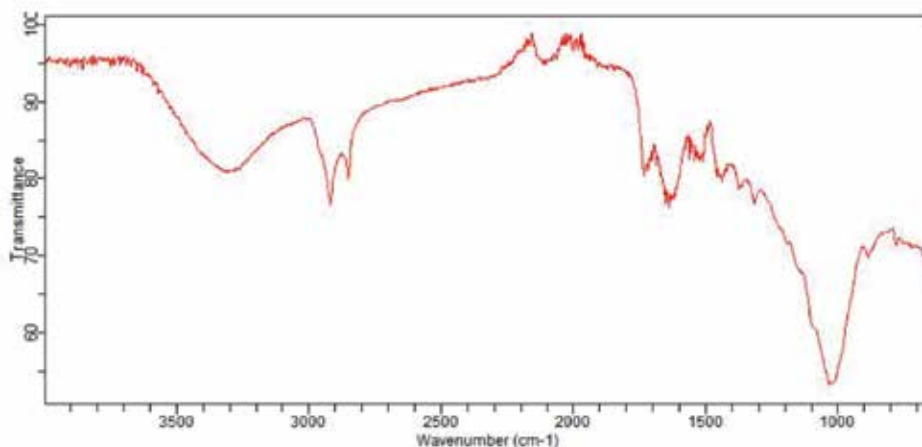


Fig. 2. Spectrum of banana peel treated with sulfuric acid.

banana peels majority of sharp peaks were found in the range of 1600 cm^{-1} to 2100 cm^{-1} . According to FT-IR wavenumber table in this range alkenyl C=C stretch, aryl substituted C=C and terminal alkyne $\text{C}\equiv\text{C}$ functional groups are present [27]. Similarly, sharp peaks in raw banana peel are also formed from 3600 cm^{-1} and onwards. This range of wavenumber contains hydroxyl groups -OH with bond stretch. Stretch in bonds shows weak attractive forces between the bonds. So overall raw banana peel shows some tendency of adsorption process because of unsaturated double and triple bonded functional groups.

3.2 Banana Peel Structure after Treatment

Fig. 2 is the spectra generated by FT-IR for banana peels powder treated with 1N solution of sulfuric acid. Comparing the results with untreated banana peels, little difference in peak pattern is observed. Spectrum declining pattern at the beginning of spectrum from right hand side varies showing less depression points while up to 1000 cm^{-1} declining pattern is same. As the spectra proceed further the pattern remains the same as in Fig.1 up to 1200 cm^{-1} . However, after 1200 cm^{-1} rays strikes at different depression points and after 1400 cm^{-1} sharpness in peaks increase along with the depression points and this pattern continues up to 1700 cm^{-1} . This ascending spectrum with increase in number of peaks in spectrum continues up to 2000 cm^{-1} . A depression point again starts between 2100 cm^{-1} to 2200 cm^{-1} and after this declining pattern of spectrum with decrease in number of peaks start up to 3300 cm^{-1} . The spectrum pattern from 2200 cm^{-1} remains the same as in Fig.1 till the end of spectrum, but sharpness of peaks is decreased in this range. Peak sharpness increases within range 1400 cm^{-1} to 1700 cm^{-1} showing more porous behavior and enhanced adsorption capacity and in this range along with multiple bonds, some aromatic groups are also present which shows more tendency of unsaturation and adsorption process [28]. After 3500 cm^{-1} peaks sharpness are reduced as compared to raw banana peels showing less porosity factor in this particular portion of the spectrum. Therefore, it can be concluded that adsorption capacity of banana peels is not improved effectively when treated with sulfuric acid.

Fig. 3 shows the spectra generated by FT-IR for banana peels treated by 1N solution of oxalic acid. This spectrum is different than previous two patterns indicating the effect of oxalic acid is better than the sulfuric acid. Up to 1000 cm^{-1} peak depressions occurs which shows some narrow gaps within the structure of treated banana peels powder indicating porous behavior. Between 1000 cm^{-1} and 1700 cm^{-1} peak pattern is entirely different than the previous one. Some depression points can be seen in the spectrum at 1150 cm^{-1} , 1350 cm^{-1} and 1450 cm^{-1} . Sharpness in peaks increases between range 1300 cm^{-1} to 1500 cm^{-1} . After 1600 cm^{-1} peak pattern up to end of spectrum remains same as in fig.1. However, from 1800 cm^{-1} to 3200 cm^{-1} peak sharpness is greater at different points as compared to raw banana peels sample, which shows the enhanced porous behavior of the sample. In oxalic acid treatment, majority of sharp peaks are produced within the range 1700 cm^{-1} to 2300 cm^{-1} . In this range, C-C double bond and triple stretch bonds are present along with some stretch aromatic group. Which shows more porous behavior and hence more tendency of adsorption process [29]. However, after 3500 cm^{-1} and onwards peaks sharpness and their number is decreased as compared to raw banana peels sample but shows better result than sulfuric acid treatment. Similarly, depression points in oxalic acid treatment are more than previous two samples. So, by oxalic acid treatment it is concluded that adsorption capacity of banana peel is enhanced.

The FT-IR spectrum of banana peel sample treated with 1N solution of sodium hydroxide solution is shown in Fig. 4. This pattern is quite different than first two but relatively close to pattern 3. At starting point some depressions in spectrum occurred and after 700 cm^{-1} long peak depression is observed. After 1000 cm^{-1} and onward ascending pattern of spectrum is observed this is same as in previous samples except for absence of depressions up to 1200 cm^{-1} . After 1300 cm^{-1} the peak sharpness start increasing with increasing number of peaks within spectrum pattern up to 1500 cm^{-1} . As the spectrum proceeds further the peak sharpness and number of peaks are increasing constantly up to 2300 cm^{-1} . Maximum numbers of sharper peak are produced within range 1800 cm^{-1} to 2100

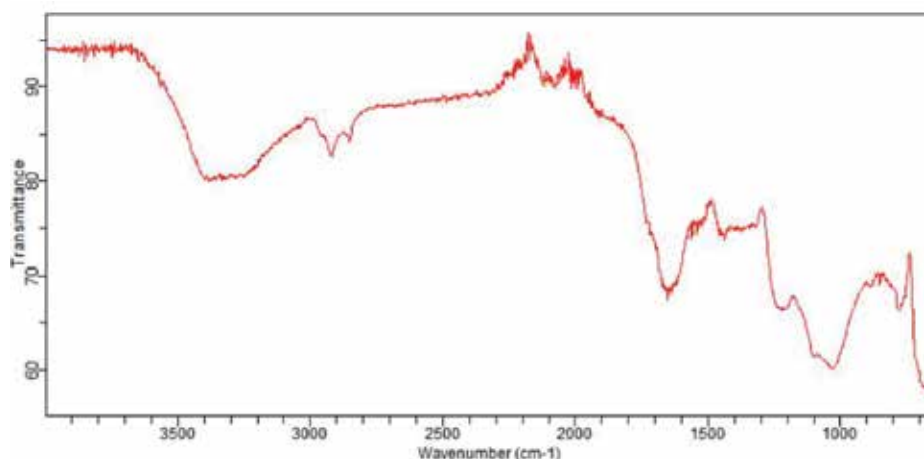


Fig. 3. Spectrum of banana after treatment with oxalic acid.

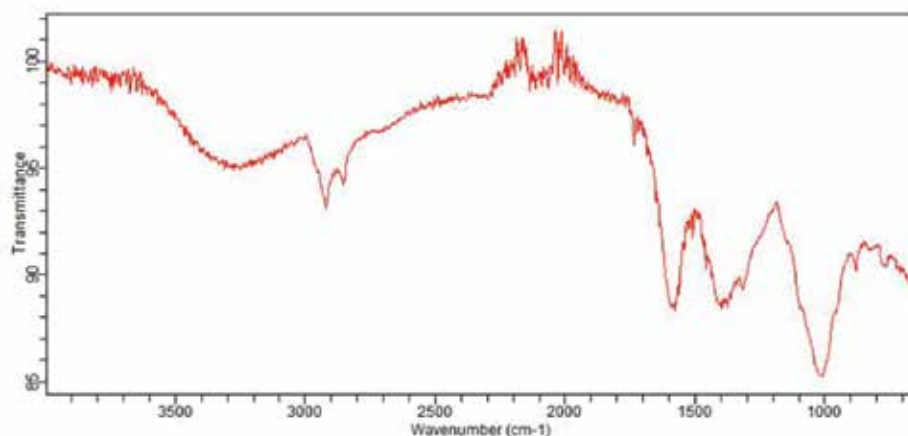


Fig. 4. Spectrum of banana peels after treatment with sodium hydroxide.

cm⁻¹. After 2300 cm⁻¹ peak sharpness and spectrum pattern shows descending pattern up to 2800 cm⁻¹ with some depressions. After 3000 cm⁻¹ spectra shows again ascending pattern. Peak sharpness and number again start increasing up to end of the spectrum. Comparing the results of sodium hydroxide treated banana peels with other samples then it can easily be observed that depression points in the spectrum and overall sharp peaks are greater in numbers throughout the spectrum. Sharpness in peaks and depression points inside the spectrum shows that infrared rays of equipment (FT-IR) strikes more in depth of the sample which shows gaps are produced inside the structure. Sodium hydroxide treatment clearly reveals that very sharp, long, and better peaks are formed in the range 1800 cm⁻¹ to 2200 cm⁻¹ and in this range greater aromatic stretch functional groups are present as compared to

double and triple bonded alkenes and alkynes. From 3500 cm⁻¹ and onwards, more sharp and better peaks are formed and in this range phenolic groups with C-H stretch bond are present along some hydroxyl or alcoholic groups [30]. Peak depressions and gaps are greater than previous samples. Hence sodium hydroxide modified and improved the adsorption characteristics of the banana peel effectively.

4. CONCLUSIONS

The banana peels were treated with different chemicals for enhancing the adsorption properties. The banana peels were treated with 1 N solution each of sulfuric acid, oxalic acid and sodium hydroxide for 24 hours. The samples were dried and then identified by FT-IR technique. It was observed that sulfuric acid partially enhanced the adsorbing

qualities of banana peels. Oxalic acid under same conditions also enhanced partially the adsorbing qualities of banana peels. The results of oxalic acid were found better than sulfuric acid. The results of banana peels treated with sodium hydroxide were found better than other two. Everything treated and untreated samples of banana peels were analyzed by FT-IR. It was observed that FT-IR is simple and rapid technique for identification of adsorbing properties of banana peels.

5. ACKNOWLEDGEMENTS

The funding support provided by University of Engineering and Technology Lahore, Pakistan, is acknowledged.

6. REFERENCES

1. Achak, M., A. Hafidi, N. Ouazzani, S. Sayadi, & L. Mandi. Low cost biosorbent "banana peel" for the removal of phenolic compounds from olive mill wastewater: Kinetic and equilibrium studies. *Journal of Hazardous Materials* 166: 117-125 (2009).
2. Annadurai, G., R.-S. Juang, & D.-J. Lee. Use of cellulose-based wastes for adsorption of dyes from aqueous solutions. *Journal of Hazardous Materials* 92: 263-274 (2002).
3. Hossain, M., H.H. Ngo, W. Guo, & T. Nguyen. Removal of copper from water by adsorption onto banana peel as bioadsorbent. *Int. J. Geomate* 2: 227-234 (2012).
4. Annadurai, G., R. Juang, & D. Lee. Adsorption of heavy metals from water using banana and orange peels. *Water Science and Technology* 47: 185-190 (2003).
5. Hossain, M., H. Ngo, W. Guo, & T. Nguyen. Biosorption of Cu (II) from water by banana peel based biosorbent: experiments and models of adsorption and desorption. *Journal of Water Sustainability* 2: 87-104 (2012).
6. Memon, J.R., S.Q. Memon, M.I. Bhangar, A. El-Turki, K.R. Hallam, & G.C. Allen. Banana peel: a green and economical sorbent for the selective removal of Cr (VI) from industrial wastewater. *Colloids and Surfaces B: Biointerfaces* 70: 232-237 (2009).
7. Memon, J.R., S.Q. Memon, M. Bhangar, G.Z. Memon, A. El-Turki, & G.C. Allen. Characterization of banana peel by scanning electron microscopy and FT-IR spectroscopy and its use for cadmium removal. *Colloids and Surfaces B: Biointerfaces* 66: 260-265, (2008).
8. Anwar, J., U. Shafique, M. Salman, A. Dar, & S. Anwar. Removal of Pb (II) and Cd (II) from water by adsorption on peels of banana. *Bioresource Technology* 101: 1752-1755 (2010).
9. Amela, K., M.A. Hassen, & D. Kerroum. Isotherm and kinetics study of biosorption of cationic dye onto banana peel. *Energy Procedia* 19: 286-295 (2012).
10. Sivaraj, R., C. Namasivayam, & K. Kadirvelu. Orange peel as an adsorbent in the removal of acid violet 17 (acid dye) from aqueous solutions. *Waste Management* 21: 105-110 (2001).
11. Khalid, A., M.A. Kazmi, M. Habib, & K. Shahzad. Kinetic & Equilibrium modelling of copper biosorption. *Journal of Faculty of Engineering & Technology* 22: xx-xx (2015).
12. Ngah W.W., & M.A.K.M. Hanafiah. Removal of heavy metal ions from wastewater by chemically modified plant wastes as adsorbents: a review. *Bioresource Technology* 99: 3935-3948 (2008).
13. Shamaila, S., N. Zafar, S. Riaz, R. Sharif, & J. Nazir. Gold nanoparticles: an efficient antibacterial agent against enteric bacterial human pathogen. *Journal of Engineering and Technology* 43: 456-463 (2012).
14. Mansha, M., A.R. Saleemi, & J.H. Naqvi. Status and spatial visualization of toxic pollutants (BTEX) in urban atmosphere. *Advances in Chemical Engineering and Science* 1: 231-237 (2011).
15. Griffiths P.R. & J.A. De Haseth. *Fourier Transform Infrared Spectrometry*. John Wiley & Sons, USA (2007).
16. Khan, A., S. H.J. Naqvi, M.A. Kazmi, & Z. Ashraf. Surface Activation of fuller's earth (Bentonite Clay) using organic acids. *Science International* 27: 2252-2258 (2015).
17. Faix, O. Fourier transform infrared spectroscopy. *Methods in Lignin Chemistry* 1992: 83-109 (2014).
18. Griffiths P.R. & J. A. de Haseth. Fourier transform infrared spectroscopy. *Science* 222: 297-302 (1983).
19. Khan, A. Bleaching of Vegetable Oil using Organic Acid Activated Fuller's Earth (Bentonite Clay). *Global Journal of Research In Engineering* 15: 234-238 (2015).
20. AjayKumar, A.V., N. A. Darwish, & N. Hilal. Study of various parameters in the biosorption of heavy metals on activated sludge. *World Applied Sciences Journal* 5: 556-563 (2009).
21. Arunachalam, R. & G. Annadurai. Nano-porous adsorbent from fruit peel waste for Decolorization studies. *Research Journal of Environmental Sciences* 5: 366-373 (2011).
22. Banerjee, S.S., M. V. Joshi, & R. V. Jayaram. Treatment of oil spill by sorption technique using fatty acid grafted sawdust. *Chemosphere* 64: 1026-1031 (2006).
23. Surewicz, W.K., H.H. Mantsch, & D. Chapman. Determination of protein secondary structure by

- Fourier transform infrared spectroscopy: a critical assessment. *Biochemistry* 32: 389-394 (1993).
24. Susi H., & D.M. Byler Resolution-enhanced fourier transform infrared spectroscopy of enzymes. *Methods in Enzymology* 130: 290-311 (1986).
 25. Goormaghtigh, E., V. Cabiaux, & J.-M. Ruyschaert. Determination of soluble and membrane protein structure by Fourier transform infrared spectroscopy. In: *Physicochemical Methods in the Study of Biomembranes*, p. 405-450 (1994).
 26. Rey, C., B. Collins, T. Goehl, I. Dickson, & M. Glimcher. The carbonate environment in bone mineral: a resolution-enhanced Fourier transform infrared spectroscopy study. *Calcified Tissue International* 45: 157-164 (1989).
 27. Siesler, H.W., Y. Ozaki, S. Kawata, & H.M. Heise, *Near-infrared Spectroscopy: Principles, Instruments, Applications*. John Wiley & Sons (2008).
 28. Nichols, P.D., J.M. Henson, J.B. Guckert, D.E. Nivens, & D.C. White. Fourier transform-infrared spectroscopic methods for microbial ecology: analysis of bacteria, bacteri-polymer mixtures and biofilms. *Journal of Microbiological Methods* 4: 79-94 (1985).
 29. Al-Qadiri, H.M., M. Lin, A.G. Cavinato, & B.A. Rasco. Fourier transform infrared spectroscopy, detection and identification of *Escherichia coli* O157: H7 and *Alicyclobacillus* strains in apple juice. *International Journal of Food Microbiology* 111: 73-80 (2006).
 30. Håkansson, K., M.J. Chalmers, J.P. Quinn, M.A. McFarland, C.L. Hendrickson, & A.G. Marshall. Combined electron capture and infrared multiphoton dissociation for multistage MS/MS in a Fourier transform ion cyclotron resonance mass spectrometer. *Analytical Chemistry* 75: 3256-3262 (2003).

Proceedings of the Pakistan Academy of Sciences

Instructions for Authors

Aims and Scope: *Proceedings of the Pakistan Academy of Sciences* is official journal of the Academy, published quarterly, in English. This open access journal publishes research papers in *Engineering Sciences & Technology, Life Sciences, Medical Sciences, and Physical Sciences*. State-of-the-art reviews (~20 pages, supported by recent references) summarizing R&D in a particular area of science, especially in the context of Pakistan, and suggesting further R&D are also considered. Manuscripts undergo double-blind review. Authors are not required to be Fellows or Members of the *Pakistan Academy of Sciences* or citizens of Pakistan.

Manuscript Format

Manuscript may contain Abstract, Keywords, INTRODUCTION, MATERIALS AND METHODS, RESULTS, DISCUSSION (or RESULTS AND DISCUSSION), CONCLUSIONS, ACKNOWLEDGEMENTS and REFERENCES and any other information that the author(s) may consider necessary. The Manuscript sections must be numbered, i.e., **1. INTRODUCTION, 2. MATERIALS AND METHODS**, and so on.

Manuscripts, in *Times New Roman*, 1.5-spaced (but single-space the Tables), with line numbering and one-inch margins on all sides on A-4 size paper, should not exceed 20 pages including Tables and Figures. Number manuscript pages throughout. The text (in **Font Size 11**, except for the sections mentioned in **Font Size 10**) must be typed in a single column across the paper width. All Tables and Figures must be placed after the text, i.e., after REFERENCES section.

(a) **Title** of the article (Capitalize initial letter of each main word; font size 16; **bold**), max 160 characters (no abbreviations or acronyms), depicting article's contents; (b) Author's first name, middle initial and last name (font size 12, **bold**), and professional affiliation (i.e., each author's Department, Institution, Mailing address and Email; but no position titles) (font size 12); (c) Indicate the corresponding author with *; (d) **Short running title**, max 50 characters (font size 10). The **next Page** should start with **Title** of the Article, followed by entire manuscript. **Headings and Subheadings** (font size 11): All flush left

LEVEL-1: ALL CAPITAL LETTERS; bold

Level-2: Capitalize each main word; bold

Level-3: Capitalize each main word; Bold, Italic

Level-4: Run-in head; Italics, in the normal paragraph position. Capitalize the initial word only and end in a colon (i.e., :)

Abstract (font size 10; max 250 words): Must be self-explanatory, stating rationale, objective(s), methodology, main results and conclusions of the study. Abbreviations, if used, must be defined on first mention in the Abstract as well as in the main text. Abstract of review articles may have variable format.

Keywords (font size 10): Three to eight keywords, depicting the article.

INTRODUCTION: Provide a clear and concise statement of the problem, citing relevant recent literature, and objectives of the investigation.

MATERIALS AND METHODS: Provide an adequate account of the procedures or experimental details, including statistical tests (if any), in a concise manner but sufficient enough to replicate the study.

RESULTS: Be clear and concise with the help of appropriate Tables, Figures and other illustrations. Data should not be repeated in Tables and Figures, but must be supported with statistics.

DISCUSSION: Provide interpretation of the RESULTS in the light of previous relevant studies, citing published references.

ACKNOWLEDGEMENTS (font size 10): In a brief statement, acknowledge financial support and other assistance.

REFERENCES (font size 10): Cite references in the text **by number only in square brackets**, e.g. "Brown et al [2] reported ..." or "... as previously described [3, 6–8]", and list them in REFERENCES section, in the order of citation in the text, Tables and Figures (not alphabetically). Only published (and accepted for publication) journal articles, books, and book chapters qualify for REFERENCES.

List of REFERENCES must be prepared as under:

a. **Journal Articles** (*Name of journals must be stated in full*)

1. Golding, I. Real time kinetics of gene activity in individual bacteria. *Cell* 123: 1025–1036 (2005).
2. Bialek, W. & S. Setayeshgar. Cooperative sensitivity and noise in biochemical signaling. *Physical Review Letters* 100: 258–263 (2008).
3. Kay, R.R. & C.R.L. Thompson. Forming patterns in development without morphogen gradients: differentiation and sorting. *Cold Spring Harbor Perspectives in Biology* 1: doi: 10.1101/cshperspect.a001503 (2009).

b. **Books**

4. Luellen, W.R. *Fine-Tuning Your Writing*. Wise Owl Publishing Company, Madison, WI, USA (2001).
5. Alon, U. & D.N. Wegner (Ed.). *An Introduction to Systems Biology: Design Principles of Biological Circuits*. Chapman & Hall/CRC, Boca Raton, FL, USA (2006).

c. **Book Chapters**

6. Sarnthein, M.S. & J.D. Stanford. Basal sauropodomorpha: historical and recent phylogenetic developments. In: *The Northern North Atlantic: A Changing Environment*. Schafer, P.R. & W. Schluter (Ed.), Springer, Berlin, Germany, p. 365–410 (2000).
7. Smolen, J.E. & L.A. Boxer. Functions of Europhiles. In: *Hematology*, 4th ed. Williams, W.J., E. Butler & M.A. Litchman (Ed.), McGraw Hill, New York, USA, p. 103–101 (1991).

Tables, with concise but self-explanatory headings must be numbered according to the order of citation (like **Table 1**, **Table 2**). Round off data to the nearest three significant digits. Provide essential explanatory footnotes, with superscript letters or symbols keyed to the data. Do not use vertical or horizontal lines, except for separating column heads from the data and at end of the Table.

Figures may be printed in two sizes: column width of 8.0 cm or page width of 16.5 cm; number them as **Fig. 1**, **Fig. 2**, ... in the order of citation in the text. Captions to Figures must be concise but self-explanatory. Laser printed line drawings are acceptable. Do not use lettering smaller than 9 points or unnecessarily large. Photographs must be of high quality. A scale bar should be provided on all photomicrographs.

Declaration: Provide a declaration that: (i) the results are original; (ii) the same material is neither published nor under consideration elsewhere; (iii) approval of all authors has been obtained; and, (iv) in case the article is accepted for publication, its copyright will be assigned to *Pakistan Academy of Sciences*. Authors must obtain permission to reproduce, where needed, copyrighted material from other sources and ensure that no copyrights are infringed upon.

Reviewers: Authors may suggest four relevant reviewers, two local and two from scientifically advanced countries.

Manuscripts must be submitted in Microsoft Word (.doc or .docx format; **pdf** files not acceptable). Figures can be submitted in Word format, TIFF, GIF, JPEG, EPS, PPT.

Manuscripts may be submitted as email attachment at the following email address. In case of any difficulty while submitting your manuscript, please get in touch with:

Editor-in-Chief
Pakistan Academy of Sciences
3-Constitution Avenue, G-5/2, Islamabad, Pakistan
Email: editor@paspk.org
Tel: +92-51-920 7140
Website: www.paspk.org



PROCEEDINGS

OF THE PAKISTAN ACADEMY OF SCIENCES:

A. Physical and Computational Sciences

CONTENTS

Volume 54, No. 3, September 2017	Page
Review Article	
Solar Tracking Techniques and Implementation in Photovoltaic Power Plants: a Review — <i>Fazli A. Khalil, Muhammad Asif, Shahzad Anwar, Sana ul Haq, and Farman Illahi</i>	231
Research Articles	
Design of Broadband Matching Network for Complex Reactive Load using L-Matching — <i>Jawad Yousaf, Zubair Mehmood, Waseem Abbas, and Khuram Shehzad</i>	243
On Classes of Analytic Functions Associated by a Parametric Linear Operator in a Complex Domain — <i>Rabha W. Ibrahim, Adem Kilicman, and Zainab E. Abdulnaby</i>	257
Automatic Signature Extraction from Document Images using Hyperspectral Unmixing — <i>Kashif Iqbal, and Khurram Khurshid</i>	269
Numerical Simulation of Fractional Order Dengue Disease with Incubation Period of Virus — <i>Zain Ul Abadin Zafar, M. Mushtaq, Kashif Rehan, and M. Rafiq</i>	277
Fractional Numerical Treatment for Biochemical Reaction Networks — <i>Zain Ul Abadin Zafar, Kashif Rehan, M. Mushtaq, and M. Rafiq</i>	297
Radiolysis-induced Dosimetric Characterization of Aqueous Solutions of a Synthetic Dye for Gamma Dosimetry — <i>Muhammad Khawar Hayat, Ramiza, Taqmeem Hussain, Nasim Akhtar, Rabia Khaliq, and Abdul Hanan Saeed</i>	305
Magnetotelluric Data Analysis using Swift Skew, Bahr Skew, Polar Diagram, and Phase Tensor: a Case Study in Yellowstone, US — <i>Erick Pranata, Selvi Misnia Irawati and Sintia Windhi Niasari</i>	311
Characterization of CO ₂ Laser Photoacoustic Spectrometer Intracavity Configuration and Its Application in Measuring Acetone Gas in Human Breath — <i>Mitrayana, Nurul Muyasaroh, Mohammad Ali Joko Wasono, and Mohammad Robikhul Ikhsan</i>	319
Efficiency Enhancement of Banana Peel for Waste Water Treatment through Chemical Adsorption — <i>Atif Khan, Hassan Jived Naqvi, Shabana Afzal, Shaista Jabeen, Misbah Iqbal, and Iram Riaz</i>	329
Instructions for Authors	337

PAKISTAN ACADEMY OF SCIENCES, ISLAMABAD, PAKISTAN

HEC Recognized, Category X; PM&DC Recognized

Website: www.paspk.org